



Recent advances in 3D bioprinted neural models: A systematic review on the applications to drug discovery[☆]

Amanda Orr ^a, Farnoosh Kalantarnia ^b, Shama Nazir ^c, Behzad Bolandi ^d, Dominic Alderson ^e, Kerrin O'Grady ^f, Mina Hoorfar ^b, Lisa M. Julian ^c, Stephanie M. Willerth ^{a,g,h,i,*}

^a Department of Mechanical Engineering, University of Victoria, Victoria, BC V8W 2Y2, Canada

^b Mechanical Engineering, University of Victoria, Victoria, BC V8W 2Y2, Canada

^c Department of Biological Sciences, Simon Fraser University, Burnaby, BC V5A 1S6, Canada

^d Department of Chemistry and Biochemistry, University of Windsor, Windsor, ON, Canada

^e Newcastle University Biosciences Institute, Newcastle-Upon-Tyne, NE2 4HH, UK

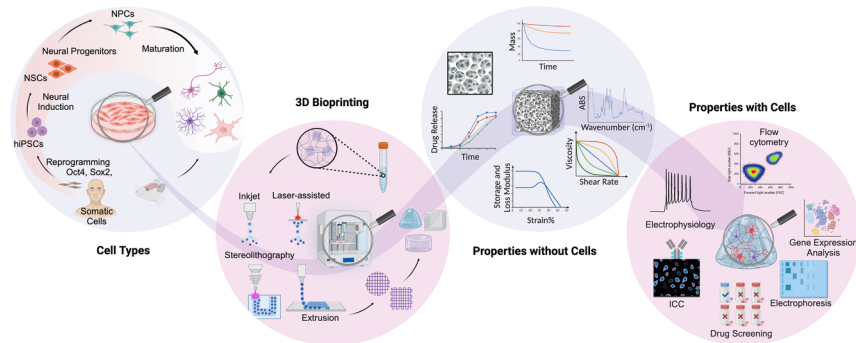
^f Department of Biomedical & Chemical Engineering, Syracuse University, Syracuse, NY 13244, USA

^g Division of Medical Sciences, University of Victoria, Victoria, BC V8W 2Y2, Canada

^h Centre for Advanced Materials and Technology, University of Victoria, Victoria, BC V8W 2Y2, Canada

ⁱ School of Biomedical Engineering, University of British Columbia, Victoria, BC V6T 1Z4, Canada

GRAPHICAL ABSTRACT



ARTICLE INFO

Keywords:

Neural tissue engineering
3D bioprinting
Standardized 3D model characterization
Cellular characterization
Functional brain tissues
Mechanical characterization
Drug discovery
Human induced pluripotent stem cells

ABSTRACT

The design of neural tissue models with architectural and biochemical relevance to native tissues opens the way for the fundamental study and development of therapies for many disorders with limited treatment options. Here, we systematically review the most recent literature on 3D bioprinted neural models, including their potential for use in drug screening. Neural tissues that model the central nervous system (CNS) from the relevant literature are reviewed with comprehensive summaries of each study, and discussion of the model types, bioinks and additives, cell types used, bioprinted construct shapes and culture time, and the characterization methods used. In this review, we accentuate the lack of standardization among characterization methods to analyze the functionality (including chemical, metabolic and other pathways) and mechanical relevance of the 3D bioprinted

[☆] This article is part of a special issue entitled: 'PharmBio3DP' published in Advanced Drug Delivery Reviews.

* Corresponding author.

E-mail address: willerth@uvic.ca (S.M. Willerth).

Neurodegenerative disease
 Neural progenitor cells
 Neural stem cells
 Construct culture
 Bioinks
 Construct geometry

constructs, and discuss this as a critical area for future exploration. These gaps must be addressed for this technology to be applied for effective drug screening applications, despite its enormous potential for rapid and efficient drug screening. The future of biomimetic, 3D printed neural tissues is promising and evaluation of the *in vivo* relevance on multiple levels should be sought to adequately compare model performance and develop viable treatment options for neurodegenerative diseases, or other conditions that affect the CNS.

Nomenclature	
Acronyms	
2D	two dimensional
3D	three dimensional
6-ODHA	6-hydroxydopamine
AA	amino acid
AAS	antibiotic antimitotic solution
AB	Alamar blue
AD	Alzheimer's disease
ADSCs	adipose-derived stem cells
AI	artificial intelligence
AuNPs	gold nanoparticles
BBB	blood brain barrier
BDNF	brain derived neurotrophic factor
BFCNs	basal forebrain cholinergic neurons
bFGF	basic fibroblast growth factor
BIONs	bioengineered immunomodulatory organelle targeted nanozymes
BMECs	brain microvascular endothelial cells
C-AMP	cyclic adenosine monophosphate
CaCl ₂	calcium chloride
CAM	Calcein AM
CaSO ₄	calcium sulphate
CCH	conductive composite hydrogel
CHIR	CHIR99021
CMC	carboxymethylcellulose
CNS	central nervous system
CSMA	chondroitin sulfate methacrylate
CSMS	chondroitin sulfate methacrylate
DA	dopaminergic
DC	dopamine conjugated
DC-Gel	dopamine-conjugated gelatin
DC-Gel-MA	dopamine-conjugated gelatin methacrylate
DC-HA	dopamine-conjugated HA
DIW	direct ink writing
DLP	digital light processing
DMSO	dimethylsulfoxide
E	elastic modulus
eAPs	evoked action potentials
EB	embryoid body
ECM	extracellular matrix
EDOT	3,4-ethylenedioxythiophene
EGF	epidermal growth factor
EGM-2	Endothelial cell growth medium
EHD	electrohydrodynamic
ELISA	enzyme-linked immunosorbent assay
FBS	fetal bovine serum
FGF-2	fibroblast growth factor 2
FPA	primary fetal astrocytes
FRESH	freeform reversible embedding of suspended hydrogels
FTIR	Fourier transform infrared spectroscopy
G'	storage modulus
G''	loss modulus
GBM	glioblastoma
GDNF	glial-derived neurotrophic factor
GelMA	gelatin methacrylate
GEMMs	genetically engineered mouse models
GG	gellan gum
GMHA	glycidyl methacrylate hyaluronic acid
HA	hyaluronic acid
HA-BCN	bicyclo[6.1.0]nonyne modified HA
hiPSCs	human induced pluripotent stem cells
hMG	human microglia cells
hNSCs	human neural stem cells
HTS	high-throughput screening
HUVECs	human umbilical vein endothelial cells
ICC	immunocytochemistry
ID	inner diameter
IHC	immunohistochemistry
IKVAV	Ile-Lys-Val-Ala-Val
IPSCs	inhibitory postsynaptic currents
IVFK	Ac-Ile-Val-Phe-Lys-NH ₂
IVZK	Ac-Ile-Val-Cha-Lys-NH ₂
KCl	potassium chloride
LAB	laser-assisted bioprinting
LAP	lithium phenyl (2,4,6-trimethylbenzoyl) phosphinate
LDN	LDN193189
LIFT	laser-induced forward transfer
MDCKs	Madin-Darby Canine Kidney epithelial cells
MEAs	microelectrode arrays
MGE	medial ganglionic eminence
MMP	matrix metalloproteinase
MNPs	motor neuron progenitors
MNs	motor neurons
mRNA	messenger RNA
MSCs	mesenchymal stem cells
MSs	microspheres
mTG	micro-transglutaminase
MTT	3-[4,5-dimethylthiazol-2-yl]-2,5 diphenyl tetrazolium bromide
NAs	neural aggregates
NGF	nerve growth factor
NPCs	neural progenitor cells
NPs	nanoparticles
NSCs	neural stem cells
NSPCs	neural stem/progenitor cells
OoC	organ on a chip
OPCs	oligodendrocyte precursors
P/S	penicillin/streptomycin
PD	Parkinson's disease
PDMS	polydimethylsiloxane
PDXs	patient-derived xenografts
PecMA	pectin methacrylol
PEDOT	3,4-ethylenedioxythiophene polymer
PEG	polyethylene glycol
PEGDA	PEG-diacylate
PF127-SH	thiolated Pluronic F-127
PI	photoinitiator
PLO	poly-L-ornithine
PNS	peripheral nervous system
PRISMA	Preferred Reporting Items for Systematic Reviews and Meta-Analyses
Puro	purmorphamine

qPCR	quantitative polymerase chain reaction
RA	retinoic acid
RGD	Arg-Gly-Asp
RGD-GG	RGD-modified gellan gum
rhPDGF-AA	recombinant human platelet-derived growth factor-AA
rhShh	recombinant human sonic hedgehog
RNA	ribonucleic acid
RT-qPCR	reverse transcriptase quantitative polymerase chain reaction OR real-time quantitative PCR used throughout
sALS	sporadic Amyotrophic lateral sclerosis
sAPs	spontaneous action potentials
SB	SB431542
SCI	spinal cord injury
SEM	scanning electron microscopy
SHAPE	Self-Healing Annealable Particle-ECM
SilMA	methacrylated silk fibroin
SISMA	methacryloyl-modified decellularized small intestinal submucosa
SISMA-GO	SISMA with electroconductive graphene oxide nanoflakes
SLA	stereolithography
SRB	sulforhodamine B
t-ZnO	tetrapodal-shaped zinc oxide
TA	tannic acid
TMZ	Temozolomide
TPP	two-photon polymerization
UV	ultraviolet
VEGFA	vascular endothelial growth factor A
VGFs	vascular growth factors
VM	ventral midbrain
WJ-MSCs	Wharton jelly mesenchymal stem cells
Markers:	
βIII tubulin/TUJ1	Beta III tubulin
AADC	aromatic L-amino acid decarboxylase
APOL4	apolipoprotein L4
APOL6	apolipoprotein L6
ATP	adenosine triphosphate
β-Actin	beta actin
BDNF	brain-derived neurotrophic factor
BRN2	also known as POU3F2 (NPC marker)
CA IX	carbonic anhydrase 9
CB	calbindin
CD133	prominin 1 (GBM stem cell marker)
CD31	also known as platelet and endothelial cell adhesion molecule 1 (PECAM1)
CD44	transmembrane glycoprotein
ChAT	choline acetyltransferase
CNPase	cyclic nucleotide 3'-phosphodiesterase
CR	calretinin
CTIP2	COUP-TF-interacting protein 2
DAPI	4',6-diamidino-2-phenylindole
DAPT	γ-secretase inhibitor IX
DAT	dopamine transporter
DCX	doublecortin
ESG1	TLE family member 1
F-actin	filamentous actin
FBP	fructose 1,6-bisphosphate
FOXA2	Forkhead Box A2
FOGX1	Forkhead Box G1
GABA	γ-aminobutyric acid
GAD	glutamic acid decarboxylase
GFAP	glial fibrillary acidic protein
GFP	green fluorescent protein
GLT-1	glutamate transporter 1
H19	endodermal marker
HAND1	heart and neural crest derivatives expressed 1 (mesoderm marker)
HB9	protein homeobox 9
HIF1-α	hypoxia inducible factor 1 subunit alpha
HMG	high mobility group
HMGB1	high mobility group box 1
I-BET 151	BET bromodomain inhibitor
IGF-1	insulin-like growth factor 1
IGF2	insulin like growth factor 2 (mesoderm marker)
iGluSnFR	glutamate-sensing fluorescent reporter
IKK	inhibitory kappa B kinase
IL-1β	interleukin-1 beta
Isl1	ISL LIM homeobox 1
ISX9	isoxazole 9
ITGB1	integrin subunit beta 1
Ki-67	proliferation marker
LMX1B	LIM homeobox transcription factor 1 beta
MAP2	microtubule-associated protein 2
MKI67	marker of Ki-67
NANOG	nanog homeobox
NCAD	N-cadherin
NCAM	neural cell adhesion molecule
Nestin	neuroepithelial stem cell protein
NeuN	neuronal nuclear protein
NG2	nerve/glial-antigen 2
NGF	Nerve growth factor
NKX2-1	NK2 homeobox 1
Nr4A1	nuclear receptor subfamily 4, group A, member 1
Nr4a2	nuclear receptor subfamily 4, group A, member 2 ("Nurr1")
Nrf2	nuclear factor erythroid 2-related factor 2
NT3	neurotrophin-3
NURR1	Nr4a2
O4	oligodendrocyte marker
OCT4	octamer-binding transcription factor 4
OLIGO2	oligodendrocyte transcription factor 2
PAX	paxillin focal adhesion protein
PAX6	Paired box protein 6
PDX1	pancreatic and duodenal homeobox 1 (endodermal marker)
PSD95	discs large MAGUK scaffold protein 4 (also DLG4)
PTK2	protein tyrosine kinase 2
PV	parvalbumin
REX1	zinc finger protein 42 (Zfp42)
S100β	S100 calcium-binding protein B
SATB2	special AT-rich sequence binding protein 2
SLC2A1	solute carrier family 2 member 1
SMI312	neurofilament marker
SOX1	SRY (sex determining region Y)-box 1
SOX2	SRY-box transcription factor 2
SOX9	SRY-box transcription factor 9
SOX10	SRY-box transcription factor 10
SPP1	secreted phosphoprotein 1
SSEA4	stage-specific embryonic antigen-4
SST	somatostatin
SYN	synaptophysin
SYN1	synapsin-I
SYP	presynaptic terminals marker
TBR1	T-box brain transcription factor 1
TBR2	T-box brain protein 2
TDGF1	teratocarcinoma-derived growth factor 1
TH	tyrosine hydroxylase
TNF-α	tumour necrosis factor-alpha
TRA-1-60	pluripotent marker
TUBB3	class III beta-tubulin protein
TUJ1	β-III tubulin (may be referred to as β-III tubulin, III beta-

tubulin, or β T III in the original paper)	vGAT vesicular GABA transporter
UTF1 undifferentiated embryonic cell transcription factor 1	vGlut1 vesicular glutamate transporter 1
VEGFA vascular endothelial growth factor A	Vimentin structural intermediate filament protein
VEGFR2 vascular endothelial growth factor receptor 2	

1. Introduction

Neural tissues are not limited to the brain as neural cells can be found throughout the central nervous system (CNS) and the peripheral nervous system (PNS) [1]. The brain and spinal cord comprise the CNS and are both vital to human function, sensory capacities, and the emergence of various neurodegenerative disorders. The brain is a complex and intricate organ that hosts an abundance of cellular components, defences, and synaptic pathways and is directly responsible for movement, memory, and all processes that occur within the human body. Brain tissue is predominantly populated with a diverse arrangement of cells, including neurons, astrocytes, oligodendrocytes, microglia and other support cells [2]. Spatially, neurons primarily comprise the periphery (or grey matter) of the brain and are surrounded by interior white matter filled with support cells – astrocytes, microglia and oligodendrocytes [3]. The cells of the brain form complex interactions through cell signalling and coordination, where neurons are the signalling cells, and the glial cells coexist as structural support cells, generating intricate neural networks responsible for multifaceted functions. These organizations are heterogeneous throughout the brain microstructure and exhibit regional distinctions that vary in stiffness, cellular composition and function [4], so recapitulating the structure through *in vitro* models remains challenging. The formation of the brain itself has complexities that may not be mimicked such as spatial coordination for synaptic connections [4], and the plasticity of the brain generates complex restructuring depending on the timescale, adding to this challenge.

The blood brain barrier (BBB), a crucial component of the brain, serves as the protective physiochemical barrier in the CNS that selectively regulates nutrient and hormonal transport using various routes that rely on biochemical recognition and passive transport [5]. The cellular composition of the BBB is comprised primarily of brain microvascular endothelial cells, supported by the basement membrane (collagen, elastin, fibronectin, laminin, proteoglycans), astrocytes, pericytes, and microglial cells [5]. Neurons interact with these regulating bodies to generate a convoluted symbiotic functioning network [5]. Importantly, the BBB plays a crucial role in drug efficacy, as its maintenance controls the primary defence system to restrict passage into the brain, thereby limiting drug adsorption.

Three dimensional (3D) bioengineered models can serve as fundamental tools in advancing the understanding of functional biology and neurodegenerative disorders, among others. Prominently, their use can be used for screening various drug therapies for disease treatments and extend to evaluating drug toxicity and other effects during brain development and address the high costs associated with ineffective pre-clinical disease models [6]. The design of more complex models that resemble native tissue are more beneficial compared to two-dimensional (2D) models and those that use monocultures. Importantly, disease pathology has been more pronounced when multi-cell models are employed, inherently due to synergistic cellular signalling. The recapitulation of native cells is promoted through the incorporation of hydrogel-based environments that resemble the extracellular matrix (ECM). Further, the design of representative 3D neural tissues can be enhanced using human induced pluripotent stem cells (hiPSCs). These cells can be sourced from individuals to create patient-specific models that can be precisely patterned to form networks via intrinsic cell signaling pathways and organization similar to native brain tissue by incorporating 3D bioprinting into neural tissue model workflows.

1.1. 3D bioprinting

Our understanding of the human brain is limited due to the general inaccessibility of human brain tissue and the lack of experimental models that accurately replicate key aspects of its developmental and functional complexity. Much of our knowledge of how the brain develops and functions has been gained from rodent models, whose brains lack the intricate cytoarchitecture and many characteristic features of the human brain. Various structural and biological limitations constrain the use of 2D cell cultures as the foundation for most brain models. Monolayer cultures lack the essential morphological and spatial organization of tissues, fail to replicate the complex 3D structure of the brain and do not capture crucial interactions between cells or between cells and the ECM [7]. The dynamics of waste accumulation and removal are also omitted [8]. Therefore, developing more complex 3D models is crucial for a better understanding of the CNS.

3D bioprinting of human derived neural cells enables the creation of complex tissue structures that closely mimic the architecture and function of human brain tissues [9]. Additionally, 3D bioprinting can enable us to reproduce abnormal structures associated with human brain diseases (Lewy bodies, amyloid plaques), which are often not replicable in animal models [10,11]. Due to a historical lack of ideal brain models, scientists have faced major setbacks in drug discovery for neurological disorders. Drugs tested and deemed successful in animal models often fail in clinical settings. While replicating the full architecture and function of the human brain is not yet possible, the field of tissue engineering has made significant progress toward this goal [9]. 3D bioprinting deposits bioinks in a layer-by-layer fashion to achieve precise patterning and relevant geometries as well as integrates cues for differentiation, growth and interaction. These architectures better resemble the complex structures within neural tissues for more precise cell deposition and inherently more representative tissue models compared to 2D models [1], especially for disease models [12,13].

3D models better emulate the complex organization and signalling between cells, which play a major role in recapitulating disease pathophysiology [14]. Non-bioprinted 3D models, such as organoids can have limited disease expression, demonstrate experimental variability, and/or are difficult to structurally reproduce [15]. 3D bioprinting can address these obstacles since it can generate highly complex and precise tissue patterning that incorporates relevant mechanical stiffness of native tissues, which are crucial for mimicking disease pathology in the lab [16,17]. Here, we briefly discuss the various 3D bioprinting approaches.

1.1.1. Extrusion-based bioprinting

Extrusion-based bioprinting is a widely used technique that deposits viscous bioinks, including hydrogels and cell suspensions, layer-by-layer to create 3D structures [18]. This method is versatile and cost-effective but can exert significant pressure on cells, leading to lower survival rates and reduced tissue functionality [19,20]. Despite these challenges, extrusion-based bioprinting is favoured in tissue engineering and cancer research due to its ability to create complex models that mimic *in vivo* tissue architecture [21,22]. Ongoing advancements focus on optimizing printing parameters, such as nozzle geometry and extrusion pressure, to enhance cell viability and achieve high-resolution prints [22,23]. This method has proven effective in creating compartmentalized tumoroids and other models that closely replicate the *in vivo* environment, making it a key tool in studying cancer and other diseases [21,24].

1.1.2. Droplet-based bioprinting

As the name implies, droplet-based bioprinting deposits droplets that are generated from various mechanisms (sound, thermal, electric), and includes the methods of inkjet and acoustic bioprinting. Inkjet bioprinting uses low-viscosity solutions to deposit microdroplets onto a substrate in a precise, layer-by-layer manner [25]. Thermal or piezoelectric actuators control this process, with thermal inkjet printing relying on localized heating to generate droplets and piezoelectric printers using acoustic waves [19,26]. The technique offers high printing speed and micron precision, making it ideal for creating detailed 3D structures at a relatively low cost [19]. Inkjet bioprinting is versatile, enabling the printing of human cancer cellular spheroids and complex biomaterial combinations [27–29]. However, challenges such as nozzle clogging and limitations in the range of printable bioinks due to viscosity constraints remain [30,31]. Ongoing improvements aim to enhance resolution and expand material versatility while addressing the impact of crosslinking agents on cell viability [32–34].

Acoustic-based bioprinting alleviates the nozzle-clogging issue of other droplet-based printing methods since it uses sound waves to position bioinks in layered formulations [35]. In addition, this method allows for the printing of sensitive biomaterials with high precision, but the technique has limited printed speeds and requires specialized equipment which may be inaccessible for users [35].

1.1.3. Light-based methods

Laser-assisted bioprinting (LAB) leverages laser-induced forward transfer (LIFT) technology to produce intricate tissue constructs with high precision. Originally developed for metal patterning in computer chip fabrication, LIFT was adapted for bioprinting, enabling the precise deposition of cells and bioinks at the micron level [36–39]. LAB excels in creating high-resolution, complex 3D cellular models, with high cell viability and density [40,41]. The absence of nozzles eliminates clogging issues, and LAB supports a wide range of bioink viscosities, making it suitable for advanced tissue engineering applications [42,43]. Despite these strengths, LAB faces challenges, such as limited productivity and high equipment costs [44]. However, its precision and ability to produce complex cellular models with high fidelity make it a promising tool for tissue engineering and regenerative medicine [41,45–47].

Another LAB technique is two-photon polymerization (TPP). TPP uses femtosecond lasers to induce polymerization and has the potential to generate sub-micron-level printing resolution [35]. This technique incorporates the principles of two-photon absorption, which in the presence of a photoinitiator, leads to polymerization of the material(s) [35]. Since this technique requires the use of specialized lasers, TPP can be costly and the use of photoinitiators may lead to cytotoxicity, but the ability to achieve nanometer-level resolution has favourable relevance to neurite outgrowth *in vitro* [48].

1.1.4. Stereolithography

Stereolithography (SLA) uses photosensitive polymers, solidified layer-by-layer with light, to fabricate complex structures with high resolution [49,50]. Originally adapted from a 2D method, SLA allows for efficient construction of intricate scaffolds in biomedical applications, maintaining high cell viability and consistency in print times regardless of layer complexity [51–54]. Recent advancements address the toxicity of photo-curing agents and potential DNA damage from UV light by using visible light for biocompatibility and material versatility [50,54]. Despite these improvements, challenges remain, including the development of fully biocompatible polymers and the need for a photopolymer-filled reservoir, leading to material waste and increased costs [55,56]. Nevertheless, SLA continues to be a prominent technique for creating detailed 3D structures in tissue engineering.

1.1.5. Indirect printing

Indirect bioprinting uses a sacrificial framework to support the formation of polymer-based scaffolds, with the support material removed

post-printing to create the final structure [57]. This technique is versatile, allowing for the incorporation of various materials, including bioactive substances, into scaffolds with controlled external and internal architectures [58]. For example, carbohydrate glass networks can serve as sacrificial templates, enabling precise control over endothelialization and network geometry in engineered tissues [59]. Indirect bioprinting shows promise in creating complex hydrogel scaffolds, although its application in nerve tissue regeneration is still underexplored, with the mechanical and biological properties of such scaffolds needing further research. The method's capability to incorporate different materials and create advanced architectural designs makes it a valuable tool for complex tissue engineering applications [31,60,61].

1.1.6. FRESH printing

Freeform Reversible Embedding of Suspended Hydrogels (FRESH) bioprinting is a cutting-edge technique designed to print soft, fragile hydrogels with high fidelity by extruding low-viscosity inks into a thermoreversible gelatin microparticle support bath, stabilizing the printed material and allowing complex freeform structures that would otherwise collapse under gravity [62,63]. This method supports multiple crosslinking strategies, enabling the construction of large, intricate tissue scaffolds, such as vascularized heart and neural models, with applications in surgical training and tissue engineering [64,65]. Recent advancements have improved printing resolution and mechanical properties by refining the support bath's properties, enhancing its capability to print various hydrogels with precise resolution [65–67]. This technique's versatility extends to creating complex biological structures, demonstrating its potential in biomedical applications [68].

1.1.7. Emerging printing technologies

Beyond the aforementioned printing methods, relatively new technologies are emerging that have applications in tissue engineering such as magnetically induced and chaotic bioprinting. Typical printing strategies for magnetic bioprinting involve seeding cells that have been magnetized with magnetic nanoparticles (NPs), allowing for precise patterning of cells using an external magnet [69]. This technique has been commonly used to form spheroids through suspension or levitation within a culture dish or in ring form based on differing magnetic fields to dictate the structure [69]. However, compared to other printing techniques, this method does not specifically deposit cells through a printhead within bioink, and relies on the magnetic organization from stimulus outside of the dish, and concentrations of magnetic NPs or media conditions are not always clear [69]. The technique also has limitations in ensuring multiple cell phenotype of spheroid co-cultures for aortic valves [70] and adipose tissue [71] models. There are also uncertainties of the influence of the magnetic NPs on cell function [72]. However, research has shown that the magnetic properties of NPs within cells can be regenerated in mesenchymal stem cells in conditions associated with high iron and ferritin [73].

Chaotic bioprinting is a method of printing that incorporates chaotic mixing through laminar flow within the printhead that happens in a predictable and reproducible fashion [74]. The mechanism combines droplets into viscous fluids in a defined flow cycle, which generates exponentially complex mixing interfaces which can be solidified and create favourable environments for cells [75]. While this technique has yet to be incorporated with neural models, it has the potential to mimic the BBB given the hierarchical patterning of chaotic bioprinting [75].

1.2. Other models

As mentioned, 3D models better emulate the complex organization and signalling between cells, but certain models, such as organoids, can have limited disease expression and reproducibility [15]. These models were not explored in our review, but given their prevalence in the literature, are worth mentioning.

Spheroids – clusters of proliferating neural cells – do not possess the

complex structures or functions of mature brain tissue [7]. To overcome the limitations of spheroids, organoids have been developed, which are 3D models capable of self-organization and mimicking certain aspects of brain architecture, such as the formation of structures resembling cortical layers [76,77]. Organoids offer a more representative *in-vivo* physiology than 2D cultures despite the variability that results from their formation and development differences [78]. 3D matrix models have emerged as a promising alternative to address the inherent variability often encountered with spheroids and organoids. Self-organizing organoids can vary significantly in size, shape, and cellular composition, whereas 3D matrix models offer a higher degree of standardization. These models require culturing or embedding specific cells in hydrogels that solidify into a controlled-thickness matrix. The hydrogels create a supportive scaffold for cell growth and organization while maintaining predictable and reproducible conditions.

Additionally, organ-on-a-chip (OoC) is a powerful tool for studying the brain. OoC systems are engineered devices with channels, chambers, and membranes to provide a small-scale platform and replicate the natural environment of tissues by mimicking the physiological structure and biochemical cues [76,79]. These devices offer precise control over the microenvironment, allowing for the study of cell behaviour, drug responses, and disease progression in a controlled setting [80,81]. Polydimethylsiloxane (PDMS) is commonly used in OoC fabrication due to its optical clarity, stretchability, ease of fabrication, and high oxygen permeability, making it ideal for creating detailed microstructures [79]. In the field of brain tissue engineering, OoC systems can mimic the complex vascularization and nutrient gradients found in the brain, making them valuable for studying neurological disorders [82–84]. Integrating OoC and 3D bioprinting approaches shows promise for creating more sophisticated brain models. For example, a 3D bioprinted GBM model was developed on a chip to simulate the oxygen-deprived environment of a tumour by creating an oxygen gradient [85]. However, due to its specialized and complex nature, a detailed discussion on OoC is beyond the scope of this review. For comprehensive insights, readers are referred to several reviews on the topic, including those by Amirifar *et al.* and Akcay *et al.* [86,87].

Animal models are also widely used for understanding function, pathology, and testing drug therapies in clinical settings. Rodents that

include genetically engineered mouse models (GEMMs)[88] or patient-derived xenografts (PDXs)[89] have been instrumental in advancing our understanding of disease mechanisms and pathologies. Despite their utility, differences in anatomical structures and developmental trajectories between species pose challenges to directly translating findings. For instance, mouse brains differ from human brains in size, complexity, and regional organization, limiting their ability to replicate the spatial heterogeneity and microenvironment of human brain [90].

Animal models of glioblastoma (GBM) facilitate studying mechanisms such as tumor invasiveness, angiogenesis, and resistance to therapies, but genetic and immunological differences further complicate their translational potential to preclinical studies [91]. Mice often exhibit a heightened immune response to GBM, which contrasts with the immunosuppressive nature of the human GBM microenvironment. This heightened immunogenicity can skew the evaluation of immunotherapies [92]. Furthermore, the genetic background of mouse GBM models does not fully recapitulate the heterogeneity and mutational landscape of human GBM, potentially overlooking critical aspects of tumor biology [91]. Moreover, age-related neurodegenerative diseases are largely human-specific and cannot be replicated in rodents. Some aged mammals, including nonhuman primates, bears, and dogs, spontaneously develop neuropathological features like β -amyloidosis and neurofibrillary tangles, though these do not fully match human disease phenotypes [93]. For instance, despite similarities in the amino acid sequences of pathogenic proteins between humans and nonhuman primates, the latter appear more resilient. Differences in protein clearance mechanisms, chaperone activity, proteasomal and autophagosomal pathways and lifespan likely contribute to this resistance [93]. Drug screening using animal models is time-consuming, while cellular models offer a faster alternative, being highly valuable for high-throughput screening and assays, where animal models are limited. The goal of 3D cellular models is to be able to offer better pre-clinical screening for drug therapies, alleviating the costly expense (time and money) of poor translational aspects of animal models.

1.3. Systematic review

There has been extensive review of 3D bioprinting for neural tissue

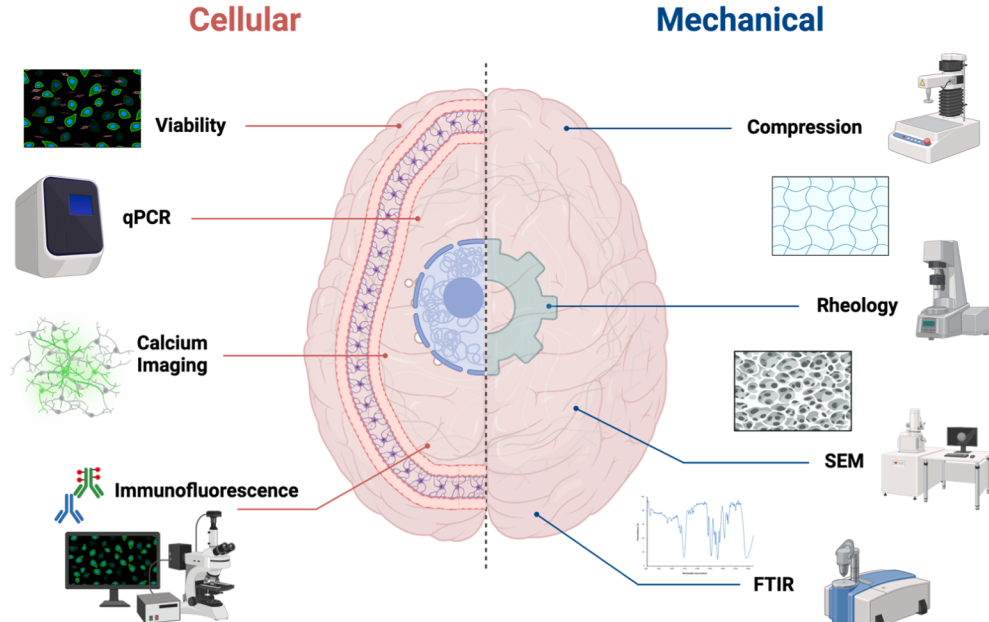


Fig. 1. Overview of common cellular and mechanical characterization techniques involved in 3D bioprinted neural tissue models. Cellular characterizations include cell viability, quantitative polymerase chain reaction (qPCR), calcium imaging, and immunofluorescent analysis. Mechanical characterizations include compression tests, rheology, scanning electron microscopy (SEM), and Fourier transform infrared spectroscopy (FTIR). Created with BioRender.com.

engineering and its optimizations, applications, among others. Therefore, this systematic review aims to comprehensively explore the work that has been done in the last decade on 3D bioprinting of neural tissues – with an emphasis on neural brain tissue – to rationally compare the methods, materials, and characterization of the bioprinted models. Specifically, the objective of the systematic review was to understand what research has been done on 3D bioprinting neural tissues and evaluate the types of methods used to assess the efficacy of these models. Here we review what the field of 3D bioprinting has accomplished in the last 10 years toward the establishment of human-relevant models of brain disorders, assessment of drug efficacy, and nerve tissue regeneration.

While innovation and variation in materials are practical and encouraged to explore the most accurate models of the brain, we found a wide variation in the characterization methods used. The characterization of the 3D bioprinted constructs should include methods that aptly investigate their relevance to human neural tissues (Fig. 1). These techniques include an assessment of structure, fundamental function, and behaviour, and in the case of disease models, recapitulate the disease pathophysiology.

2. Methods

2.1. Systematic review

The systematic literature search followed the updated Preferred Reporting Items for Systematic Reviews and Meta-Analyses (PRISMA) 2020 guidelines [94]. Three databases were examined, PubMed, Scopus, and Web of Science. Three or four main keywords were searched to capture original research articles that covered the broad topics of ‘3D bioprinting’, ‘neuronal cells/brain models’ or ‘co-cultures’ and ‘diseases’ (Table 1). The term “disease” was included to attempt to incorporate applications for drug discovery and drug screening as the focused application of this review. The search was conducted over the last ten years (from 01/01/2014 to 12/08/2024) in all cases. In PubMed, articles were filtered to not include review articles or systematic review articles; for Web of Science, review articles were excluded; for Scopus, articles exclusive to research articles or “ar” document types were included (full details in [Supplemental Information, Tables S1, S2](#)). The last search was conducted on August 12th, 2024. The 3-keyword and 4-keyword searches and screening were conducted by two individual

reviewers, respectively, and the results were compiled.

Papers were exported from the respective databases as summaries (including abstracts). The documents were initially screened by reading the title; relevant articles were also evaluated within their abstracts to ensure applicability. The articles that were not immediately excluded based on title were assessed based on their abstract, and if it was still unclear if relevant, an assessment of methodology was sought. The reasons for exclusion were recorded in Excel as being removed from the title, abstracts or methods, and the reasons for removal were recorded and summarized in Excel.

Reasons for removal were done for various reasons including non-research articles – such as reviews, commentaries or chapters ($n = 78$, ‘3-keyword’ search), or simply no bioprinting (Fig. 2). Papers were excluded based on the most obvious exclusion criteria but could have been excluded under multiple criteria. Classification as “not bioprinting” was the broadest exclusion criteria, which varied from no bioprinting being mentioned with no relevance to neural tissue engineering (e.g., the detection of VOCs from 3D printing), or the lack of 3D bioprinting in cell culture (e.g., co-cultures but no printing). Nerve guide conduits were excluded; cells that were seeded on either 3D bioprinted, 3D printed, or non-printed matrices were also excluded since it has been thoroughly demonstrated that 3D bioprinting can achieve reproducible constructs with highly accurate patterning.

Of the included articles, evaluation of and documenting the model type (neural, brain, spinal cord, tumour, etc.), number of printed cell types (1, 2, >2), biomaterials used, days of construct culture assessment, and key functional features (e.g., viability, protein expression markers identified), were recorded. The accumulated data was evaluated to infer trends in 3D bioprinting of neural tissues.

3. Results and discussion

Based on our search, in the last ten years, there have been 44 research papers that involve 3D bioprinted neural tissue models with disease applications. Two papers were not identified during the systematic search but were manually added due to their relevance, for a total of 46 included papers. Neural tissues were 3D bioprinted using a variety of polymers (Fig. 3A); alginate was the most prevalent polymer for bioinks (used 18.18% overall), followed by fibrinogen (11.82%) and gelatin (10.0%), and gelatin-methacrylate (GelMA; 8.18%). A detailed description of polymers and their respective influence on material

Table 1

General keywords for 3 database searches of 3-keyword and 4-keyword (including co-culture specific) searches. The search was conducted on 12/08/2024.

3 Keywords						
Platform	Bioprinting	iPSCs/neurons	Disease	Co-culture/Glia	Results	
PubMed	Bioprinting/	Brain/ Neurons/ Motor Neurons/ Serotonergic Neurons/ GABAergic Neurons/	Disease		202	
Web of Science	Three-Dimensional printing/ Guided Tissue Regeneration	Adrenergic Neurons/ Dopaminergic Neurons/ Nitrogenic Neurons/ Nerve Tissue/ Induced pluripotent		–	211	
Scopus					388	
4 Keywords						
PubMed	Bioprinting/ Three-Dimensional printing/ Guided Tissue Regeneration	Brain/ Neurons/ Motor Neurons/ Serotonergic Neurons/ GABAergic Neurons/ Adrenergic Neurons/ Dopaminergic Neurons/ Nitrogenic Neurons/ Nerve Tissue/ Induced pluripotent	Disease	Neuroglia/microglia Coculture Techniques/ Coculture Neuroglia Neuroglia/microglia Coculture Techniques/ Coculture Neuroglia Neuroglia/microglia Coculture Techniques/ Coculture Neuroglia	17 34 76 3 14 4 21 37 12	
Web of Science						
Scopus						

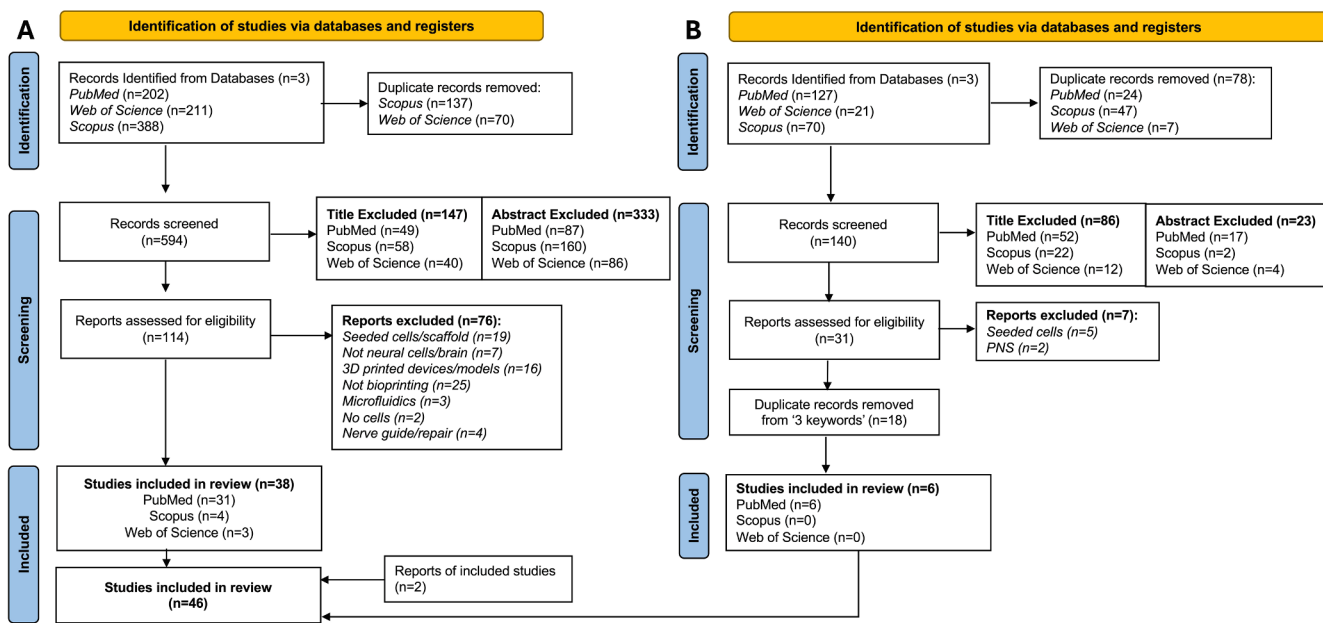


Fig. 2. Systematic screening process based on PRISMA Guidelines for both 3 keywords ‘3D bioprinting’, ‘neuronal cells/brain models’, and ‘diseases’ (A) and 4 keywords with the addition of ‘co-culture’ (B). The total included articles (n = 46) for the systematic review are compiled at the bottom of (A).

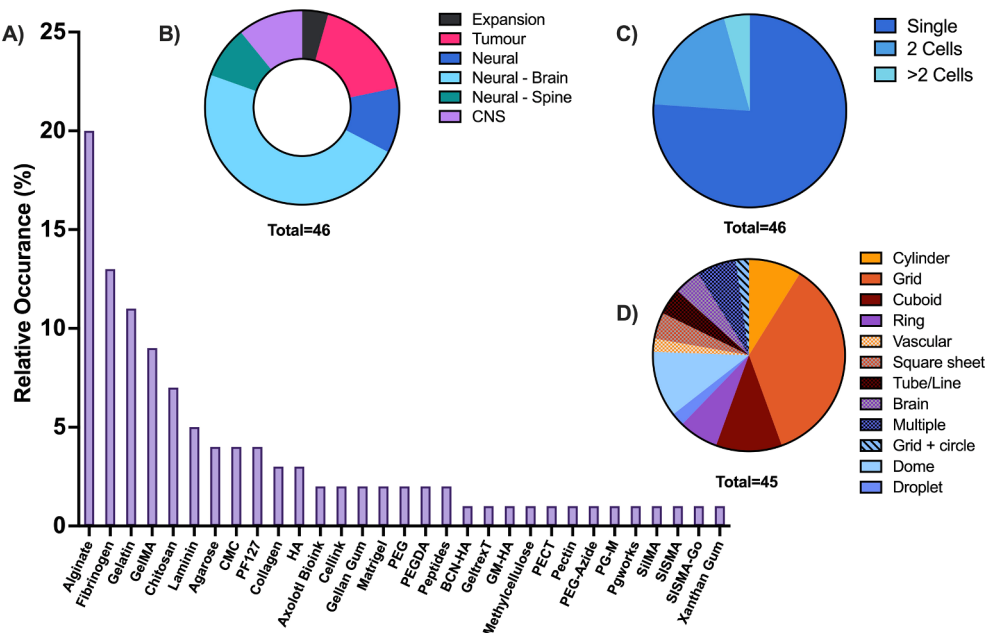


Fig. 3. Results from systematic search on (A) bioink compositions, (B) types of models, (C) number of cells printed and (D) construct shapes. The total included articles was n = 46, but one study did not report the constructed geometry (n = 45).

design and functionality is discussed in Section 3.2. One limitation in the reporting on bioinks here was that commercial bioinks (Axolotl and Cellink bioinks, Geltrex, and Pgworks) were reported as a single entity, without reporting their composition. For example, Axolotl bioink is a fibrin-based bioink, but it was not reported for fibrinogen percentages. Therefore, there is likely an underreporting of the percentages of certain polymers. In addition, in Abdelrahman *et al.* used two peptides to form their bioink, but this was only recorded as “peptides” once [11].

3.1. Models

The 46 papers included four that discussed spinal models directly, whereas the remaining 43 papers discussed neural tissues focusing on

the brain (n = 22), tumour models – including glioblastoma/gliomas (n = 8), or more broadly discussed models of the CNS (n = 5), and “neural” models (n = 5) (Fig. 3B). Other models include those that were used for cellular expansion (n = 2) and spinal models (n = 4). Models that conducted 3D bioprinting for applications such as nerve repair and guidance or the peripheral nervous system were excluded. A majority of the 3D bioprinted materials printed one cell type (n = 36), followed by co-printing with two cells (n = 9); only two papers printed more than two cell types (Fig. 3C). The geometries that were bioprinted varied, and typically correlated to the model/function of the 3D bioprinted neural tissues. Most often, grid constructs were formed (n = 16), followed by dome-shaped (n = 6), cuboid (3D rectangular lattices, n = 5), cylindrical (n = 4), ring (n = 3), brain geometry (n = 2), square sheets (n = 2), tube/

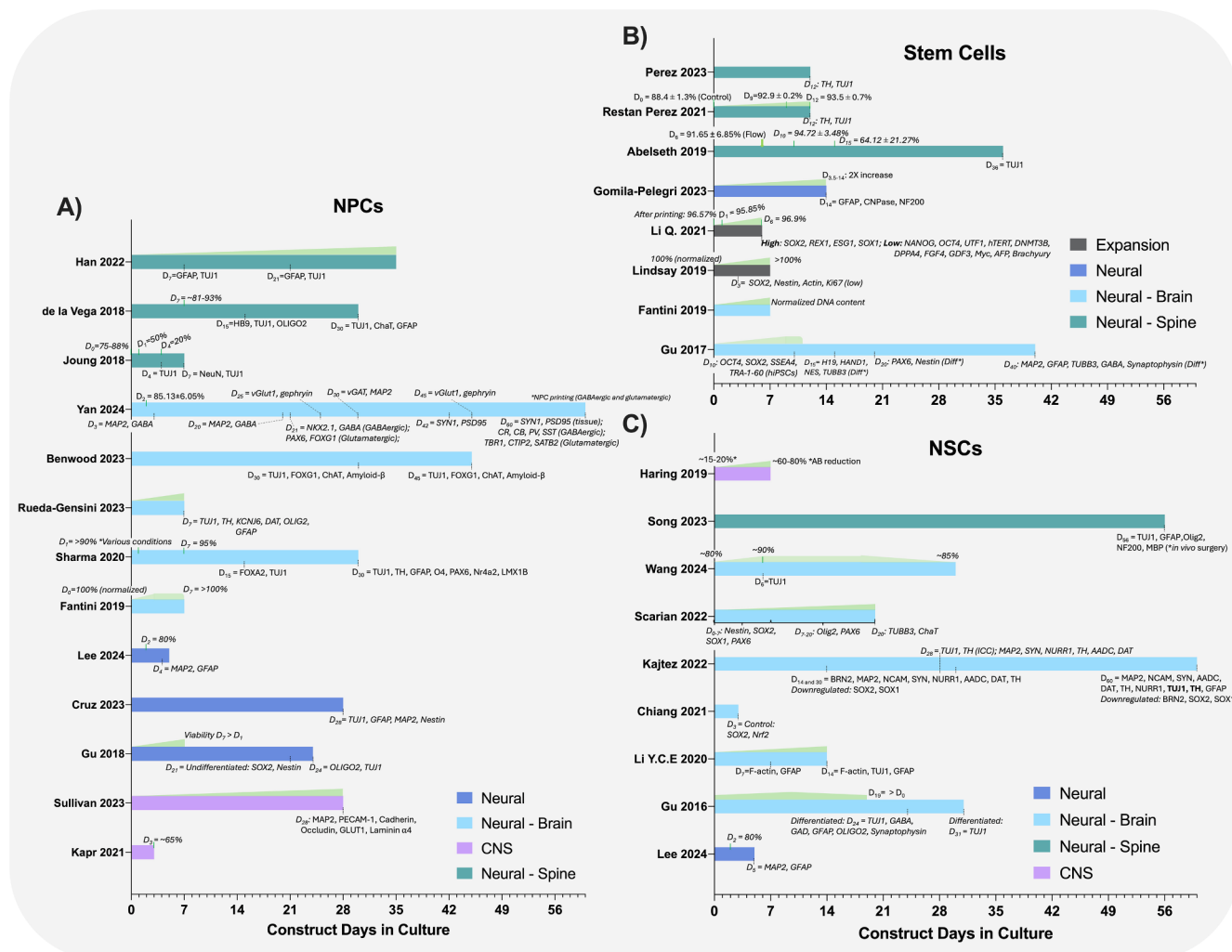


Fig. 4. Summary of select cellular characterization assessments (viability and protein expression) for cells that were 3D bioprinted over various days in culture. Summaries are divided by stem cell-like cell types of A) NPCs, B) stem cells (hiPSCs, MSCs, ADSCs), and C) NSCs. Viability measurements are shown on top; if no quantitative numbers were given, the general trends are shown (green). Summary of protein markers (ICC/RT-qPCR) are shown below each bar at relevant days assessed. Colours indicate the neural model application. (For interpretation of the references to colour in this figure legend, the reader is referred to the web version of this article.)

line ($n = 2$), droplet ($n = 1$), vascular ($n = 1$), and a combination of circular and grid-shaped ($n = 1$) (Fig. 3D). Three papers printed multiple construct architectures that were bioprinted with cells.

The reviewed literature is discussed next, summarizing the main findings of the relevant papers by model type. An analysis of the mechanical and cellular characterization techniques is provided later in more detail in section 3.5. The main findings related to cellular analysis regarding viability and protein expression are summarized to supplement the text to intuitively compare similar models and cell types (Figs. 4 and 5). The cellular-based characterization summaries are sectioned by cell type: those using immature cells, such as stem cells, neural progenitor cells (NPCs), and neural stem cells (NSCs), and more mature lineages related to tumour cells (glioblastoma, glioma, neuroblastoma), glial cells (Schwann, astrocytes, oligodendrocytes) and neurons. The 'stem cells' include those that have the potential to differentiate into multiple lineages, including hiPSCs, mesenchymal stem cells (MSCs), and adipose-derived stem cells (ADSCs). In the literature, we noted that inconsistencies exist between the use of the terms 'NPCs' and 'NSCs', but we aimed to differentiate NSCs as being those sourced directly without differentiation (e.g., mouse-derived stem cells). Interestingly, one paper referred to their cells as "neural stem/progenitor cells (NSPCs)", emphasizing this variation [95].

Inconsistencies in the literature were largely associated with the discrepancy of terms or methods relating to characterization. Most commonly, there was an incongruity in using β III tubulin or TUJ1, or other variations to identify neural lineage. Several reported variations were noted, where typically analysis with reverse transcriptase quantitative polymerase chain reaction (RT-qPCR) referred to class III beta-tubulin protein (TUBB3), but immunocytochemistry (ICC) or similar methods referenced α T-III, β III-tubulin, β -tubulin III, β -III-tubulin, among others. Throughout the text, we aimed to state the terms used within the respective article, but for comparison consistencies, the outlined tables and figures include 'TUJ1' as a representative term. It should be noted that inconsistencies in nomenclature may inhibit intuitive comparative analyses using systematic screening, which may be a bias in our review search.

3.1.1. Brain

Modeling the brain offers fundamental insights into the intricacy of biological and chemical pathways, including understanding the complex pathophysiology of neurological and neurodegenerative disorders such as Alzheimer's disease, Parkinson's disease, and Huntington's disease, among others. 3D bioprinted tissue constructs must recapitulate the multifaceted sophistication of the brain, which is a non-linear entity,

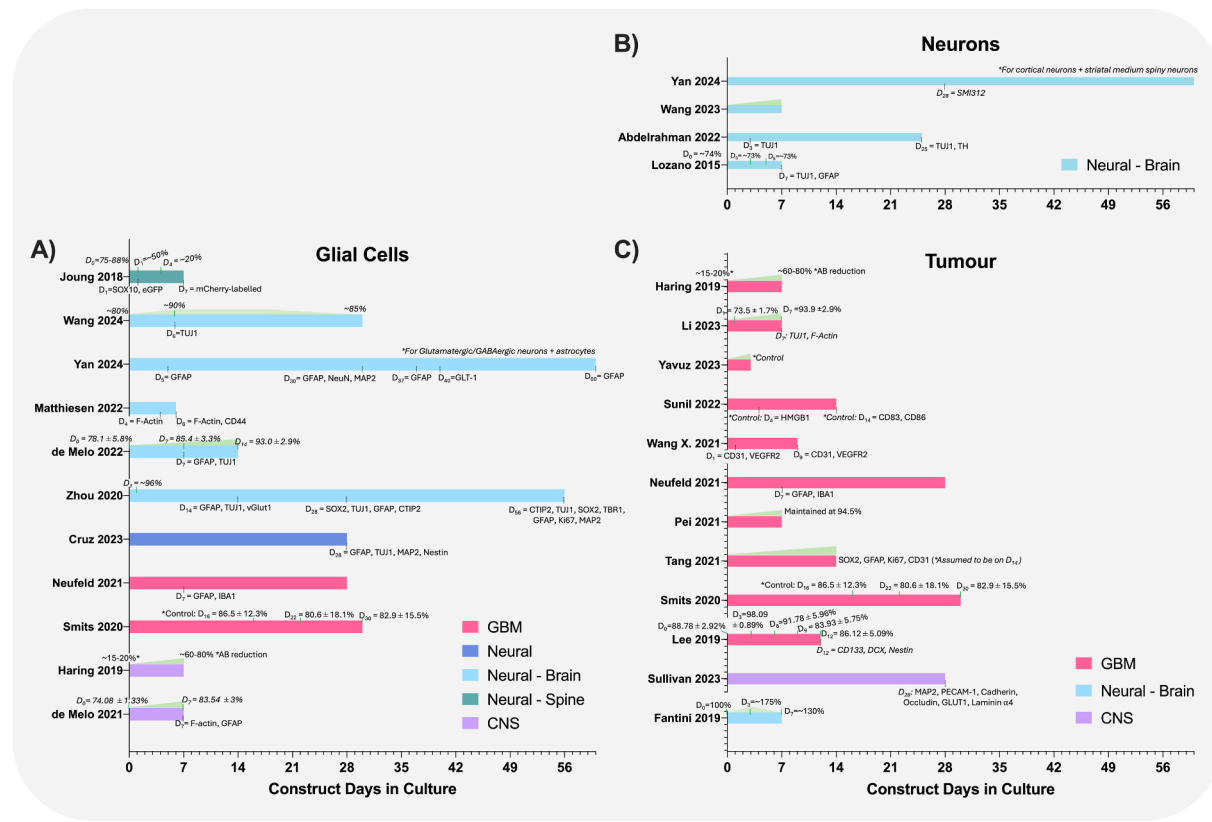


Fig. 5. Summary of select cellular characterization assessments (viability and protein expression) for cells that were 3D bioprinted over various days in culture. Summaries are divided by matured/limited lineage of A) glial cells, B) neural cells, and C) tumour cells (GBM, glioma, neuroblastoma). Viability measurements are shown on top; if no quantitative numbers were given, the general trends are shown (green). Summary of protein markers (ICC/RT-qPCR) are shown below each bar at relevant days assessed. Colours indicate the neural model application. (For interpretation of the references to colour in this figure legend, the reader is referred to the web version of this article.)

composed of varying stiffnesses, cell types and functions.

The level of sophistication of 3D bioprinted neural tissue models has increased in the last decade, which shows promise for the future bioengineering of 3D bioprinted neural tissues. In 2015, Lozano *et al.* conducted semi-manual “3D bioprinting” using a coaxial needle, combining manual extrusion of the bioink and a syringe pump for the crosslinker [96]. Their neural model used an Arg-Gly-Asp (RGD)-modified gellan gum (RGD-GG) printed with mouse primary cortical neurons, which increased cell adhesion and differentiation of primary cortical neurons into both neurons (β III tubulin+) and glial cells (GFAP+, glial fibrillary acid protein) after 7 days (Table 2). No modulus mechanical characterizations were done, but they attributed the differentiation to the sufficient mechanical support of the hydrogels to maintain 3D structure and suitable porosity that permitted the exchange of nutrients and cellular debris (shown through a BSA diffusion study), which promoted cell growth and neurite extension, even extending into cell-absent printed layers. Also focused on cortical tissues, Zhou *et al.* conducted a non-conventional printing method using droplet printing to achieve soft, but mechanically stable matrices to bioprint human cortical cells in Matrigel [97]. They were able to print high-viscosity biomaterials using a customized driver, and when dropped into a lipid-containing oil bath, a lipid-bilayer supported network was formed which maintained the 3D architecture. The droplets were conserved as distinct chambers during printing, and upon media exchange, aging, and incubation, 3D geometries of Matrigel (representing the ECM) and cells remained. The printed tissues using human neural stem cells (hNSCs) with and without astrocytes were cultured in media (containing B-27, neurotrophin-3 – NT3, and brain-derived neurotropic factor – BDNF) for up to 14 days. Alone, the hNSCs showed neuronal migration, differentiation, axon outgrowth, and astrogenesis, and importantly, pre-

patterning arrangements of astrocytes and hNSCs indicated key biological functions regarding neurogenesis and astrogenesis. When hNSCs were centrally printed bordered by empty ‘ECM’, hNSCs began to migrate to the empty space by day 14, expanded by day 28 (CTIP2+, TUJ1+, SOX2+), and saw astrogenesis by day 56, but astrocytes (GFAP+) remained within the empty compartments. Similar results were found if astrocytes were printed within the centre; they tended to migrate away from the proliferating hNSCs. This, in combination with progenitors (SOX2+) aligning along the bundle, suggested astrocyte-induced neural fasciculation and axon-guided cell migration. Further, the presence of various markers relating to progenitors (SOX2+), young neurons (TUJ1+), deep-layer cortical neurons (CTIP2+), sub-plate neurons (TBR1+), and differentiated neurons (MAP2+, microtubule-associated protein 2) and proliferating cells (nuclear proliferation marker, Ki67+) recapitulated the aspects of cortical development.

In 2016, Gu *et al.* bioprinted frontal cortical hNSCs within a bioink made of alginate, carboxymethylcellulose (CMC) and agarose [98]. Cell survival and proliferation were largely influenced by CMC concentration due to the effect CMC had on porosity, but 5 % w/v CMC was found to be favourable. In the absence of differentiation factors, the bioprinted hNSCs remained undifferentiated after 3 weeks – expressing SOX2, vimentin, Nestin, and Ki67, with limited expression of GFAP, OLIGO2, or TUJ1. Adding induction molecules to the media (StemPro, N2, and BDNF) produced cells that expressed high levels of TUJ1, γ -Aminobutyric acid (GABA), glutamic acid decarboxylase (GAD), GFAP, OLIGO2, and Synaptophysin, and low SOX2 by 24 days (14 days of differentiation). TUJ1+ staining was performed at 31 days post printing (21 days of differentiation); it was unclear if only TUJ1+ was stained, or if the other markers were not present. Importantly, 3D bioprinted models were associated with higher expression of neural and neuroglial

Table 2

Summary of the included articles that model the brain.

Source	Printed Bioink Composition		Cells	Construct Media	Bioprinter	Characterization	
	Bioink	Crosslinker				Bioink	Cells/Construct
Lozano <i>et al.</i> , 2015 [96]	RGD-Gellan gum (RGD-GG; 0.5 % w/v)	DMEM (5X; $\text{CaCl}_2 = 9 \text{ mM}$, $\text{MgSO}_4 = 4.05 \text{ mM}$), or CaCl_2 (1 M)	Mouse primary cortical neurons (1×10^6 cells/mL)	Complete neurobasal media	Handheld printing (coaxial needle; 0.2 mm ID, 1 mm OD; 0.1 mL/min)	SEM (RGD-GG) <i>Diffusion study</i> (labelled BSA) <i>Consistency</i> (extrusion force) <i>Modulus</i> (compression, EComp, Indentation, EOmd) <i>Diffusion study</i> (labelled BSA) SEM (surface/internal porosity)	Viability (Live/dead; 2 hr, D3, 5) ICC (TUJ1, GFAP, DAPI; D7) SEM (RGD-GG) Viability (Live/dead; D1, 3, 5, 7, 9, 11) hNSC proliferation (PrestoBlue) ICC (GFAP, SOX2, vimentin, OLIGO2, Ki67, TUJ1, Nestin, synaptophysin, GABA, GAD, DAPI; D21, 24, 31) RT-qPCR (TUJ1, GFAP, OLIGO2, SYP, GABA, NKX2.1, MYST, VGLT, SERT, PET-1, β -Actin; D21) Calcium imaging (Fluo-4, bicuculline) SEM (cell adhesion and position)
Gu <i>et al.</i> , 2016 [98]	Alginate (5 % w/v), carboxymethyl-chitosan (CMC; 5 % w/v), agarose (1.5 % w/v)	CaCl_2 (2 % w/v, 10 mins)	Frontal cortical hNSCs (5×10^6 cells/mL)	Differentiation media ^a , P/S (P = 100 U/mL, S = 100 ug/mL)	EnvisionTEC GmbH (200 μm printing nozzle; 1.5–2.0 bar)		
Gu <i>et al.</i> , 2017 [99]	Agarose (1.5 %), alginate (2 %), CMC (5 %)	CaCl_2 (2 %) for 10 min	Human iPSCs (8×10^7 cells/mL)	hiPSC expansion = mTESR1, Y-27632 ^b EBs induction ^c Neural induction medium ^d Neural differentiation medium ^e	3D-Bioplotter® System (EnvisionTEC; 200 μm printing nozzle)	SEM *Material characterized previously	Viability (Live/dead; D1, 3, 7) Cell proliferation (PrestoBlue; D1, 3, 5, 7, 9, 11) Calcium imaging (D40) RT-qPCR (OCT4, NANOG, TDGF1, UTF1, H19, HAND1, NES, PDX1, IGF2, TUBB3; D15) Flow cytometry (OCT4, SSEA4, TRA-1–60 and SOX2) ICC (OCT4, SSEA4, TRA-1–60, PAX6, Nestin, Synaptophysin, TUJ1, GABA, GFAP, MAP2, SOX2, DAPI; D3, 7, 14, 40)
Gu <i>et al.</i> , 2018 [100]	Agarose (1.5 %), alginate (5 %), CMC (5 %)	CaCl_2 (2 %) for 10 min	hNSC cell line (1×10^7 cells/mL)	hNSC differentiation medium ^f	3D-Bioplotter® System (EnvisionTEC; 1.5–2.0 bar)	*Material characterized previously	Viability (Live/dead; D1, 7) ICC (Undifferentiated = D10; Differentiated = D24; Nestin, TUJ1, OLIGO2, SOX2, GFAP, vimentin, synaptophysin, GABA, GAD, DAPI) Calcium imaging
Fantini <i>et al.</i> , 2019 [101]	Alginate (6 %), gelatin (4 %)	CaCl_2 (2 %, 5 min)	SH-SY5Y (5×10^4 cells/mL) hiPSCs NSCs derived from hiPSCs (2×10^6 cells/mL)	DMEM, FBS (15 %), P/S (100 U/mL /100 mg/mL), and L-glutamine (2 mM)	CELLINK INKREDIBLE+ (grid constructs; 0.41 mm nozzle; 25 °C, 37 °C; 30–70 (kPa); 600 mm/min; 0.4 mm LH)	Repeatability tests (3 days)	Viability (SH-SY5Y cells; D5) ICC (GAPDH, α -Tubulin, DAPI) 3D bioprinted constructs: Viability (Live/dead for iPSC/NSC; D0, 3, 7)
Abelseth <i>et al.</i> , 2019 [102]	Alginate (5 mg/mL), genipin (0.3 mg/mL), fibrin (20 mg/mL)	CaCl_2 (20 mg/mL), chitosan (0.75 mg/mL), thrombin (10 U/mL)	hiPSC-derived neural aggregates (NAs; 10,000 cells/aggregate)	D17: Gradually from neural induction media to neural basal media, puro (0.5 μm) and RA (0.25 μm)	Aspect Biosystems' RX1 with DUO-1 Printhead	–	Viability (Live/dead; D10, 15; Flow cytometry – Guava ViaCount assay; D6) ICC (TUJ1, GFAP, DAPI; D30, 41)

(continued on next page)

Table 2 (continued)

Source	Printed Bioink Composition		Cells	Construct Media	Bioprinter	Characterization	
	Bioink	Crosslinker				Bioink	Cells/Construct
Y.-C. E. Li <i>et al.</i> , 2020 [108]	Gelatin methacryloyl (GelMA; 4 % w/v), gelatin (1 % wt), alginate (0.5 % wt), PI (0.25 % wt), GelMA (5 % wt) in HBSS (40 % v/v) and MEM (60 % v/v), laminin (10 µg/mL)	Support bath: DMEM, CaCl ₂ (11 mM), PI (0.25 % wt), GelMA (5 % wt) in HBSS (40 % v/v), astrocyte complete media (60 % v/v) ^g	Rat neural cells derived from neuroepithelial cells (25x10 ⁶ cells/mL)	MEM complete media = MEM, FBS (10 %), P/S (1 %) +/- RA (1 µM)	CELLINK INKREDIBLE (30 G needle; 3 µL/min)	Compressive moduli Rheology (viscosity, oscillatory stress sweep, oscillatory time sweep) Printability	Viability (Live/dead) Cell metabolic activity (Presto Blue Reagent; D1, 3, 7, 14) ICC (TUJ1, GFAP, DAPI, F-actin; D5, 7, 10, 14) Glutamate Assay (Glutamate assay kit)
Sharma <i>et al.</i> 2020 [103]	Fibrinogen (20 mg/mL), alginate (0.5 % w/v), genipin (0.3 mg/mL), chitosan (0.075 % w/v), thrombin (1.7 U/mL)	UV crosslinked (60 s) CaCl ₂ (20 mg/mL), chitosan (0.075 % w/v), thrombin (1.7 U/mL)	NPCs derived from hiPSCs (1 x10 ⁶ cells/mL)	PLO/laminin coated plates, STEMdiff™ Neural Progenitor Media (EGF, bFGF), AAS (1 %) D10: STEMdiff™ Neural Induction Medium, AAS (1 %) D20: Brain Phys Neuronal Medium	Aspect Biosystems RX1 dome shaped constructs; rectilinear infill; 6 layers; 25 mm/s; 50 mbar (bioink), 60 mbar (crosslinker), 100 mbar (buffer)	-	Microscopy Viability (Flow cytometer + Guava ViaCount reagent®; D1, 7) ICC (FOXA2, TUJ1, TH; DAPI; D15, 30) Flow Cytometry (TUJ1, O4, TH, GFAP; D30) RT-qPCR (TUJ1, TH, Nr4a2, PAX6, LMX1B; D30)
Zhou <i>et al.</i> , 2020 [97]	Matrigel Print bath: DPhPC (4 mg/mL) in a mixture of undecane and silicone oil AR20	30 min room temperature	iPSC-derived: hNSCs Red-fluorescent-protein-labeled hNSCs (RFP-hNSCs) Human cortical neurons (hCNs) Human primary astrocytes (hAs) *Cell densities ranged up to 3.5x10 ⁷ cells/mL)	hNSCs constructs: Neural Maintenance Media = 1:1N-2 medium ^h to B-27 medium ⁱ hCN constructs: comp:GCN medium ^j , + variations (Y-27632 (10 µM) and/or doxycycline (1 µg/mL))	Droplet printing (piezo-electric driver; Peltier-based temperature-controlled stage; coated glass printing nozzle)	Ejected droplet size and nozzle diameter	Viability (Live/dead; D1, 4, 8, 14, 28) ICC (TUJ1, GFAP, CTIP2, MAP2, Ki67, NeuN, CAM, DAPI, D100) Calcium imaging (Fluo-4 Direct calcium assay kit; D4, 44, 65) Cell migration (fluorescence-labeled cells; D3, 14) hAs Segregation Analysis (ICC: TUJ1, GFAP, SOX2) Process Analysis (Density, length, bundle with ICC (TUJ1))
Chiang <i>et al.</i> , 2021 [109]	CELLINK bioink	Crosslinking solution (5 mins)	Human neural stem cells (1x10 ⁷ cells)	NSC Serum free media (SFM) ^k 3 parameters: (1) NSC SFM (72 hrs) (2) A _{f1-42} (5 µM; 24 hrs), NSC SFM (48 hrs) (3) A _{f1-42} (5 µM; 24 hrs), AuNPs (10 ppm; 48 hrs)	CELLINK INKREDIBLE bioprinter (22 G needle; 10–20 kPa)	*TEM and FTIR done previously	SEM Viability (<i>in vitro</i> Sulforhodamine B (SRB)-based assay kit) ELISA (TNF-α, IL-1β) qPCR (IKKα, IKKβ, p65, iNOS, COX2, Nrf2, SOD1, SOD2, Gpx, Catalase, HO-1, HSP27, HSP70) Western blot (p65, lamin) ICC (SOX2, Nrf2) *Various AuNP-related characterization ^l
Restan Perez <i>et al.</i> , 2021 [104]	Fibrinogen (20 mg/mL), alginate (0.5 % w/v), genipin (0.3 mg/mL)	CaCl ₂ (20 mg/mL), chitosan (0.075 % w/v), thrombin (1.7 U/mL)	Human adipose-derived MSCs (2 x 10 ⁶ cells/mL)	PLO/Laminin coated plate with MSC media D0-D9: Control Media or Differentiation Media ^m D9-12: BDNF (50 ng/mL) to differentiation group	Aspect RX1 with LOP™ printhead (half spherical constructs; 7 layers; 40 % rectilinear infill; 60 mbar (crosslinker), 50 mbar (bioink), 100 mbar (buffer); 25 mm/s)	*Characterized previously	Microscopy (Phase, D0, 4, 9, 12) Viability (Live/dead; D0, 9, 12) ICC (TUJ1, TH, DAPI; D12) Dopamine release (ELISA; D12) Electrical properties (voltage sensitive dye)

(continued on next page)

Table 2 (continued)

Source	Printed Bioink Composition		Cells	Construct Media	Bioprinter	Characterization	
	Bioink	Crosslinker				Bioink	Cells/Construct
de Melo et al., 2022 [110]	GGFL = Gelatin (4 % w/v), GelMA (2 % w/v), fibrinogen (3 mg/mL), laminin (2 µg/mL), PI (Irgacure 2959, 0.5 %)	Thrombin (1 U/mL), CaCl ₂ (10 % w/v; 90:1 thrombin: Ca ²⁺) UV Crosslinking (2 x 60 s)	Murine cortical astrocytes (1x10 ⁶ cells/mL) Mature murine neurons seeded on top (1x10 ⁴ cells)	D0-7: Astrocyte culture medium D7: media removed, soaked in laminin (30 µg/mL), seeded with mature neurons; media = astrocyte culture medium, neuronal medium (1:1) Infected with either SARS-CoV-2 (0.2 MOI) or MA-SARS-CoV-2 (0.2 MOI); 2 h	3D bioprinter (3D Biotechnology Solutions; 22 G; 400 mm/min; 25 °C)	Rheology (temperature sweep, shear viscosity, frequency sweep) Mechanical (mechanical compression, Young's modulus) SEM (surface) Physical characterization (degradation, porosity)	Viability (Live/dead; D0, 7, 14) ICC (spike S1, MAP2, TUJ1, GFAP, ACE2, DAPI; D7)
Abdelrahman et al., 2022 [11]	Ac-Ile-Val-Cha-Lys-NH2 (IVZK; 13 mg/mL) Ac-Ile-Val-Phe-Lys-NH2 (IVFK; 13 mg/mL)	N/A	Ventral midbrain DA and non-DA neurons (suspended in 1X PBS)	N2 Media	Custom 3D bioprinter 37 °C; three variations (none, half molded, fully molded); 10–20 µl/min flow rate; 24 layers (cells extruded in top 2 layers)	SEM TEM Raman spectroscopy AFM *Other assessments done previously Printability	Viability (Live/dead; D1, 2, 3) Metabolic activity (CellTiter-Glo® 3D Cell Viability Assay; D2, 3) ICC (TUJ1, TH, TBR1, CD31, DAPI) Neurite Outgrowth (NeuronJ) Neurosphere migration assay (ICC: TUJ1, TH, DAPI; D3) Neuronal activity (MEAs; up to D42) 6-OHDA Hydrochloride Treatment (Live/dead, ATP assay, ICC for TH) qPCR (Th, Nurr1, En1, Lmx1a, Pitx3; D3) 3D bioprinted constructs: Viability (Live/dead; D3) ICC (TUJ1; D3) ICC (TUJ1, TH, GFAP, DAPI; 1 and 2 month) RT-qPCR (BRN2, SOX1, SOX2, NURR1, AACD, DAT, TH, SYN, MAP2, NC; 1 month) Calcium imaging (Fluo3 AM; 2 months) Whole-cell patch-clamp recordings (cells with neuronal morphology and round cell body positive for synapsin-GFP) 3D Oxygen Mapping (oxygen mapping microbeads, live staining; D2 to D50)
13 Kajtez et al., 2022 [65]	Growth medium, Xanthan gum (0.1 %)	Support system: Jammed microgels = Alginate (0.5 % w/v), CaCO ₃ (1 mg/mL), collagen (1 mg/mL), laminin (2 µg/mL), fibronectin (5 µg/mL), HA (100 µg/mL) Dispersed microgels = jammed microgels:cell culture media (2:1)	hNSCs (9x10 ⁶ cells/mL)	Growth Medium ^b D1: Differentiation medium ^c	3D Discovery bioprinter (RegenHU; 27G; 4 °C; 3.6 µL/min (extrusion), 0.3 mm/s (lateral))	Rheology (frequency sweep, viscosity, stress sweep, time sweep, temperature sweep)	Viability (Live/dead; D3) ICC (TUJ1, TH, GFAP, DAPI; 1 and 2 month) RT-qPCR (BRN2, SOX1, SOX2, NURR1, AACD, DAT, TH, SYN, MAP2, NC; 1 month) Calcium imaging (Fluo3 AM; 2 months) Whole-cell patch-clamp recordings (cells with neuronal morphology and round cell body positive for synapsin-GFP) 3D Oxygen Mapping (oxygen mapping microbeads, live staining; D2 to D50)
Scarian et al., 2022 [111]	CELLINK bioink (cellulose nanofibrils, alginate)	Crosslinking agent (CELLINK)	hNSCs (6x10 ⁵ cells/mL)	D0-14: Neurobasal medium, expansion medium D14-21: MNP Differentiation Medium ^d D21-28: iMNs differentiation medium ^e D28-35: MNs differentiation medium ^f	Bioplotter BioX (CELLINK; grid construct; 23 G nozzle; 25 °C; 600 mm/min; 45–70 kPa)	Hydrogel moisture % Swelling test Porosity % (Liquid displacement)	Viability (Live/dead; D0, 3, 7, 10, 14, 20) ICC (Nestin, SOX2, SOX1, PAX6, Oligo2, TUBB3, ChAT, DAPI) RT-qPCR (Nestin, SOX2, SOX1, PAX6, TUBB3, MAP2) Electrophysiological analysis (c-fos marker; D0, 1, 4, 7, 11, 14)
Chrenek et al., 2022 [106]	(1) High viscosity, fibrin-based bioink – TissuePrint-HV Kit (Axolotl Biosciences) (2) Alginate (2 % w/v), gelatin (2 % w/v)	(1) TissuePrint Crosslink (Axolotl Biosciences) (in agarose support bath*) (2) CaCl ₂ (2 %)	hiPSCs, MSCs, or U-87 GBMs (1x10 ⁶ cells/mL)	Cell culture media or TBS (without cells)	BioX (CELLINK) (grid lattice, others; 22G) TissuePrint-HV kit: Support bath = 10/11 kPa, 15 mm/s Pre-crosslinked = 5 kPa, 10 mm/s	–	–

(continued on next page)

Table 2 (continued)

Source	Printed Bioink Composition		Cells	Construct Media	Bioprinter	Characterization	
	Bioink	Crosslinker				Bioink	Cells/Construct
Matthiesen et al., 2023 [112]	Azide-terminated polyethylene glycol – (PEG-Az) ₈ (1 % w/v)	HA- bicyclo [6.1.0]nonyne (HA-BCN) modified with 1 mM cRGD or IKVAV (1 % w/v)	Human fetal primary astrocytes (FPA; 2x10 ⁵ per 100 µL)	ScienCell astrocyte media, FBS (2 %), Astrocyte growth supplement (1 %), P/S (1 %) High Glucose DMEM, FBS (10 %), P/S (1 %)	Alg/Gel: 20 kPa, 20 mm/s CELLINK BioX (grid structure)	Rheology (strain sweep, frequency sweep, time/ temperature sweep) SEM (internal)	Viability (AlamarBlue; D1, 3, 6) qPCR (Vimentin, PAX, ITGB1, PTK2, CD44, GFAP, S100B, GAPDH) ICC (CD44, F-actin, Hoechst) 3D bioprinted construct: ICC (F-actin, Hoechst; D4)
Perez et al., 2023 [105]	TissuePrint – Low Viscosity (LV; Axolotl Biosystems) TissuePrint – Hight Viscosity (HV; alginate/fibrin; Axolotl Biosystems)	Component 2 (genipin)	MSCs (2-10x10 ⁶ cells/mL)	PLO/Laminin, Control and Experimental media ^s D –1: complete MSC media D0: respective media; no media change until D9 D9: BDNF (50 ng/mL) to experimental group	BioX (CELLINK; dome; 10 x 3 mm; 20–25 %; rectilinear infill) RX1 (Aspect Biosystems; LOP™ printhead; 40 % rectilinear infill)	*LV characterized previously	Viability (Live/dead; D9, 12) ICC (TUJ1, TH, DAPI; D12) Electrophysiology (FLIPR Membrane Potential Assay Kit) Dopamine release (ELISA; D12)
Gomila Pelegri et al., 2023 [2]	PEG, RGD and YIGSR (Tyr-Ile-Gly-Ser-Arg) peptides = 1.1 kPa	—	Human adipose-derived stem cells (ADSCs; 1x10 ⁶ cells/mL)	DMEM/F12, GlutaMAX, FBS (10 %), AAS (1 %) Changed every 84 hr	RASTRUM bioprinter (~1.1 kPa)	Stiffness (unknown method)	Morphology (Incucyte imaging) Viability (AlamarBlue; D3.5, 7, 10.5, 14) ICC (GFAP, CNPase, Neurofilament 200; D14) Protein analysis (Proteomics, LC-MS/MS; D14)
Cruz et al., 2023 [116]	'4GMA_Gx' = Geltrex, GelMA (8 wt%; 1:1 v/v)	PI (Irgacure; 0.5 % w/v)	Murine cortical astrocytes (4x10 ⁶ cells/mL) hiPSC-derived NPCs (14.5x10 ⁶ cells/mL) Neuroblastoma cells (SH-SY5Y; 2x10 ⁶ cells/mL)	NPCs = Neural maturation media ^t Astrocytes = astrocyte cell medium or NSC medium ^u	3DBS Educational Starter Printer (4x4x1 mm)	*Various combinations of bioink tested Compression test (Instron) Degradation (D1, 3, 7) Rheology (temperature sweep, viscosity) SEM (surface)	Cell proliferation (Resazurin assay; D2, 5, 6) qPCR (ACTB, SOX2, Nestin, NANOG, TUBB3, MAP2, vGlut1) 3D bioprinted construct: ICC (DCX, TUBB3, SOX2, MAP2, GFAP, DAPI; astrocytes = D3, 5, 10, NPCs = D28; after differentiation = D17, 24)
J. Li et al., 2023 [117]	Alginate (2 % w/w), Pluronic F127 (30 % w/w), tetrapodal-shaped-ZnO microparticles (t-ZnO; 0.025 %)	CaCl ₂ (2 % w/w); 1 min CaCl ₂ (1.5 % w/w) the following day/before viability testing	Neuroblastoma (SH-SY5Y)-derived dopaminergic neurons (3x10 ⁶ cells/mL)	Cell culture medium: P/S (20 U/mL / 20 µg/mL), heat inactivated fetal calf serum (15 % v/v), DMEM/F-12	3D Discovery printer (RegenHU; circular grid; 21 G needle)	Rheology (frequency sweep) SEM (surface) Photoluminescence spectroscopy Material properties (FTIR, XPS) Dopamine Sensing	Viability (Live/dead; D7) ICC (TUJ1, F-actin, DAPI; D7)
Z. Wang et al., 2023 [113]	Pluronic F127, poly(ethylene glycol) diacrylate (PEGDA, Mn = 700)	UV light	HT22 cells (2x10 ⁶ cells/mL GelMA)	DMEM, FBS (10 %), P/S (1 %)	3D extrusion printer EFL-BP-6602 (custom-made coaxial extrusion head; 17 G OD, 22 G ID; cuboid structure; 16 L x 16 W x 6H mm; 3 layers; 0.74 mL/min (inner), 2.21 mL/min (outer); 37 °C)	SEM (internal) Swelling behaviour FTIR Diffusion (Eosin Y, up to 24 hrs) Rheology (temperature sweep, viscosity, shear recovery, storage and loss moduli)	Viability and proliferation (Live/dead, CCK-8; D1, 7) Compression modulus
Rueda-Gensini et al., 2023 [10]	SISMA SISMA-GO	Blue light irradiation (1 min)	DA neurons differentiated from Lund human mesencephalic	Differentiation medium; media changes on D2, 5, 7 D7: constructs over immune co-culture (THP-1 monocytes:astrocytes, 2:1).	BioX (CELLINK; 13 °C (print head), 37 °C (print bed); 20 G (conical); 8 kPa)	Rheology (time sweep) Growth factor quantification (Quantibody™ Human Growth Factor Array)	Viability/Metabolic Activity (Alamar Blue; D0, 3, 7) Apoptosis (apoptosis; ROS production; MMP ¹ ; intracellular-syn immunostaining; D1, 2, 5)

(continued on next page)

Table 2 (continued)

Source	Printed Bioink Composition		Cells	Construct Media	Bioprinter	Characterization	
	Bioink	Crosslinker				Bioink	Cells/Construct
Benwood et al., 2023 [107]	Fibrinogen (20 mg/mL), alginate (0.5 % w/v), genipin (0.3 mg/mL), puro-loaded microspheres (1 mg/mL)	CaCl ₂ (20 mg/mL), chitosan (0.075 % w/v), thrombin (1.7 U/mL)	(LUHMES) NPCs (1x10 ⁷ cells/ml)	Media = LUHMES differentiation medium, A53T α-syn (10 µg/mL) D10: LUHMES differentiation medium, A53T α-syn (5 µg/mL)	RX1 with DUO™ printhead (Aspect Biosystems; dome-shaped constructs; 10 mm diameter, 5 mm high; 100 mbar (crosslinker), 90 mbar (bioink), 500 mbar (buffer); 25 mm/s 40 % rectilinear infill; 9 layers; cultured up to 45 days)	<i>Microspheres:</i> SEM (size/shape) <i>Encapsulation efficiency</i> (HPLC) <i>Polydispersity Index</i> (DLS)	<i>ICC</i> (CCR7, TUJ1, α-synuclein, GFAP, Hoechst; D1, 2, 7) <i>Flow Cytometry</i> (CD68, CD14) <i>qRT-PCR</i> (KCNJ6, DAT, TH, SYN1, GFAP, OLIG2, PINK1, PARKIN, DC-STAMP, CD206; D7) <i>Viability</i> (Live/dead; D1, 30, 45) <i>ICC</i> (FoxG1, ChAT, Aβ, Tau, TUJ1, DAPI; D30) <i>Electrophysiology</i> (FLIPR Membrane Potential Assay Kit; D30, 45)
H.-W. Lee et al., 2024 [95]	SilMA (15 % w/v), pectin (1 % PI (Irgacure 2959, 0.5 %)	UV Light (PI = 0.5 %, 30 s) Calcium ion solution (outer portion of coaxial, 1 M)	Rat primary cortical NPC spheroids (500 spheroids/mL)	Culture medium, bFGF (20 ng/mL)	Customized extrusion-based 3D printer (TL-D5 TMC2209; coaxial printing; 50–100 mm/min; 1–30 mm/s; 2x2 cm; 0–500 µm thick) Coaxial: bioink = 5 mm/min; crosslinker = 15 µL/min	<i>Gelation</i> <i>Swelling ratio</i> <i>Porosity</i> <i>SEM</i> (surface) <i>Compression</i> <i>Rheology</i> (viscosity, frequency sweep, strain sweep) <i>Printability</i> (continuity, design, Pr value)	<i>Biocompatibility/Proliferation</i> (MTT, LDH assays/CCK-8) <i>Viability</i> (Live/dead; D5) <i>ICC</i> (MAP2, GFAP, Nestin, Synapsin I; D5) 3D: <i>Viability</i> (Live/dead; D0, 5)
Yan et al., 2024 [14]	Fibrinogen (2.5 mg/mL), HA (1:2 HA:fibrinogen, 3 % w/v) <i>*Other variations assessed for printing</i>	CaCl ₂ (2.5 mM), thrombin (1U), transglutaminase (0.2 % w/v)	hiPSC-NPCs (1x10 ⁷ cells/mL fibrinogen)	D0: neural basal medium, B-27 (2 %), BDNF (10 ng/mL), GDNF (10 ng/mL), ascorbic acid (200 µM), cAMP (1 µM), CNTF (10 ng/mL; for printing with astrocytes); Y27632 (10 µM) added for the first 24 hrs	CELLINK INKREDIBLE+ (5 mm/s; 100 kPa; 30G (150 µm ID), 27G (200 µm ID)) CELLINK BioX (5 mm/s; 100 kPa; 30G (150 µm ID), 27G (200 µm ID))	<i>Gelation Time</i> <i>Printability</i> (Descriptive: Low, High, Intermediate)	<i>Viability</i> (Live/dead) <i>ICC</i> (calbindin, calretinin, CTIP2, DARPP32, drebrin, FOXG1, GABA, gephyrin, GFAP, GLT1, GFP, MAP2, mCherry, NeuN, NFKX2.1, OTX2, parvalbumin, PAX6, PSD95, S100β, SATB2, SMI312, somatostatin, SOX2, SYN1, TBR1, TUJ1, vGAT, vGlut1, Hoechst; D3, 7, 15, 20, 28, 30, 40, 60) <i>Synaptic puncta quantification</i> <i>Calcium and glutamate imaging</i> (GCaMP6 or iGluSnFR labelled; D14, 28, 42) <i>Optogenetic stimulation</i> (jRGECO1b labelled) <i>Electrophysiology</i> (whole cell patch clamp) <i>Viability</i> (Live/dead; D2, 4, 6, 12, 18, 24, 30) <i>ICC</i> (BIII-tub, DAPI; D6)
L. Wang et al., 2024 [115]	G5F0.5 = GelMA (5 % w/v), fibrinogen (0.5 % w/v) <i>*Other variations tested</i>	Thrombin (10 U/mL), CaCl ₂ (0.2 % w/v) UV light (15 s)	PC12 (4x10 ⁶ cells/mL) GL261 (2x10 ⁶ cells/mL)	Complete Culture Media ^a	Custom 3D bioprinter 24 °C 6 layers	<i>Compression</i> (Universal testing machine) <i>SEM</i> (surface)	<i>Viability</i> (Live/dead; D2, 4, 6, 12, 18, 24, 30) <i>ICC</i> (BIII-tub, DAPI; D6)

^a 1:1 DMEM/F12:Neurobasal, supplemented with StemPro (2 %), N2 (0.5 %), BDNF (50 ng/mL).^b ROCK inhibitor (Y-27632). Used for first 3 days.^c EB induction = DMEM/F12, K/O (20 %), MEM NEAA, B-mercaptoethanol (55×10^{-6} M).^d NIM = DMEM/F12 (1:1), 1 % N-2 (1 %), heparin (2 µg/mL), MEM NEAA.^e NDM = (2:1) DMEM/F-12 to Neurobasal Medium, StemPro Neural supplement (2 %), N-2 (0.5 %), BDNF (50 ng/mL).^f Differentiation medium = DMEM/F-12:Neurobasal Medium, 2:1 (v/v) supplemented with StemPro (2 %), N2 (0.5 %), BDNF (50 ng/mL).^g DMEM, 10% FBS, 1% P/S.

^h N-2 medium = DMEM/F12, 1 × N-2, 5 µg/mL insulin, 100 µM 2-mercaptoethanol, 1 mM GlutaMAX, 100 µM nonessential amino acids (NEAA), and 50 U/mL P/S.

ⁱ B-27 medium = neurobasal medium, 1 × B-27, 1 mM GlutaMAX, and 50 U/mL P/S.

^j Comp:GCN medium = neurobasal medium, GlutaMAX (1 mM), 2-mercaptoethanol (25 µM), B-27 (1X), NT3 (10 ng/mL), and BDNF (5 ng/mL).

^k StemPro® NSC SFM complete medium consists of KnockOut™ D-MEM/F-12 with 2 % StemPro® Neural Supplement, 20 ng/mL of EGF, 20 ng/mL of bFGF, and 2 mM of GlutaMAX™-I.

^l Reactive oxygen species (ROS; microplate reader); *Dihydroethidium staining*; *Nrf2 binding activity* (Colorimetric assay kit); *Superoxide dismutase activity* (SOD; SOD assay kit); *Glutathione peroxidase activity* (Gpx; colorimetric assay kit); *Total glutathione* (GSH; colorimetric assay kit); *Filter retardation assay* (β-amyloid, tau, Actin); *Proteasome activity assay*.

^m Control Media = Neurobasal Media (NB), B-27 (2 %), GlutaMAX (1 %), P/S (1 %); Differentiation Media = NB, B-27 (2 %), GlutaMAX (1 %), puro (250 ng/mL), FGF8 (100 ng/mL), bFGF (50 ng/mL), LDN-193189 (100 nM), SB431542 (10 µM).

ⁿ DMEM/F12 with GlutaMAX, glucose (30 × 10⁻³ M), HEPES (5 × 10⁻⁶ M), AlbuMAX (0.5 % w/v), L-alanine, L-asparagine monohydrate, L-aspartic acid, L-glutamin acid, and L-proline – each 40 × 10⁻⁶ M, N2 supplement (1 %), P/S (1 %), epidermal growth factor (EGF; 20 ng/L), fibroblast growth factor (FGF; 20 ng/L).

^o Growth medium without FGF or EGF, with N6,2-O-dibutyryladenosine 3',5'-cyclic monophosphate sodium salt (1 × 10⁻³ M) and GDNF (2 ng/L).

^p MNP Differentiation Medium = Neurobasal 2X, Advanced DMEM/F12 2X, Neural induction supplement 50X, RA (0.1 µM), Purmorphamine (0.5 µM).

^q Neurobasal 2X, Advanced DMEM/F12 2X, RA (0.5 µM), purmorphamine (0.1 µM), GDNF (10 ng/mL), IGF (10 ng/mL), BDNF (10 ng/mL).

^r MNP Differentiation Medium + Compound E (0.1 µM).

^s Control Media = NB, B-27 (2 %), GlutaMAX (1 %), P/S (1 %); *Experimental media* = control media, puro (250 ng/mL), FGF8 (100 ng/mL), LDN-193189 (100 nM), SB431542 (10 µM).

^t NMM = Neurobasal 1 (50 %), DMEM/F12 (50 %), B-27 (w/o Vit A), N2, Glutamax (2 mM), PS (1 %), ascorbic acid (80 µM), dib-CAMP (50 µM), BDNF (20 ng/mL), GDNF (10 ng/mL); media change every 3 days.

^u AST = DMEM F12, FBS (10 %), glutamine (2 %), P/S (1 %); NSC medium = DMEM F12, B-27 (2 %), glutamine (1 %), P/S (1 %), EGF (10 ng/mL), heparin (20 µg/mL), bFGF (10 µg/mL), heparin (20 µg/mL), NSC medium – (EGF, bFGF), RA (10 µM; D10).

^v Mitochondrial membrane potential.

^w Media + puro (100 ng/mL), FGF8 (100 ng/mL), BMP9 (10 ng/mL), NGF (100 ng/mL).

^x BrainPhys™, NGF (100 ng/mL), BDNF (5 ng/mL).

^y BrainPhys™, NGF (100 ng/mL), BDNF (5 ng/mL), P/S (0.5 %).

^z DMEM (89 % v/v), FBS (10 % v/v), P/S (1 % v/v) and nerve growth factor (50 ng/mL).

¹ Mitochondrial membrane potential.

markers with functional neurons (calcium imaging) compared to 2D systems. In 2017, Gu *et al.* 3D bioprinted hiPSCs for the first time [99]. The hiPSCs were maintained and renewed within the 3D bioprinted constructs and could be directed to form embryoid bodies (EBs) by using media without basic fibroblast growth factor (bFGF). EB formation of three germ layers was confirmed through morphological assessment and reverse-transcriptase quantitative polymerase chain reaction (RT-qPCR); the cells expressed markers of the endoderm (H19, PDX1), mesoderm (HAND1, IGF2) and ectoderm (Nestin, TUBB-3) and down-regulated pluripotent markers 15 days post-printing. They were able to demonstrate that pluripotency can be maintained, but differentiation can be directed to neuronal fate using neural induction media for 2–3 weeks after printing, then switching to a medium with BDNF to mature the neurons. The cells expressed neural progenitor markers PAX6 and Nestin 20 days post-printing, and expression of MAP2, βIII tubulin, GFAP, GABA, and presynaptic vesicle glycoprotein synaptophysin after 40 days. In 2018, Gu *et al.* combined their previous work, printing with frontal cortical hNSCs on a 3D-Bioplotter® using an agarose, alginate, and CMC-based bioink broadly described for neural tissue engineering detailed in a protocol paper [100]. They characterized cell viability, immunophenotyping using various antibodies (GFAP, SOX2, vimentin, OLIGO2, MKI67, TUJ1, Nestin, synaptophysin, GABA, and GAD) and live calcium imaging (Fuo-4, bicuculline) using confocal microscopy. The constructs were incubated for 10 days and differentiated from hNSCs to neurons/neuroglia using the differentiation media as before and culturing for at least two weeks. Viability was assessed on days 1 and 7 after printing; immunophenotyping is suggested at 3 weeks post-printing for undifferentiated constructs and at 24 days post-printing for differentiated constructs (2 weeks after differentiation started). They only showed staining for SOX2, Nestin, OLIGO2 and TUJ1, and spontaneous intracellular calcium release was observed.

Fantini *et al.* individually 3D bioprinted two different cell types (hiPSCs and hiPSC-derived NSCs) in alginate and gelatin-based bioinks crosslinked with calcium chloride (CaCl₂) [101]. Their optimal printing conditions were found to be 6 % alginate, and 4 % gelatin printed at 25 °C. Encapsulation with the neuroblastoma cells (SH-SY5Y) showed viability of ~ 50 % after 5 days of culture. Bioprinted cells of hiPSCs and NPCs showed better viability, (hiPSCs D0 = 100 %, D7 > 100 %; NSCs: D0 = 100 %, D3 = ~175 %, D7 = ~140 %), although viability was normalized to day 0, making it difficult to compare these directly to other models. No other characterization was done for the 3D bioprinted materials.

Abelseth *et al.* published a protocol detailing how an Aspect RX1 printer with novel lab-on-a-chip microfluidic printhead (DUO-1) could be used to print hiPSC neural aggregates (NAs) that remained viable within the construct up to 36 days [102]. Their bioink consisted of fibrin, genipin, and alginate, which was crosslinked with chitosan, CaCl₂ and thrombin. The culture medium included neural induction medium, and to direct motor neuron differentiation, the media was switched (day 17) to neural basal media with purmorphamine (puro) and retinoic acid (RA). They conducted viability assessments on day 10 (5 days after printing) and day 15 and found the viability to be 94.72 ± 3.48 % and 64.12 ± 21.27 %, respectively. The low viability was attributed to cells within the construct not being counted and the potential for the aggregates benefiting cells within the centre and limiting resources to the external cells. Flow cytometry was used to confirm this, where after 6 days the cell viability showed similar viability to live/dead imaging (91.65 ± 6.85 %). By day 30, the cells showed visible changes in their morphology, exhibiting extensions; immunocytochemistry (ICC) was performed to visualize neurite extension and confirm neuron phenotypes. On day 41, cells stained positive for TUJ1 (early neuronal marker) and showed no astrocyte phenotypes (GFAP–), which was thought to occur from low-stress printing promoting neuronal differentiation. However, quantitative viability assessments were not investigated past day 15. Using the same bioink, Sharma *et al.* investigated the use of guggulsterone-releasing microspheres (MSs) to differentiate hiPSC-

derived NPCs into dopaminergic (DA) neurons to generate neural tissues [103]. Cell viability and neuronal marker expression were used to compare the guggulsterone-MSs in the bioink to guggulsterone in the media and unloaded MSs. For NPC differentiation, constructs were added to plates consisting of NPC media (10 days), neural induction media (10 days), and Brain Phys Neuronal Medium (Day 20 post-printing). The cells and MSs were evenly distributed in the bioprinted constructs, with good viability. After one day post-printing, no significant differences were found between printed constructs with guggulsterone-MSs ('GM', $92 \pm 3\%$), blank microspheres ('UM', $78 \pm 11\%$), or guggulsterone in the media ('SG', $89 \pm 2\%$). The same was true after seven days, although GM had higher viability ($98 \pm 1\%$). The constructs were positive for FOXA2+ (midbrain-type dopamine neuron marker) and β -tubulin III (TUJ1+, an early neuronal marker) after 15 days, although TUJ1 was much lower in GM. After 30 days, constructs were positive for TUJ1+ and TH+ (tyrosine hydroxylase; dopaminergic neuron marker) both for cells that migrated out of and stayed within the construct. Flow cytometry indicated that TUJ1 ($15 \pm 1\%$), TH ($8 \pm 1\%$), and GFAP ($15 \pm 4\%$) were higher in GM condition, suggesting that the guggulsterone MSs promote neuronal differentiation, although both astrocyte and neural markers were proportionally expressed. O4 expression was similar between GM and UM, suggesting that the microspheres may play a role in oligodendrocyte differentiation. The cells were shown to differentiate into neurons due to the upregulation of TH, NR4A1 and LMX1B (roles in dopaminergic neurons), and FOXA2, which was expressed in all conditions, suggesting the media was beneficial for DA neuron differentiation.

Restan Perez *et al.* continued the use of this bioink to fabricate the first neural model using MSCs [104]. The MSCs were differentiated to DA neurons using small molecules puro, LDN193189 (LDN) and SB431542 (SB) and characterized their constructs over 12 days for viability, differentiation, dopamine release (in the supernatant) and electrophysiological activity. No media changes were performed between days 0 and 9 to allow for growth factor production to influence dopaminergic neuron generation. Their microscopy images showed even distribution in the constructs and noted that the control group had more cell death ($53.4 \pm 1.6\%$) compared to the differentiated group ($93.5 \pm 0.7\%$) on after 7 days. This low viability was possibly due to a lack of media changes, but the viability of the differentiating group (both 3D printed and non) had high viability (>93%) up to 12 days. The viability was higher than shown previously in Abelseth *et al.* 100 using the same bioink and bioprinter to print NPCs (Day 15 = $64.12 \pm 21.27\%$) [102]. The 3D bioprinted models could successfully differentiate (TUJ1+ = ~87%, TH+ = ~76%); however, no neurite extension was seen in 3D models but were present in 2D controls (~87% of the TUJ1+ cells had neurite extensions), and the 2D conditions had higher relative TUJ1 and TH (~98% both). Notably, the 3D bioprinted models did show enhanced dopamine release (5.47 ± 0.18 pg/mL), where no dopamine was released in 2D or 3D control groups, in addition to enhanced electrical activity after excitation with potassium chloride (KCl). Similar work was detailed in a protocol paper which outlined the use of a fibrin-based bioink for 3D bioprinting MSCs and differentiating them into DA neurons [105]. This protocol paper outlines the preparation of MSCs, including plate coating with poly-L-ornithine (PLO) and laminin to enhance cell attachment, and the formulation of low viscosity (TissuePrint-LV) and high viscosity (TissuePrint-HV) bioinks. The bioprinting process is described for two different bioprinters (RX1 & BIOX), followed by instructions for culturing the 3D constructs and inducing MSC differentiation using growth factors, and includes analysis techniques such as cell viability assays, ICC, electrophysiology, and dopamine Enzyme Linked Immunosorbent Assay (ELISA). Chrenek *et al.* also reported a workflow for 3D bioprinting with the Axolotl TissuePrint-HV kit both with and without a support bath, as well as an alginate and gelatin-based crosslinker [106]. While no results were shown, it was indicated that cell viability is sustained at high levels and constructs remain stable up to 6 weeks of incubation.

Further work with this bioink was used to model Alzheimer's disease (AD) by integrating puro-releasing MSs into the bioink using the RX1 bioprinter [107]. This work bioprinted AD patient-derived NPCs into dome-shaped constructs mimicking the *in vivo* environment. The inclusion of MSs, encapsulated with differentiation-inducing compounds, supported the development of cholinergic neurons resembling basal forebrain cholinergic neurons (BFCNs). The bioprinted models were assessed for cell viability, marker expression, and electrical activity, demonstrating successful differentiation and the presence of immature electrical responses. The fibrin-based bioink, coupled with a microfluidic extrusion printhead system, further enhanced cellular viability and functionality. The study highlighted that the bioprinted tissue models not only exhibited expression of key AD markers (amyloid-beta - A β , tau protein) and neuronal characteristics (TUJ1+, FOXG1+, ChAT+) but also showed potential for use in drug screening and personalized medicine applications. The microspheres played a crucial role in improving the mechanical properties and longevity of the constructs, underscoring their value in AD research and treatment development.

Y. Li *et al.* designed a 'co-cultured' neural tissue model using photo-crosslinkable bioink (containing neurospheroids) printed into a low Young's modulus gelatin support bath (containing astrocytes) [108]. The elasticity of the support bath was designed to mimic the natural stiffness of non-neural regions of the brain, favouring astrocyte growth and self-assembled neural-astrocyte construction. In addition, the support bath enabled physical crosslinking of the alginate during printing with divalent cations and enhanced shear thinning (and ensured homogenous embedding), followed by UV crosslinking for mechanical stability. The optimized bioink contained GelMA, gelatin, alginate, and laminin within a media-based solution. The goal was to promote neural differentiation, where RA was added to the media after 4 days. It was found that fetal bovine serum (FBS)-containing culture promoted the formation of neuroglia cells. The neural cells extended along the bio-printed fibres after 7 days of co-culture and by 14 days, elongated morphologies were observed (F-actin+, TUJ1+). Importantly, the interconnected networks were observed where neural extension beyond the printed niche was present (TUJ1+). After 2 weeks, astrocytes (GFAP+) formed large networks, which was attributed to construct degeneration leading to unincumbered cell proliferation. Morphological differences were observed at the niches, where astrocytes had more rounded morphology, and invading neurons also had circular morphology (but TUJ1+), likely due to the higher stiffness within the bath.

Kajtez *et al.* used embedded bioprinting, where a soft gel is extruded into a stiff (yield-stress) support medium with high fidelity, using similar principles of sacrificial printing (Fig. 6) [65]. The discussed Self-Healing Annealable Particle-ECM (SHAPE) composites for the printing bath generate pseudoplastic materials that are capable of smooth sol-gel transitions, integrating hydrogel-based polymers, and long-term support. The SHAPE support material has a ~70% granular volume in a ~30% hydrogel/volume composed of common ECM molecules collagen, laminin, hyaluronic acid (HA) and fibronectin. Importantly, this method can be tailored for various mechanical stiffnesses to match other tissue regimes or crosslinking techniques. After 2 months of differentiation, axonal extension and neurite outgrowth from the proliferating hNSCs were observed. Significantly, differentiating neurons had interregional organization along the path and extending axonal bodies, which is a function of native brain tissue and function, and these morphologies were highly preserved in the SHAPE hydrogels during fixation. After 4 weeks, the hNSCs were TUJ1+ and TH+, and RT-qPCR showed down-regulated expression of progenitor markers (BRN2, SOX1, SOX2), increased neuronal expression (MAP2, NCAM, SYN), and midbrain/dopaminergic fate (NURR1, AADC, DAT, TH) (Fig. 6G). In a co-printed geometry of a core (containing ventral mesencephalic hNSCs) and outer ring (with hNSCs from a forebrain region that typically differentiates to astrocytes), showed after 4 weeks TUJ1+ core and highly

expressed GFAP+ outer ring (Fig. 6J). Gelatin was printed within the SHAPE composites and upon sacrificial removal, simultaneous flow through the channels was demonstrated which could be useful for flow dynamics during vascularization. Ultimately, they found that oxygenation could be controlled by infill density and extrusion to generate relevant brain levels (1–3.5 % dissolved O₂).

The influence of gold nanoparticles (AuNPs) in a simplistic AD model was investigated by Chiang *et al.* using a CELLINK bioink to 3D bioprint hNSCs [109]. The protective effects of AuNPs on A_β inflammation and oxidative stress were investigated by assessing inflammatory cytokine expression and cell viability. While the target was AD, the phenotype was not naturally produced *in vitro* using AD-derived cells, rather they used their neural model for a proof-of-concept of the effect of AuNPs following A_β exposure (A_β1-42 treated for 24 h). They found that in the presence of A_β, the AuNPs enhanced the viability of hNSCs, reduced tumour necrosis factor-alpha (TNF-α) and Interleukin-1 beta (IL-1_β) expression (which are inflammatory cytokines) and increased inhibitory kappa B kinase (IKK) expression. Their control models (no A_β treatment or AuNPs) models expressed SOX2 and Nuclear factor erythroid 2-

related factor 2 (Nrf2). This study emphasizes the potential of treatment investigations with functional neural models, however, without functional analysis of the bioprinted model, caution must be used in interpreting these findings. When investigating infection with either severe acute respiratory syndrome coronavirus 2 SARS-CoV-2 or mouse-adapted versions (MA-SARS-CoV-2), de Melo *et al.* conducted some functional assessments for their disease model [110]. The bioink combined gelatin and GelMA with or without laminin to 3D bioprint murine cortical astrocytes and seeded surface layer of mature murine neurons. Initially, they compared bioink formulations with and without laminin, where ultimately laminin-included bioinks favoured softer materials with increased porosity and enhanced viability over 2 weeks. In addition, the laminin-containing bioink had higher cell adhesion and more elongated astrocyte morphologies, suggesting higher matrix recognition and anchorage and that laminin is necessary for the native tissue-like behaviour of astrocytes. The models were used in combination with seeded neurons (since they had low viability with ultraviolet (UV) exposure and various printing speeds), which were infected with MA-SARS-CoV-2 to adapt to species differences in susceptibility. In this

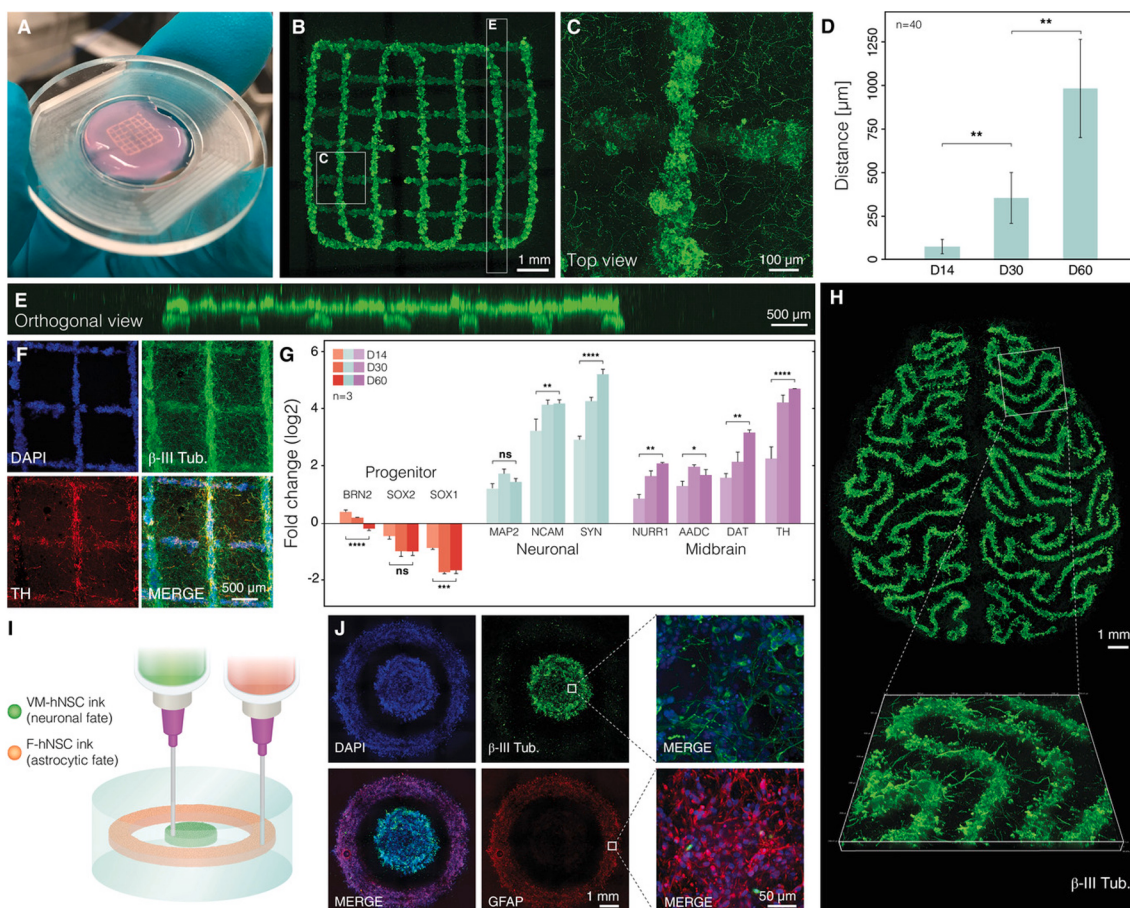


Fig. 6. Reproduced from Reference [65] with permissions from © Kajtez J. *et al.* 2022. Creative Commons Attribution License. Original caption: Generation of authentic human neurons within 3D printed constructs. A) Photograph of a 3D printed construct in annealed SHAPE support after 2 months of differentiation. B) Confocal image of the same construct labeled with Calcein-AM. C) Maximum intensity projection of a 200 μm optical section showing that neural projections extend in the volume between printed lines. D) Quantification of the extent of projection outgrowth away from a 3D printed structure as a function of the differentiation time. E) Orthogonal projection showing that the structural integrity with defined features in different layers are preserved. F) Fluorescence images of immunostained 3D printed construct after 2 months of differentiation displaying neuronal and dopaminergic markers (β-III tubulin and TH respectively). G) RT-qPCR gene expression analysis of the printed construct at 3 different time points indicating midbrain patterning and neuronal maturation. Nondifferentiated hNSCs were used as a reference. H) Maximum projection fluorescence image of neurons in a 3D printed construct resembling brain meanders with a 3D close-up view of a selected segment. I) Illustration showing the printing of cells with orthogonal differentiation trajectories by using 2 inks containing hNSCs with different predefined fates. Inks were printed in consecutive order in concentric circle design within the same SHAPE support. The outer radius of the inner and outer disk is 2 and 4 mm, respectively. J) Fluorescence images of fixed and immunolabeled constructs after 1 month of differentiation. DNA counterstain shows the presence of cells both in the inner and outer ring but staining for GFAP and β-III tubulin reveal distinct protein expression characteristics between cells generated from each ink. Cells display elongated morphology indicating successful differentiation.

model, there was an increased expression of spike protein ($15.9 \pm 2.6\%$ of cells were infected), and after 7 days, neuronal phenotypes (β -tubulin III+) and astrocytes (GFAP+) were connected.

Work by Abdelrahman *et al.* used two self-assembling amino acid (AAs) sequences (Ac-Ile-Val-Cha-Lys-NH₂ = IVZK; Ac-Ile-Val-Phe-Lys-NH₂ = IVFK) as their bioink to bioprint ventral midbrain (VM) DA and non-DA neurons [11]. Initial work performed encapsulation studies to characterize viability, ICC, morphology, and extracellular spontaneous neuronal activity. The compound 6-hydroxydopamine (6-ODHA) hydrochloride was used to simulate DA-loss expressed in Parkinson's Disease. Most characterization was done in scaffolded (not bioprinted) scenarios. In the scaffolds, they found that viability increased, adenosine triphosphate (ATP)-related signals increased, and encapsulation in IVFK showed cell attachment, migration and neurite extension after 3 days. The number of neurites, number of branches, neurites length, and dominant neurite length in both TUJ1+ and TH+ cells were also quantified. Successful neuron migration out of the neurospheroids encapsulated was observed by day 3 and microelectrode arrays (MEAs) showed that the peptides enhanced spontaneous electrical activity until day 34 (IVFK) and 42 days (IVZK). The 3D bioprinted models were only assessed until 3 days after printing, and the AAs were printed in an elastic mould to allow for shape retention during the crosslinking process. After 3 days post-printing, the VM neurons expressed TUJ1+ and TH+ (TUJ1 was more pronounced), and the cells were viable, although no quantification was given.

Scarian *et al.* used a CELLINK bioink (IK-102000; composed of cellulose nanofibrils and alginate) to bioprint hiPSC-derived NSCs from a patient suffering from sporadic Amyotrophic lateral sclerosis (sALS) and differentiate these in the constructs to motor neurons [111]. Cell viability continually increased over the differentiation period, but was low after printing, rising from approximately 40 % on day 0 to ~60 % after 20 days. The cells were positive for typical differentiation markers at various stages: NSCs (Nestin, SOX2, SOX1, PAX6), motor neuron progenitors (MNP; Olig2, PAX6) and motor neurons (MN; TUBB3, ChAT). It is unclear on what days these were expressed, but it is assumed to be similar to the viability timeline (NSCs = D0-7; MNPs = D7-20; MNs = D20). This differentiation was confirmed quantitatively using RT-qPCR. It was suggested that the sALS leads to decreased differentiation, since sALS NSCs had higher levels of Nestin and SOX2 (typically earlier progenitor markers), whereas the controls had typically more mature markers (higher SOX1 and PAX6). Electrophysiological analysis showed that the neurons responded to KCl induction, and displayed electrical activity when untreated, which was attributed to auto-fluorescence of bioink causing background fluorescence.

Matthiesen *et al.* investigated 3D bioprinting with human primary fetal astrocytes (FPA) in a bioink made of modified HA and an 8-arm polyethylene glycol (PEG) with terminal azide groups, (PEG-Az)₈ which forms hydrogels via click chemistry [112]. The HA was modified with bicyclo[6.1.0]nonyne (HA-BCN) to functionalize with ECM derivatives cyclic RGD (cRGD) and IKVAV (Ile-Lys-Val-Ala-Val). 3D bioprinting was individually assessed with human SH-SY5Y, U87 glioblastoma (GBM) and human FPAs. SH-SY5Y cells were used to assess biocompatibility over 6 days. While the metabolic activity (indicated by % reduction of AB) was shown to decrease significantly in all groups in the first 6 days, ICC staining showed clustering of cells and increased cell numbers over the same period, suggesting that the systems support cell proliferation. All hydrogels showed similar viability on day 1 for FPA cells and increased viability over 6 days. For 3D bioprinting, the FPA cells were printed in either i) HA-BCN:(PEG-Az)₈, ii) HA-BCN:(PEG-Az)₈ with cRGD, or iii) HA-BCN:(PEG-Az)₈ with IKVAV. The only analysis for the 3D bioprinted cells was staining with phalloidin for F-actin after 4 days and investigating morphology and number. Interestingly, the material, while soft, could be printed with high fidelity; no apparent differences (qualitative) were seen for cell viability between modifications (none, cRGD, or IKVAV) similar to the 2D conditions. Morphologically speaking, no peptide modifications generated rounded cells whereas

peptide modifications lead to dendritic morphologies and enhanced cellular interaction. Cells printed in the RGD-modified hydrogel all led to a significant number of extensions although this was not quantified. They did observe condensed morphology compared to the 2D systems indicative of stress-strain effects of printing.

Z. Wang *et al.* fabricated a 3D nerve cell model with brain-like mechanical properties and tuneable vascular structures using a grid geometry [113]. Using a 3D coaxial printing approach, the vascular structures were created with an outer PEG-diacrylate (PEGDA)/Pluronic F127 hydrogel layer and an inner Pluronic F127 layer, where porosity could be adjusted through the sacrificial Pluronic F127. The nerve cells, encapsulated in a gelatin-based hydrogel (GelMA), showed better proliferation in matrices with lower compressive moduli (2–7 kPa). The vascular structures enhanced nutrient exchange and cell viability, making this 3D nerve cell model a promising tool for studying ischemic stroke and neurodegenerative diseases. The 3D bioprinted model attempts to resolve the 3D model contradiction, requiring both high modulus for stability and low modulus for nerve stimuli, by creating a low-modulus, brain-like (2.3 ± 0.6 kPa compression modulus) 3D nerve cell model with adjustable porosity.

Rueda-Gensini *et al.* developed a 3D neuroimmune co-culture system to model Parkinson's disease (PD) microenvironments using a biomimetic hydrogel bioink, methacryloyl-modified decellularized small intestinal submucosa (SISMA) with electroconductive graphene oxide nanoflakes (SISMA-GO) [10]. This bioink facilitated the bioprinting of dense networks of mature human dopaminergic neurons, with enhanced functionality and differentiation compared to 2D cultures. The system also integrated neuroimmune interactions by co-culturing neurons with astrocytes, macrophages, and dendritic cells. The model replicated key PD pathologies, including α -synuclein aggregation, mitochondrial dysfunction, and oxidative stress, demonstrating increased resilience and enabling extended study of PD progression upon exposure to the neurotoxin A53T α -synuclein. Key functions include generating mature dopaminergic neuron networks with enhanced activity and connectivity, incorporating neuroimmune interactions with astrocytes and monocytes, and recapitulating PD pathologies such as α -synuclein aggregation, mitochondrial dysfunction, and oxidative stress. The model offers a more comprehensive tool for studying PD compared to traditional methods.

Recent research by Yan *et al.* was not originally identified in our systematic search, even though it has clear relevance to the topic at hand [14]. Here, 3D bioprinted models investigated cell types within similar tissues (excitatory neurons, inhibitory neurons and astrocytes), between tissues (cortical and striatal) and for disease modeling of Alexander disease (using a tri-culture). Their models were printed as horizontal patterning between cell types to circumvent the limited oxygen diffusion in avascular models, but was also necessary since the soft bioinks relevant to neural tissues could not be achieved with vertical layered geometries. A cerebral cortex model was formulated with GABAergic interneurons (derived from medial ganglionic eminence (MGE) cells) and glutamatergic neurons (derived from cortical progenitors) printed at a ratio of 1:4, respectively. After 60 days post-printing, cortical transcription factors (TBR1, CTIP2, SATB2) and GABAergic subtypes were observed (calretinin – CR, calbindin – CB, parvalbumin – PV, and somatostatin – SST) (Fig. 4A). Co-culturing the two neural types led to a relatively increased presynaptic marker (SYN1), suggesting that these cellular interactions promote synaptogenesis. The formation of inhibitory and excitatory synapses was identified by presynaptic (vGAT, vGlut1) and postsynaptic (gephyrin) markers within 45 days (Fig. 4A). The models were also shown to have functional Na⁺ and K⁺ currents, evoked and spontaneous action potentials (eAPs, sAPs, respectively) 3 weeks after printing. Tri-culture with this system and astrocyte progenitors identified matured neurons (NeuN+) 30 days post-printing, with extensive branching and close neuron-astrocyte interactions (Fig. 5A). Functional properties were analyzed through whole-cell patch clamping, revealing excitatory and inhibitory synaptic connections,

while live-cell imaging using calcium and glutamate indicators explored neuron-astrocyte interactions. Notably, the tissues showed functional properties (KCl response) and expression of the functional marker glutamate transporter 1 (GLT-1) after 40 days post-printing, which was corroborated by identified functional glutamate uptake by astrocytes (iGluSnFR signals). Cortical neurons and striatal neurons were co-printed to model interactions between tissues; axonal staining with SMI312 showed that cortical neurons project axons towards the striatum, similar to native tissues (Fig. 5B). This model enables the formation of functional neural circuits, integrates astrocytes for neuron-astrocyte interaction assessment, and allows bioprinting of layered tissues with defined compositions. The tri-culture (glutamate and GABA neurons with astrocytes with the Alexander disease mutation, or its isogenic control) was able to replicate the disease-relevant phenotypes of Alexander disease, including intracellular astrocyte aggregation, lower GLT-1 (20 days post-printing), reduced synaptic puncta density, and lessened Ca^{2+} response. The platform serves as a valuable tool for modeling neural network activity under both physiological and pathological conditions.

The most recent paper included in the review was work by L. Wang *et al.*, who designed a biomimetic six-layer 3D brain tissue model resembling the natural brain cortex [115]. This model was bioprinted using an integrated 3D printing platform that combined direct ink writing (DIW) and electrohydrodynamic (EHD) fibre printing to fabricate 6-layer *trans*-sectional patterning of PC12 and GL261 cells in a GelMA and fibrinogen-based bioink. Their optimal bioink consisted of 5 % GelMA and 0.5 % fibrinogen, which had modulus values less than 4 kPa. The research investigated how structural parameters of fibres, such as diameter and spacing, influence cell behaviour. It was found that smaller diameter fibres (10 μm) and closer spacing (150 μm) guided neurite orientation and cell migration, highlighting the importance of fibre structures in directing neural network formation and connectivity. Here, they examined the effects of structural features on neural cell directionality and neuron-glia interactions and found that smaller-diameter fibers better guide neurite growth. In addition, they discuss the role that topographical cues play in neurite extension and function, highlighting the importance of geometrical features within tissue constructs. This study was a proof of concept for the 3D bioprinted architecture, and the authors suggest the integration of hiPSC-derived cells to fully assess the potential for neural tissue modeling. They also mention that the 6 layers were difficult to assess for ICC, and found 5-layer constructions were suitable for immunohistology.

3.1.2. Spinal cord

Of the systematically reviewed papers, Joung *et al.* were the first to co-culture cells, using Matrigel-based bioink to co-print neural progenitor and oligodendrocyte progenitors to precisely pattern a cell-laden scaffold with point-dispersion printing for applications such as the treatment of spinal cord injuries [118] (Table 3). Their work generated intricate scaffolds with 200 μm spaced channels for axonal guidance, generating similar cytoarchitecture patterning of spinal cord tissue. The spinal NPCs decreased in viability from ~ 75–80 % to ~ 20 % after 4 days compared to fibroblasts (>90 %); this can be attributed to the sensitivity of neural cells compared to other cell types. They were able to show the maturation of their model when co-cultured after 7 days where OPCs expressed mCherry and NPCs expressed β III-tubulin (also shown to be NeuN+ by day 7 when printed alone), and functional neurons through calcium imaging 14 days after printing.

In 2018, de la Vega *et al.* bioprinted NPCs derived from hiPSCs in a fibrinogen, chitosan, and alginate-based bioink over 30 days to generate spinal cord models using a microfluidic-based printhead with the Aspect RX1 bioprinter [119]. The NPCs were differentiated to motor neurons using various combinations of small molecules CHIR99021 (CHIR), SB, LDN, puro and RA. The differentiation media did not affect cell viability, where all were ~ 90 % after 7 days. After 15 days, almost all media conditions had higher levels of Olig2 and HB9 than β T-III. As expected,

the combination of small molecules was thought to play a role in differentiation, where different combinations produced different significance – e.g., for Olig2, expression was drastically reduced when Puro and RA were combined with other small molecules, but this same condition enhanced β T-III and HB9 expression. The use of RA was shown to preferentially express Olig2 and HB9, but had lower β T-III expression, similar to media without added factors (PR-). The addition of Puro also enhanced spheroid formation, with highly concentrated β T-III by day 30. After 30 days, all conditions expressed β T-III, but all combined small molecules (PR+) showed enhanced β T-III and ChAT expression, and low GFAP, suggesting a better environment for motor neuron differentiation.

Han *et al.* used gelatin-based bioinks to demonstrate that both boundary cap neural crest stem cells and mixtures of astrocytes and motor neuron precursors could be viably bioprinted over several weeks [120]. They first tested optimal concentrations of micro-transglutaminase (mTG) concentrations and gelatin and found that 12 % gelatin and 25 mg/mL mTG mixture provided optimal gelation properties and cell viability based on relative cell count and morphology. Interestingly, they determined differentiation by determining the proportion of elongated cells. They also tested different layers of printed (1, 3, and 5), and found that 1 layer had little fluorescence and lost viability, and 3 layers showed increased fluorescence after 1 day compared to 5 layers but did not change after 3 days, and by day 3, the 5-layer had higher fluorescence. These phenomena were reasoned to be caused by delayed media diffusion in 5 layers, where longer incubation led to increased dispersion. The boundary cap neural crest stem cells contain fluorescent proteins, which enabled live imaging for up to 5 weeks. The cells were evenly distributed and immunofluorescent analysis of sectioned constructs (immunohistochemistry, IHC) showed TUJ1+ (referred to as bTUB in the text) and GFAP+ cells, but exterior cells had advanced morphologies. When 3D bioprinting was done with iPSC-derived MN progenitors and astrocytes mixed, both GFAP+ and bTUB+ were seen throughout, with surface cell clusters with extensions. They found that neural differentiation depended on the density and location of printed cells since the interior had immature morphologies, but surface cells obtained dendritic processes suggesting differentiation.

Most recently, Song *et al.* developed a conductive composite hydrogel (CCH) scaffold for delivering NSCs to treat spinal cord injuries (SCI) [121]. The CCH scaffold, synthesized using a novel conductive polymer of 3,4-ethylenedioxythiophene (EDOT) monomers, chondroitin sulfate methacrylate (CSMA) and tannic acid (TA) (PEDOT:CSMA,TA) integrated into a GelMA/PEG matrix, was 3D bioprinted to transport NSCs and repair spinal cord damage. *In vivo* experiments on SCI rats showed that the scaffold inhibited astrocytic differentiation, promoted neurogenesis, and facilitated the development of organized nerve fibres while reducing glial scar tissue, leading to significant recovery in locomotor function. The study highlights the scaffold's potential for stem cell-based SCI therapy, offering a promising approach for future clinical applications in regenerative medicine. Importantly, the drawbacks of hydrogels in nerve regeneration were discussed, and, while the systematic search focus on brain neural models, may explain the lack of spinal models in our search.

3.1.3. Tumour models

While not specifically including neural cells for the purpose of modeling neurons and supporting cells, tumour models, including glioblastoma and neuroblastoma cancer models are worth discussing. These models have been developed and used for patient-specific treatments and drug screening. A significant number of papers conducted 3D bioprinting for modeling glioblastoma (GBM) (Table 4), which is the most prevalent CNS tumour with high fatality [122]. Not unlike other complex diseases such as Alzheimer's disease, the mechanisms involved of tumour angiogenesis, a feature prominent in GBM, is complex and would benefit greatly from representative functional models [122]. The common theme of disease models is to enhance the understanding of

Table 3

Summary of the included articles that were designed for modeling the spinal cord.

Source	Printed Bioink Composition		Cells	Construct Media	Bioprinter	Characterization	
	Bioink	Crosslinker				Bioink	Cells/Construct
Joung et al. 2018 [118]	(1) Matrigel (50 % v/v), (2) Gelatin (7.5 % w/v), fibrinogen (10 mg/mL), HA (3 mg/mL), CaCl ₂ (2.5 x 10 ⁻³ M), (3) GelMa (7.5 % w/v), PI (LAP; 0.05 %), (4) 1:3 (w/v) alginate; methycellulose ^a (designed for scaffold)	(2) Thrombin (100 U/mL), transglutaminase (TG) (0.2 % w/v)	Primary human neonatal dermal fibroblasts	sNPCs: N2/B27 media, GDNF (20 ng/mL), BDNF (20 ng/mL), and NT3 (20 ng/mL); OPCs: N2/B27, FGF-2 (10 ⁷ cells/mL); hiPSC-derived ventral sNPCs (10 ⁷ cells/mL); miPSC-derived OPCs (10 ⁷ cells/mL)	Custom microextrusion 3D printer (100 μm ID; 1–3 mm/s; 0.5–1 psi (cell laden); customized heating (37 °C)/cooling (4 °C) system)	<i>Compression</i> (uniaxial, unconfined; Young's modulus)	<i>Viability</i> (Live/dead; 3 h, D1, 4) <i>ICC</i> (STE121, TUJ1, mCherry, NeuN, Sox10, eGFP; D1, 4, 7) <i>Calcium Imaging</i> (D14) <i>AG:MC</i> (Viability, D3; Morphology, D3)
de la Vega et al. 2018 [119]	Fibrinogen (20 mg/mL), alginate (0.5 % w/v), genipin (0.3 mg/mL)	CaCl ₂ (20 mg/mL), chitosan (0.075 % w/v), thrombin (1.7 U/mL)	hiPSC-derived NPCs	Various media: Negative (N+), Puro positive (P+), RA positive (R+), Puro and RA positive (PR+), Puro and RA negative (PR-) ^b	Aspect Biosystems RX1 with LOP™ printhead (20 mm/s; 20 mbar (bioink), 40 mbar (crosslinker), 100 mbar (buffer))	—	<i>Viability</i> (Guava ViaCount®, flow cytometry; D7) <i>Flow cytometry</i> (βT-III, Olig2, HB9; D15) <i>ICC</i> (TUJ1, ChAT, GFAP; D30) <i>Microscopy</i> (D0, 1, 7, 10)
Han et al. 2022 [120]	Gelatin (12 % w/v), Laminin (5, 10 μg/mL)	Micro TG (1:10 v/v, mTG:gelatin, 25 mg/mL)	Boundary cap neural stem cells (2.5 × 10 ⁶ cells/mL)	Proliferation medium Differentiation medium (D3)	CELLINK BIO X (3 mm syringe, 0.41 mm ID) 3 layers	<i>Rheology</i> (viscosity, temperature sweep)	<i>Viability</i> (AlamarBlue; D1, 3) <i>Immunohistochemistry</i> (GFAP, TUJ1, Hoechst; D7, D14, D21) <i>Live Imaging</i> (up to 5 weeks)
Song et al. 2023 [121]	PEDOT:CSMA, TA (0.1 % w/v), GelMA (5 % w/v), PEGDA (0.3 % w/v), PI (LAP, 0.3 % w/v)	UV crosslinking (405 nm)	Rat NSC spheroids (3x10 ⁶ cells/mL)	Proliferation medium (DMEM/F-12, L-glutamine, B27, P/S, EGF, bFGF) Differentiation medium (Complete DMEM/F-12, L-glutamine, B27, P/S)	Microextrusion-based 3D printer (GeSim, Bioscaffold 3.2; z-axially stacking structure; 5x5x3 mm)	<i>Rheology</i> (oscillating viscoelasticity tests, temperature-dependent gelation, viscosity) <i>FTIR</i> <i>Conductivity measurement</i> (electrochemical workstation) <i>Biodegradability</i>	<i>SEM</i> (D7) <i>Calcium imaging</i> (Fluo-4 AM; D7) <i>In vivo studies</i> (Female SD rats; behaviour assessment, Histological assessment) <i>ICC</i> (TUJ1, GFAP, MAP2, NF200, MBP, Olig2)

^a Printed with sNPCs or OPCs only.^b N+ = SB (2 μM), LDN (2 μM), CHIR (1 μM); P+ = Puro (0.1 μM), SB (2 μM), LDN (2 μM), CHIR (1 μM); R+ = RA (0.5 μM), SB (2 μM), LDN (2 μM), CHIR (1 μM); PR+ = Puro (0.1 μM), RA (0.5 μM), SB (2 μM), LDN (2 μM), CHIR (1 μM); PR- = Puro (0.1 μM), RA (0.5 μM).

disease function, progression, and treatment, and GBM is not immune to this need. Drug screening in this area would be of great benefit since uncontrolled vascular growth can lead to drug resistance [122]. However, traditional GBM models typically lack the characteristic tumour angiogenesis, are unable to replicate the complex tumour microenvironment, and fail to generate the hypoxic environments of *in vivo* tumours [122]. In the lab, most GBM models co-culture GBM cells and endothelial cells in the presence of vascular growth factors (VGFs), either cell-secreted or supplemented.

Using this same bioink and crosslinker composition and bioprinter as

Abelseth *et al.* [102], (except for a lower thrombin concentration of 1.7 U/mL), C. Lee *et al.* fabricated 3D bioprinted glioblastoma multiforme (GBM) models using U87MG human GBM cells [123]. The constructs were maintained in DMEM, FBS, and penicillin/streptomycin (P/S), or the same medium with the small molecules Forskolin, ISX9, CHIR99021, I-BET 151, and DAPT after 3 days. There was minimal cell clustering after printing, but the GBM cells tended to form spheroids in the constructs, which grew in density over time. The models were similar to tumour propagation *in vivo* conditions, where spheroids grew due to the proliferation of cells within the outer core of the spheres. Live/dead

imaging showed that the GBMs could be printed with high viability (~90%), which was relatively similar after 12 days. The GBM constructs were stained on day 12 using ICC for TUJ1 (early neuronal), and either CD133 (GBM stem cell marker), DCX (doublecortin – an early neuronal marker), or Nestin (neural stem cell and GBM marker). Printed cells showed very low TUJ1 but had higher expression of CD133 and Nestin compared to the 2D cultures, indicating cancer stem cell-like properties. The intensity was low for the ICC staining but could be due to the length of construct aging or autofluorescence of bioink mentioned elsewhere [104]. Using this same bioink, Smits *et al.* discussed the first use of 3D bioprinted models to evaluate model response to drugs/small molecules in our systematic review [124]. They used the RX1 bioprinter to co-print GBM cells with astrocytes, which was used as a GBM model to investigate a small anti-cancer drug, Compound 15. This compound is an antagonist to N-cadherin (NCAD), a commonly overexpressed molecule in tumours, especially in gliomas. Three conditions were investigated, a control, 10 µM of Compound 15, and dimethylsulfoxide (DMSO); cells were printed both individually and as a co-culture to investigate the effects of Compound 15. Most of the characterization was done on the influence of Compound 15 on viability and tumour size, to assess drug effectiveness. It was noted that there were differences in cellular staining between 2D and 3D bioprinted constructs, where 3D bioprinted models were more organized and rounded. Importantly, Compound 15 selectively acted on the GBM cells to decrease viability, whereas the astrocytes remained viable.

Tang *et al.* developed a co-cultured GBM model that contained three structures representing tumour-like regions, acellular ECM regions and an endothelial region (human umbilical vein endothelial cells, HUVECs) [125]. They used bioinks comprised of glycidyl methacrylate HA (GMHA) and GelMA to create four models (1): a tumour-only stiff model; (2): a tumour-only soft model; (3): a co-culture stiff model; and (4) a co-culture soft model. Their stiff models were 21 kPa, and soft were 2 kPa, which was designed to recapitulate *in vivo* differences in GBM patients, where higher stiffness is observed. They aimed to design varying stiffness levels to convey the intricacies and reciprocity of the ECM and cellular remodeling during GBM and address the lack of models that represent the complex, heterogenous, and dynamic tumour microenvironment of GBM using digital light processing (DLP) bioprinting. They adjusted the printing parameters and biomaterial concentrations to provide 3 stiffness levels. Each model had a 500 µm wide GBM area, surrounded by a ring-shaped ECM (500 µm), and co-cultures with endothelial cells printed on an external region of HUVECs. Compared to the soft models, the stiffer models had increased expression of genes related to hypoxia (CA IX, HIF1- α , SLC2A1), angiogenesis (VEGFA, SPP1), and apolipoproteins (APOL4, APOL6), among others. Soft gels also lead to more relaxed structures, and increased invasion of GBM cells. In the co-cultures, in both stiff and soft conditions, HUVECs migrated toward GBM cells, but in the stiff model, HUVECs (CD31+) both proliferated and sprouted blood-vessel like morphology adjacent to GBM cells (SOX2+). The stiff models also expressed higher angiogenic markers compared to soft, such as FN1, which is involved in the adhesion, growth, angiogenesis and reoccurrence of GBM. The models were shown to have biochemical and biophysical relevance to native GBM, which can be used to model various levels of GBM.

Neufeld *et al.* incorporated vasculature in their 3D bioprinted models to enhance the relevance of cancer models to achieve angiogenesis [126]. They used a tumour bioink (fibrinogen and gelatin) and a vascular bioink (Pluronic F127) to fabricate a GBM model. Their model included a printed bottom layer of fibrin/gelatin and cells (patient-derived GBM cells – PD-GB4, human astrocytes, and microglia) into a PDMS mold equipped with gaskets for connection to a peristaltic pump. A vascular geometry layer was printed on top using Pluronic F127 and thrombin, and then a final layer of the tumour bioink and cells was added, and sealed. For their vascular component, connection to a peristaltic pump allowed for fibronectin injection to create an adherent surface, followed by injection of labelled HUVECs and human

microvascular brain pericytes. Cells were cultured for 5 days in the media, followed by injection with dextran-FITC, and perfusion was created with unlabelled cancer and stromal cells (astrocytes and microglia). They found that their 3D GBM model recapitulated *in vivo* tumours compared to the 2D models, such as increased proliferation of both PD-GB4 and GL261 cells (GBM cells), and increased cell invasion in the presence of astrocytes. Further, using dextran, it was indicated that the cells within the “vessels” could circulate, leading to more intuitive drug screening scenarios. They looked at the effects of a P-selectin inhibitor (SELPi), which led to significantly decreased tumour growth after exposure. Further, the presence of GFAP (astrocytes) and IBA1 (microglia) were identified, which are highly active in GBM tumours.

X. Wang *et al.* Used coaxial 3D bioprinting to generate tube-like structures using an inner core of endothelial cells (HUVECs) surrounded by an outer shell of GBM cells (human glioma cells – U118) [122]. Their bioink was composed of alginate (mixed with U118-RFP cells in the core) and collagen (mixed with GFP-labelled HUVECs as a shell) which was printed into CaCl₂. They assessed cellular interaction over 9 days and confirmed the recruitment of endothelial cells by GBM cells was also exhibited in a mouse model. They found that in the co-culture, the amount of relative cell proliferation, and concentration of secreted VEGFA and bFGF were enhanced compared to individual cultures. After 5 days, the HUVECs extended into the U118 shell, and cellular fusion was observed by 9 days. Co-cultures also showed tubular structure and had higher levels of CD31 and VEGFR2 compared to HUVEC-only cultures. Vascular growth factors play a role in angiogenesis and this model comprised such factors; and the possibility that the tumour cells were secreting vascular growth factors together led to the enhanced tubular formation in the co-cultures (although ~ 9 were observed)

Sunil *et al.* used their 3D bioprinted brain model to investigate the potential of Bioengineered Immunomodulatory Organelle targeted Nanozymes (BIONs) in GBM [127]. They stated that their models could model the biology relevant between GBM cells and macrophages within their bioink to test the immune response of the BIONs. When exposed to BIONs and light, there was a drastic decrease in tumour volume and high cell death of the GBM spheroids. While most of their characterization methods relied on understanding the influence of BIONs on the host model, some techniques could be adapted to assess the functionality of neural tissue models. For example, the surface expression of calreticulin and high-mobility group box 1 (HMGB1) release from the GBMs was assessed. In this way, they wanted to see if the BIONs could trigger immunogenic cell death – an essential immune response. In the highest activated group (BIONs + light), there was a significant increase in HMGB1 release and calreticulin. They also analyzed mitochondrial membrane potential ($\Delta\psi_m$) to indicate apoptosis. This was done using a JC-1 assay and Annexin-V/FITC to indicate apoptosis. They used mitochondria, lysosome, endoplasmic reticulum, and golgi trackers. While these weren't used on the bioprinted models, incorporation into functional testing could be useful for other 3D bioprinted models.

While not explicitly a GBM model, Pei *et al.* 3D bioprinted layered constructs using gelatin and alginate, with collagen to regulate pore size and stiffness relevant to differing cortex layers [9]. Collagen was shown to directly influence porosity, allowing for complex mechanical patterning by tuning collagen concentration, although printing less than 30 layers was necessary to maintain the construct shape. A layered gradient was printed by alternating between various bioink compositions and cells (only U87 cells were indicated). The study largely focused on mimicking the porosity and moduli of gradient neural tissues. U87 cells were printed within the constructs and viability was tested after 7 days, which was shown to increase qualitatively. Viability was reported to be as high as 94.5 %, which is assumed to have been on day 7. The benefit of adding RGD peptide or bioactive factors (structural protein, glycoproteins etc.) was mentioned, but these were not investigated.

Yavuz *et al.* explored the neuroprotective effects of dopamine-loaded exosomes derived from Wharton jelly stem cells (WJ-MSCs) on the

Table 4

Summary of the included articles based on glioma, neuroblastoma, or glioblastoma models.

Source	Printed Bioink Composition		Cells	Construct Media	Bioprinter	Characterization	
	Bioink	Crosslinker				Bioink	Cells/Construct
C. Lee et al., 2019 [123]	Fibrin (20 mg/mL), alginate (5 mg/mL), genipin (0.3 mg/mL)	CaCl ₂ (20 mg/mL), chitosan (0.75 mg/mL), thrombin (1.7 U/mL)	Human GBM cells (U87MG; u/k concentration)	DMEM, FBS (10 %), P/S (1 %)	Aspect RX1 bioprinter	SEM (surface; D3)	ICC (TUJ1, CD133, DCX, Nestin, DAPI; D12) Viability (D0, 3, 6, 8, 12) SEM (surface; D3)
Smits et al., 2020 [124]	Alginate (0.5 % w/v), genipin (0.3 mg/mL), fibrinogen (20 mg/mL)	CaCl ₂ (20 mg/mL), chitosan (0.075 mg/mL), thrombin (1.7 U/mL)	Human GBM cells (U87MG; 1 × 10 ⁶ cells/mL) Human Astrocytes (1 × 10 ⁶ cells/mL)	GBMs: DMEM, FBS (10 %), AAS (1 %) Astrocytes: Astrocyte Medium (AM) + antagonist Co-culture: AM 3 conditions: control, Compound 15 (10 μM) and DMSO	Aspect Biosystems' RX1 with DUO Printhead (25 mm/s; 50 mbar (bioink), 60 mbar (crosslinker), 100 mbar (buffer))	—	Viability (Live/dead; D12 – GBM, D4 – astrocytes) ICC (NCAD, Actin, DAPI; D12)
Tang et al., 2021 [125]	Tumour Region = GelMA (10 % w/v) ^a , GMHA (2 % w/v) ^b Endothelial tumour region = Endothelial 25 s Region and Soft ECM = GelMA (5 % w/v), GMHA (1 % w/v) Stiff ECM = GelMA (10 % w/v), GMHA (1 % w/v)+	Light source Soft ECM = 20 s Endothelial/ tumour region = 10x10 ⁷ cells/mL Endothelial 25 s Region and Soft ECM = 30 s Stiff ECM = GelMA (10 % w/v), GMHA (1 % w/v)+	Human glioblastoma stem cells (TS576; CW468 cells) HUVECs (5x10 ⁷ cells/mL)	Maintenance medium = TS576 medium (50 %), EGM-2 (50 %)	Customized DLP-based 3D bioprinting system	Compressive Modulus (MicroSquisher; D1, 3, 7) SEM (surface) Molecular diffusion assessment	ICC (SOX2, GFAP, CD31, Ki67, Hoechst 33342; D3, 7, 14) RT-qPCR (ABCG2, CXCL12, GAPDH, MGMT, SPP1, VEGFA) RNA sequencing (tumour only) Drug Response (TMZ; D11)
Pei et al., 2021 [9]	Gelatin (6 % wt), sodium alginate (1 wt%), collagen (0.5, 1, 1.5 mg/mL) ^c	CaCl ₂ (0.1 %, 30 mins)	U87 cells (GBM) (1 × 10 ⁶ cells/mL)	—	Custom-built 3D extrusion printer (27 G, 15 mm/s, 60 μL/min for top and middle layer, 30 μL/min for bottom layer)	Viscosity (viscometer) Compression modulus (Universal testing machine) SEM (porosity) Printability	Viability (Live/dead; D1, 3, 7)
Neufeld et al., 2021 [126]	Fibrin bioink = Fibrinogen (1 % w/v), gelatin (6, 12 % w/v) Vascular bioink = Pluronic F127 (38 % w/v), thrombin (100 U/mL)	TG (3 % w/v), CaCl ₂ (250 mM), thrombin 0.5 U/mL; (min 3 h)	Patient derived-GB4 cells (Azurite-labelled; 1x10 ⁶ cells/mL) hAstro (GFP-labelled; 1x10 ⁶ cells/mL) hMG (1x10 ⁵ cells/mL) *printed together	1:1:1:1 ratio of DMEM, astrocyte medium, microglia medium, pericyte medium, and EGM-2	3D-Bioplotter (Envision TEC; 24–29 °C; vasculature = 0.25 mm needle, 6–8 layers)	Rheology (oscillatory time sweep) Mechanical (Young's modulus) Swelling (to D28) SEM (D14)	Swelling (to D28) Viability (PrestoBlue, up to 6–7 week) ICC (GFAP, IBA1, P-selectin, DAPI, Hoechst) SEM (D14)
X. Wang et al., 2021 [122]	Alginate (2 % w/v), collagen (1 mg/mL)	CaCl ₂ (3 %)	Human glioma cell line U118 (1x10 ⁶ cells/mL) Human umbilical vein endothelial cells (HUVECs; 1x10 ⁵ cells/mL)	DMEM, FBS (10 %)	Coaxial sheath /core nozzle Core: 0.577 mm, 5 mL/hr Shell: 1.469 mm, 15 mL/hr	Microscopy (inner and outer diamter)	Cell proliferation (Alamar blue; D1, 3, 5, 7, 9) VEGFA/bFGF Secretion (Sandwich enzyme immunoassay kit; D1, 3, 5, 7, 9) Morphology and Migration (Fluorescent labeled cells under confocal microscope, D1, 5, 9) qRT-PCR/Western Blot (VEGFR2, CD31; D1, 9) In vivo transplant: ICC (CD31, CD105, vWF, GFAP, 6 week) Microvessel Density (ICG)
Sunil et al., 2022 [127]	GelMA (2 % w/v), gelatin (4 % w/v), PI (LAP, 0.4 %), FBS (10 % v/v), P/S (1 % v/v)	UV Crosslinking (2 mins)	RAW 264.7 macrophages (3x10 ⁶ cells/mL) U87 GBM spheroids (2000 cells/mL)	DMEM medium	CELLINK BIO X 25 G needle	BIONs: Particle size analyzer (size distribution, polydispersity index, zeta potential) TEM (shape, surface morphology) Fluorescence	Viability (CellTiter-Glo 3D cell viability assay; D4 pp, 6hr + BIONs) Various BION characterization ^d

(continued on next page)

Table 4 (continued)

Source	Printed Bioink Composition		Cells	Construct Media	Bioprinter	Characterization	
	Bioink	Crosslinker				Bioink	Cells/Construct
Yavuz et al., 2023 [114]	Alginate:gelatin (3:5) (from HD Bioink)	CaCl ₂ (0.1 N)	SH-SY5Y spheroids (1x10 ⁷ cells in 5 mL)	DMEM-F12, 10% FBS, L-Glutamine, NEAA, Sodium pyruvate, Sodium bicarbonate	Bioprinter; 7.5 psi; 60% speed; 37°C; cell suspension seeded on top of construct (1x10 ⁶ cells/2 mL)	spectrophotometer UV-Vis Western blot Catalytic activity Polyacrylamide gel In vitro release study *FTIR/Trasmission Electron Microscopy (TEM) done previously	Viability (Live/dead) ICC (TUJ1, DAPI)

^a GelMA = GelMa (20 % w/v; 1 g gelatin:0.1 mL methacrylic anhydride).

^b GMHA (4 % w/v; 200 kDa HA, trimethylamine, glycidyl methacrylate).

^c Each concentration was optimal for printing gradient.

^d Reactive oxygen species (DCFH-DA; 6 hr); Mitochondrial membrane damage (JC-1 assay); Apoptosis (Annexin V-FITC/PI Apoptosis Detection kit); Immunogenic Cell Death Induction (HMGB1 release/calreticulin exposure); Cellular uptake of BIONs (ICC; DAPI; 3, 6 hr); Extracellular HMGB1 Release (Human HMGB1 Elisa Kit); Endocytic Pathway of BIONs (confocal microscopy); Intracellular trafficking of BIONs in U87 cells (LysoTracker Green, Mitotracker Green, kDa^{RhoB}dextran, ER Staining Kit Green, Golgi Staining Kit; 6 hr); Penetration of BIONs in 3D Spheroids (confocal microscopy; 6 hr).

dopaminergic neuroblastoma cell line SH-SY5Y [114]. To induce neurotoxicity, cells were exposed to 6-OHDA. The results indicated that the dopamine-loaded exosomes effectively mitigated neurotoxicity in both 2D and 3D cell cultures. Increased cell viability and enhanced expression of the neuronal marker β-tubulin were observed in the exosome-treated groups compared to controls, as confirmed by Live/Dead analysis and immunostaining. The study predicts that exosome-based carrier systems from WJ-MSCs have significant potential for treating neurodegenerative diseases due to their regenerative properties and size. This research outlines the potential of dopamine-loaded WJ-MSC exosomes as an effective nano-drug delivery system for neuroprotection and highlights their promise as a therapeutic platform for central nervous system disorders. Additionally, they emphasize exosomes' abilities to transfer genetic information, regulate immune response, and cross the blood-brain barrier, with 3D cultures as a promising alternative for *in vivo* research. Further studies on their *in vivo* efficacy were recommended. While the authors expressed that their model was used to represent Parkinson-like features, it was considered within the tumour model since neuroblastoma (SH-SY5Y) cells were used.

3.1.4. Other models

Beyond establishing brain, spinal cord, or tumour models exclusively, some studies discussed general applications for their respective bioprinted tissues. These applications are summarized next.

3.1.4.1. CNS. With a CNS model in mind, Tomaskovic-Crook & Crook established a protocol to bioprint hNSCs using agarose (1.5 %), CMC (5 %) and alginate (5 %) in the bioink [128] (Table 5). While only briefly mentioned in the protocol, electrically conductive bioink can be made using conductive polymer and electrodes to penetrate the construct to initiate differentiation. Following printing, the constructs were covered with 2 % CaCl₂ in PBS and crosslinked for 10 min, followed by washing with DMEM/F-12 (x3 washes), hNSC proliferation medium (10 min, x2; 1 h, x1) and then changed to full media, composed of Complete NeuroCult Proliferation Medium with NeuroCult NS-A Basal Medium, NeuroCult NS-A Proliferation Supplement, heparin, epidermal growth factor (EGF) and bFGF. They suggest having the hNSCs in a proliferation medium (without heparin, EGF and bFGF) for at least 4 days, and differentiation to functional neurons and supporting neuroglia can be done by switching to hNSC differentiation medium. In the protocol, it is suggested to assess viability on days 1 and 7 with calcein and propidium iodide. For membrane permeant live neural labelling, they used NeuFluor NeuO diluted in hNSC differentiation medium added directly to

the constructs and visualized using a fluorescent microscope. This labelling technique is temporary and is non-vital to cells. They also report conducting immunophenotyping, and live cell calcium imaging using Fluo-4 AM and confocal microscopy.

Kapr et al. used alginate, gellan gum (GG) and laminin-based hydrogels to 3D bioprint hiPSCs and NPCs emulating CNS models [129]. Most of their cellular characterization and assessments were done via the mixing of hiPSC-derived NPC spheres within the optimal bioinks. The spheres were chopped and "embedded" into the gels and analyzed over 21 days. They noted thick bundles of BIII tubulin+ and F-actin, and differentiation into neurons (BIII-tubulin+) dopaminergic neurons (TH+) and astrocytes (GFAP+), and similar results were found in pre-differentiated NPC spheres. However, it was noted that in the absence of pre-differentiation, complex, multicellular tissues were formed within 3 weeks, while pre-differentiating led to limited extension, but generated a 3D multicellular network within 1 week. The two models could be used for long-term disease modeling in the former, and screening applications in the latter. The only characterization done for 3D bioprinted constructs was viability on day 3, which showed ~ 62 % viability.

De Melo et al. printed mice-derived astrocytes in gelatin, GelMA, fibrinogen, and laminin-containing bioink to model mouse brain modulus values (although no mechanical characterization was described in the protocol) [130]. Their bioink was crosslinked with thrombin, CaCl₂, photoinitiator and UV light for two consecutive 60 s intervals. Lower printing speeds favoured increased viability (74.08 % ± 1.33 % after bioprinting, 83.54 % ± 3.00 % after 1 week) and the bioinks could be printed into various complex geometries. They found that printing astrocytes had lower viability compared to 2D controls but enriched the typical morphology of *in vivo* interconnected astrocytes. In addition, the astrocytes maintained relevant phenotype (GFAP+) after 7 days.

Sullivan et al. investigated the use of 3D bioprinting for creating stem cell-derived CNS models, focusing on the development and application of bioinks [131]. The researchers developed a biocompatible PEG-based matrix incorporating peptide motifs and collagen IV to simulate human brain stiffness (1.5 kPa). Using a commercial bioprinter, they successfully integrated cells resembling brain microvascular endothelial cells (BMECs), NPCs and astrocytes, highlighting its potential for creating complex multicellular models. The study highlights the value of 3D bioprinting in generating *in vitro* models that closely resemble the human CNS environment, including increased spontaneous calcium transients and signal intensity after 4 weeks. They also explored how 3D bioprinting enhances the growth of astrocytes, vasculogenesis, and neural differentiation. The bioinks used supported the development of intricate 3D structures that improve the function and differentiation of

Table 5

Summary of the included articles based on generic models of the CNS.

Source	Printed Bioink Composition		Cells	Construct Media	Bioprinter	Characterization	
	Bioink	Crosslinker				Bioink	Cells/Construct
Haring et al., 2019 [132]	(1) Chelating neural bioink = PF127-SH (9 %, 12 wt%), DC-HA (1 wt%), DC-Gel (2 wt%) (2) Photocured neural bioink = PF127-SH (12 wt%), DC-HA (1 wt%), DC-Gel-MA (5 wt%)	(1) Ferric nitrate (50 mM, 2 mins) (2) PI (DMPA; 0.1 wt%)	Rat Schwann cells through 10 min exposure to UV light	Phenol-free DMEM (3.2 × 10 ⁶ or 2 × 10 ⁶ cells/mL)	Custom micro extrusion 3D bioprinter (27 G tapered needle; 1 mm/s; 2–10 psi) CELLINK INKREDIBLE+ (PC12; 4 × 10 ⁶ cells/mL) Human glioma cells (DS4-MG; 4 × 10 ⁶ cells/mL)	Gelation temperature (Differential scanning calorimetry) Rheology (frequency and stress sweeps) Velocity profile (finite element modeling software) Elastic modulus (dynamic mechanical analyzer)	Viability (AlamarBlue assay; D1, 3, 7) Fluorescence microscopy (D1, 3, 7)
Tomaskovic-Crook & Crook, 2020 [128]	Agarose (1.5 %), CMC (5 %), alginate (5 %) *Can add penetrating conducting polymer (CP)	CaCl ₂ (2 %)	hNSCs (10x10 ⁶ cells/mL)	hNSC Proliferation Medium ^a hNSC Differentiation Medium ^b	EnvisionTEC 3D Bioplotter	*Previously done	Viability (D1, 7) Membrane permeant live cell neural labeling (NeuroFluor NeuO) ICC (not specified) Live Cell Calcium Imaging (Fluo-4 AM)
Kapr et al., 2021 [129]	Alginate (1.5 %), gellan gum (0.5 %), laminin (0.01 %)	CaCl ₂ (0.09 M, 5 mins)	hiPSC-derived NPC spheres (4.9 × 10 ³ spheres/mL gel)	Differentiation medium	EnvisioTEC 3D-Bioplotter (Manufacturers Series; 37 °C; 0.1 bar; 31–33 mm/s; 200 µm ID)	FTIR SEM (surface) Mechanical testing (unconfined compression tests, gel stiffness, stress relaxation) Degradation (mass over 21 days) Printability	Viability (Live/dead; D7) ICC (TUJ1, GFAP, S100β, F-actin, TH, Hoechst, D21) Calcium imaging (Fura-2; D21) 3D bioprinting constructs: Viability (Live/dead; D3) Print speed (Viability; D7) Viability (Live/dead, D0, 7) ICC (GFAP, F-actin, DAPI; D7)
de Melo et al., 2021 [130]	Gelatin (4 % w/v), gelatin methacryloyl (GelMA, 2 % w/v), fibrinogen (3 mg/mL), PI (0.5 % w/v), laminin (2 µg/mL)	Thrombin (1 U/mL), CaCl ₂ (10 %, 1:9, CaCl ₂ : thrombin) UV crosslinking (2 x 60 s)	Cortical Astrocytes from Mice (1x10 ⁶ cells/mL)	Astrocyte culture medium (DMEM/F12, 10 % FBS, 2 % glutamine, 1 % P/S)	Extrusion-based bioprinter (grid construct; 6 x 6 mm; 6 layers; 400 mm/min; 22 G; 2D control)	Printability (Bioink's ability to print different shapes)	Printability (Bioink's ability to print different shapes) Viability (Live/dead, D0, 7) ICC (GFAP, F-actin, DAPI; D7)
Sullivan et al., 2023 [131]	PEG, RGD peptide, YIGSR peptide (Tyr-Ile-Gly-Ser-Arg) *Concentrations unknown, modulus of bioink was 1.5 kPa variation	Activator solution (Inventia Life Sciences), collagen IV (3 mg/mL), cells	iPSC-derived BMEC-like cells (iBMECLs; 10x10 ⁶ cells/mL) Astrocytes (5x10 ⁶ cells/mL)	BrainPhys™, NeuroCult (1:50), N2 (1:100), BDNF (20 ng/mL), GDNF(20 ng/mL), cyclic-AMP (1 mM), Vitamin C (200 nM) NPCS (10x10 ⁶ cells/mL)	RASTRUM Bioprinter (Inventia Life Sciences)	Stiffness (unknown method)	Viability (Live/dead; D1) ICC (GFAP, S100β, Nestin, PAX6, MAP2, Ve Cadherin, Occludin, PECAM-1, Laminin α4, GLUT-1) Interleukin 6 (IL-6; ELISA) Calcium imaging (4 weeks)

^a Complete NeuroCult Proliferation Medium comprising NeuroCult NS-A Basal Medium and NeuroCult NS-A Proliferation Supplement, supplemented with heparin (2 µg/mL), epidermal growth factor (EGF, 20 ng/mL), and basic fibroblast growth factor (bFGF, 20 ng/mL).

^b DMEM/Ham's/F² Nutrient Mixture (F-12):Neurobasal Medium, 1:1 (v/v), supplemented with 1% NeuroCult SM1 neuronal supplement, 0.5% N2 Supplement-A, 1 GlutaMAX Supplement.

CNS cells. This research suggests that bioink-based 3D bioprinting could be pivotal for modeling and studying CNS disorders *in vitro* and facilitating high-throughput drug discovery.

Haring et al. designed multi-CNS and PNS constructs from ECM-based polymers (HA, gelatin) that were dopamine conjugated (DC) combined with the synthetic polymer Pluronic F-127 (thiolated, PF127-SH) to enhance biomimicry, printability, and mechanical relevance [132]. Since both CNS and PNS components were integrated into the model, this article was deemed relevant, despite the PNS modeling which typically warranted exclusion. Two bioinks were investigated: a

chelating bioink (12 wt% PF127-SH, 1 wt% DC-HA, 2 wt% DC-Gelatin) and a photocured neural bioink (12 wt% PF127-SH, 1 wt% DC-HA, 5 wt % DC-GelMA) printed with Schwann cells (PNS), human glioma cells and rat neuronal cells (CNS). They conducted extensive mechanical characterizations in response to the traditional lack of rheological optimization, but limited investigation was done on the functional performance of the models. Similar viability was found between the photocured ink and the alginate control, but the chelated ink had higher viability on day 7 for Schwann cells (~80 % AB reduction after 7 days). Each cell type (human glioma cells, rat neural and rat Schwann cells)

was separately mixed with a 9 % PF127-SH chelating bioink, which crosslinks using ferric nitrate, printed as single layers and cultured for 7 days. Fluorescent microscopy was used to image the tagged cells in the constructs on days 1, 3 and 7. The authors note that the cells exhibited “reasonable morphology”, and that viability “remained high” but did not conduct a quantitative assessment.

3.1.4.2. hiPSC expansion. The work of Lindsay *et al.* fabricated NPC expansion lattices to generate high-quality NPCs for various CNS dysfunction therapies [133]. While not typically designed for neural tissue simulation, it was included since the methods therein have application to neural tissue engineering using similar principles. Interestingly, they used low concentrations of calcium (8 mM CaSO₄) to crosslink alginate before printing. Higher concentrations of crosslinker were used post-printing to enable mechanically stiff materials that could be easily remodelled by proliferating cells and dissociation for NPC removal. During their initial bioink optimization (assessed various blends of low-viscosity, very low-viscosity alginate, and RGD-modified low-viscosity alginate) they found that RGD-modified was not as efficient at enhancing NPC proliferation compared to higher modulus RGD-free bioinks; therefore, only low viscosity alginate was explored. Printing of low-viscosity alginate was possible due to pre-crosslinking and printing into a support bath of gelatin, CaCl₂ (10 mM) and P/S (Supplemental Information, Table S3). The concentration of NPCs was relatively high (30×10^6 NPCs/mL). 5 mM of Ca²⁺ was also supplemented in the media (Stemness Maintenance Media), where lower Ca²⁺ concentration favoured expansion and maintained expression of stemness maintenance markers (Nestin, SOX2) compared to higher concentrations (30 mM). The higher concentration of calcium also showed increased GFAP – likely due to the increased stiffness promoting differentiation. The constructs favoured increased metabolic activity until 2 days post-printing, which plateaued up to 7 days. All cells were positive for SOX2 and Nestin, but only some expressed Ki-67, indicating that only some cells were proliferating. This model showed relatively high cell viability (~80 %) and demonstrated renewal within the constructs (Stemness Maintenance Media, SOX2+, Nestin+), and could differentiate once extracted (Mixed Differentiation Medium, BIII tubulin+, GFAP+) indicating their ability to retain multipotency (also confirmed using ICC and RT-qPCR). Similar work was done by Q. Li *et al.*, who used a PG-matrix-M based hydrogel to encapsulate and bioprint hiPSC in a sheet that maintains pluripotency and spheroid formation [134]. Their PGmatrix-M comprises a modified triblock amphiphilic peptide (h9e), where the amino acids encode proteins of human muscle and β-spiral motif of the spider flagelliform silk proteins. The self-assembly of the peptides forms nanofibers which generate reversible sol-gel materials under physical conditions, which required no additional crosslinking and remained stable in culture medium for up to 3 months. They propose this as a scalable and efficient way to generate mass amounts of hiPSCs compared to traditional methods (microarray molding or U-bottom plates). Interestingly, they found that gel strength and porosity had a limited effect on proliferation and viability, but seeding density was more influential. Importantly, up to 37 passages could be conducted with the hiPSCs within a 0.5 % peptide concentration, signifying long-term culture. The 3D method showed superior expansion efficiency and maintained pluripotency markers, where printed spheroids had enhanced SOX2, REX1, ESG1, SOX1, and decreased Brachyury compared to pipetted spheroids in the same matrix.

3.2. Bioinks

Bioinks provide structural and chemical support for the formation of functional neural networks, which were shown to vary throughout the literature. Pei *et al.* outlined that the most conducive design for brain tissues is to use bioinks and geometries that achieve the layered gradient of the cerebral cortex and recommended that bioprinted constructs be

formed using multi-component bioinks of varying concentrations, have moduli of 1000 Pa, and have appropriate porosity, with pore sizes between 30 – 150 µm [9]. Han *et al.* noted the importance of investigating different bioinks to find suitable environments for stem cell survival, differentiation and function [120]. One of the most challenging components of 3D bioprinting neural tissue models is the intricate balance between generating relevant tissue constructs that resemble the soft brain tissue but are structurally viscoelastic to achieve high-fidelity printing and enhanced cell survival [113,132]. Many groups have aimed to investigate the optimal microenvironments for neural tissue models by refining various polymers, additives, cells, and geometries into the bioprinting workflows. These components are summarized in the following sections.

3.2.1. Polymers

As mentioned, various polymers were used for the 3D bioprinted models ranging from natural (alginate, gelatin, fibrinogen, GelMA, HA, etc.) to synthetic-based polymers (Pluronic F127, PEDOT-based, PEG-based, etc.). The importance of bioink optimization was noted as optimal bioinks should target the mechanical properties of desired native tissues and should permit cellular interaction and proliferation. Polymers offer the main network for cell support, proliferation and degradation of 3D bioprinted materials. Hydrogels provide many benefits in bioink preparation including their high water content, biocompatibility, mechanical properties, and cell adhesion properties. Common polymers have been reviewed elsewhere, and here we focus on key insights regarding polymers from the reviewed literature. Different mechanical and physical properties are needed depending on the application. For example, shear thinning and conductive properties may be more beneficial for nerve regeneration applications [121] but for generating representative neural models it requires mechanical and structurally patterned relevance. Factors that inherently influence cell differentiation are related to bioink composition and printing properties [99], highlighting the importance of bioink selection.

3.2.1.1. Alginate. Alginate was the most ubiquitous polymer bioink in the reviewed literature. Alginate has favourable properties due to biocompatibility and enhanced mechanical properties and printability while being capable of degrading within the construct, providing favourable environments for cellular proliferation and differentiation. These benefits are emphasized through the mixture of alginate with multiple other polymer types. Alginate has the potential to be tuned for specific mechanical stiffness, but importantly contains reversible bonds, which is imperative for cellular remodeling, and enabling interactions between cells [133]. Intuitively, there is an equilibrium that must be achieved between wanting prolonged stability in the case of disease modeling (the phenotype must have enough time to appear) and allowing cellular remodeling, which is necessary to induce communication and function between cells.

Given its low cell adhesion, few studies printed with alginate alone, where its solitary use was done for pre-crosslinking with CaSO₄ [133]. As a control, Haring *et al.* used 1.5 % alginate (crosslinked with 100 mM CaCl₂) as a bioink and saw increased viability over 7 days with Schwann cells [132]. However, Kapr *et al.* showed that pure alginate gels deformed during crosslinking (0.09 M CaCl₂) but could maintain over 50 % viability after 7 days [129].

In Gu *et al.* they note that low-viscosity alginate (100–300 cP) is typically used to support the hNSC survival during printing [100]. Beyond cellular support and tissue relevance, some studies noted that alginate was useful for characterization techniques. For example, higher alginate percentages were used to enhance the potential for sectioning tissue constructs for calcium imaging since the stiffer materials could be more easily processed [129].

3.2.1.2. GelMA/Gelatin. Gelatin methacrylate or gelatin methacryloyl [109] was used in approximately 11 % of all investigated studies. Gelatin has arginine-glycine-aspartic acid (RGD) and matrix metalloproteinase (MMP) recognition sequences within its chain [116], making it beneficial for bioink selection. In addition, both gelatin and GelMA have thermally reversible gelation kinetics, which is desirable for extrusion-based bioprinting where lower temperatures lead to gelled materials with high fidelity [108]. However, since the viscoelastic properties have limited stability at physiological temperature [130], modified versions of gelatin, such as GelMA, are desirable to enhance mechanical features.

GelMA can be tuned to desired porosity, degradation and modulus values [130]. For example, higher concentrations of GelMA lead to faster gelation kinetics, but compromise the ability to sterile-filter the solution greater than 5 % w/v [130].

Typically, materials with high gelatin concentrations (>5% w/v) have low printability, but faster gelation kinetics and stiffer gels [108]. The choice of concentration should reflect the incorporated cell type, where neural tissues benefit from soft environments, but muscle cells can favour higher stiffnesses [108]. Han *et al.* reported that boundary cap neural crest stem cell viability was directly proportional to gelatin concentration (assessed between 4–15 % w/v), but 12 % gelatin was favourable with higher relative cell count and more elongated cells over 3 days, indicating attachment and proliferation [120]. Neufeld *et al.* used TG as a crosslinker to covalently crosslink glutamine and lysine residues on gelatin and to stabilize fibrinogen [126]. The addition of thrombin was necessary to initiate fibrinogen cleavage to effectively crosslink with TG, which yielded high modulus biomaterials [126]. This same study showed that gelatin concentration influenced swelling (12 % w/v gelatin had increased swelling compared to 3 and 6 %) and control the stiffness, but 6 % gelatin led to optimal Young's modulus of 24.5 ± 2.6 kPa [126]. Interestingly, one study initially investigated GelMA, gelatin and fibrinogen hydrogels to print spinal NPCs, but they found that after 4 days, viability was low (~20 %), so Matrigel was studied [118]. Therefore, careful consideration should be given to the cell types being used for optimal bioink selection.

3.2.1.3. Fibrinogen. Fibrinogen is a natural blood-derived glycoprotein that plays a role in the clotting cascade and has been used frequently in neural tissue engineering [102,126]. Fibrinogen concentrations influence the stiffness and porosity of bioinks, and its use promotes cell attachment. Notably, it is a favourable biopolymer since it contains cell-adhesion molecules, has slow gelation, and decreased mechanical stability [119], which allows for remodeling by proliferating cells. In addition, molecules such as genipin or TG can be added to enhance stability and promote neural outgrowth [119,126]. However, it was found in Neufeld *et al.* that TG (3 % w/v), fibrinogen (1 % w/v) with varying concentrations of gelatin (3, 6, and 12 % w/v) could not achieve relevant stiffness of neural tissues alone, and the addition of thrombin was necessary to cleave the fibrinogen [126]. Fibrin is a viscous polymer that limits its printability at high concentrations or when printed on its own [14]. In a protocol paper, de Melo *et al.* noted that fibrinogen (in addition to gelatin and GelMA) was added to increase cell-specificity, enhance printability, and physical stability [130]. Importantly, the versatility of fibrin was shown through its use in neural tissues and tumour models (Figure 3).

3.2.1.4. Chitosan/CMC. Chitosan was mentioned in seven of the included articles, but all containing the same formulations of fibrin and alginate bioinks crosslinked with genipin, thrombin and CaCl_2 . Chitosan enhances mechanical properties and providing sites for ionic or covalent attachment of other polymers/crosslinkers [119].

Four papers used modified chitosan, in the form of carboxymethyl chitosan (CMC) in their bioinks. Initial work by Gu *et al.* explored CMC, a chitosan-derived water-soluble polymer, which was shown to influence

hNSC viability during printing and after 9 days of culture [98]. CMC-based hydrogels were porous, where increased CMC% led to increased porosity and higher concentrations of CMC showed higher initial cell viability and better support over the tested timeframe.

3.2.1.5. ECM polymers. The ECM plays an integral role in cellular functioning and regulates cell differentiation, adhesion, and recruitment in the body, and therefore have recognizable advantages in neural tissue engineering. ECM proteins such as HA, collagen, and laminin have been commonly recruited in bioink development in the last ten years. HA is a hydrated glycosaminoglycan that is found in the ECM [132]. It was reported in an excluded study that HA forms an open lattice structure with fibrin for enhanced cell migration, but by itself has slow gelation kinetics and limited mechanical properties [135].

Collagen is an ECM polymer that influences pore size. In Pei *et al.*, as collagen concentration increased from 0.5 to 1.5 mg/mL, the pore size of the printed structure also showed a significant increase; this was used to design layered cortical resembling tissue models with heterogenous pore size distribution [9]. Similar to gelatin, collagen exhibits temperature-dependant gelation, which can be beneficial in extrusion bioprinting [65].

Laminin contains cell-surface receptors such as RGD, which leads to increased cellular anchorage and recognition [129]. When printing astrocytes, laminin incorporation enhanced viability, led to higher porosity (~50 %), a lower Young's modulus, viscosity and G', and an increased mass loss over time [130]. Kapr *et al.* opted for alginate and GG-based bioink, but also incorporated laminin due to its role in supporting cell viability and generating functional cellular networks [129]. Further, it was found in another study that when laminin was incorporated into 3D constructs, neural differentiation and morphology was enhanced [108].

Modifications to polymers to enhance cellular recognition and anchorage were also used. Lozano *et al.* used RGD-modified GG and showed increased cell attachment and proliferation of mouse primary cortical neurons [96]. They also showed that RGD-GG could be cross-linked with DMEM or CaCl_2 (1 M) for sustained viability. Matthiesen *et al.* found that fetal primary astrocytes had a higher degree of interactions using RGD-modified HA and IKVAV cell adhesion peptides [112]. In this study, adding RGD enhanced astrocyte viability but showed limited effects in promoting proliferation; however, for GBM (U87) cells, IKVAV appeared favourable for viability, but RGD had no effect. This is similar to the work of Lindsay *et al.*, who noted that RGD-alginate was not as efficient at enhancing NPC proliferation compared to stiffer RGD-free bioinks [133]. Together, these show that different cell lineages can be influenced by different microenvironments, and coalesced mechanical and functional characterizations should be assessed.

Dopamine can also be added to enhance cell adhesion, increase flexible elasticity and neuron interaction. In Haring *et al.*, dopamine was conjugated to both HA and gelatin to 3D bioprint various cell types [132]. While comparisons were made between the type of crosslinking (chelated with iron or photocrosslinked), there was enhanced viability after 7 days for Schwann, glioma, and neuronal cells in both systems.

Other ECM-like materials were also used such as Matrigel – a mouse-derived material containing growth factors and proteins that resemble the basement membrane that is routinely used in cell culture [118]. For example, Joung *et al.* found that 50 % Matrigel had superior mechanical properties and viability to bioprint spinal NPCs and oligodendrocyte precursors (OPCs) in a spinal cord model [118]. Matrigel was favourable for spinal NPC culture, with viability > 75 % after 4 days. The amount of Matrigel was critical, where low amounts led to softer gels resembling 2D conditions and high percentages (>75 %) had higher aggregation and decreased axon length [118]. In Yan *et al.*, Matrigel was investigated within their bioink compositions, which showed high viability (92.19 ± 4.26 %), however, the Matrigel caused clogging in the nozzle while

printing [14].

Q. Li *et al.* used a peptide polymer (h9e) to generate a self-assembling PGmatrix hydrogel, capable of reversible sol–gel transitions on a fast timescale (100 Pa after few seconds, shown through rheology) [134]. They investigated various concentrations and temperature preparations during optimization and found that each concentration (0.2, 0.5 and 1% peptides) had ~ 95 % recovery after 10 min; the entangled fibrous network was also accompanied by single nanofibers ~ 20 nm in diameter and nanofiber cluster around 100–500 nm. They saw heterogeneous pore sizes, but the PG matrix had poor printability, so increasing the hydrophobic segment was considered (PGmatrix-M). Compared to PGmatrix, PGmatrix-M had similar shear thinning, but higher viscosity and faster self-healing properties (84–94 % recovery by 1 min), had heterogeneous porosity (200–1800 nm) but more uniform nanoweb. Further, Cruz *et al.* used a naturally derived polymer, Geltrex™, which combines common ECM polymers, which was shown to significantly enhance NPC viability over 6 days and provide an environment suitable for NPC proliferation [116].

Finally, Rueda-Gensini *et al.* generated ECM-derived bioinks from small intestine submucosa (SIS) powder from porcine and functionalized with MA (SISMA) in addition to fibronectin-coated graphene oxide (GO) nanoflakes to generate conductive polymers (SISMA-GO) [10]. These systems could be tuned mechanically via blue light crosslinking with high stability, and the concentration of SISMA/SISMA-GO was shown to influence stiffness and cell viability. The incorporation of SISMA-GO also enhanced synaptic activity. The prevalence of ECM-based polymers emerging in the literature is promising for the development of biochemically and biomechanically relevant neural tissues that promote cell adhesion, proliferation and differentiation.

3.2.1.6. Pectin. H.-W. Lee *et al.* combined methacrylated silk fibroin (SilMA) with pectin, a polysaccharide derived from plants, or pectin methacrylate (PecMA) [95]. The materials were biocompatible, porous, and sustained neural cell growth and differentiation. Importantly, the addition of pectin was beneficial for improving printability and low modulus values, and the constructs had high fidelity which permitted orientation into complex geometries. Alone, SilMA had good biocompatibility and mechanical properties, however, incorporating pectin into the bioinks increased swelling, allowing for more favourable environments for the exchange of waste and nutrients. Compared to the SilMA/pectin, PecMA and silk fibroin hydrogels obtained weaker mechanical properties post printing, suggesting its combined use in bioinks for enhanced mechanical stability.

3.2.1.7. Synthetic polymers. Besides the naturally derived polymers discussed, synthetic polymers have value when supplemented into the design of 3D bioprinted neural tissue engineering – either in the bioinks or as sacrificial frameworks. The most commonly used synthetic polymer was Pluronic F127, which is a soft and biocompatible copolymer of polyethylene oxide and polypropylene oxide that displays thermally reversible and shear thinning behaviour [126,132]. Haring *et al.* used a combination of natural (HA and dopamine-conjugated gelatin) and synthetic thiol-modified Pluronic F-127 (PF127-SH) [132]. The concentration of PF127-SH directly influenced the viscosity, gelation temperature, and higher concentrations led to more stable bioinks. Oftentimes, studies use the thermally reversible properties of materials such as gelatin and Pluronic F127 to generate sacrificial frameworks to enhance the organization and functional properties of the 3D bioprinted materials. In Neufeld *et al.*, Pluronic F127 was used as a sacrificial material to fabricate embedded vasculature within their 3D printed model; upon liquidation, it created a 3D lumen vascular structure [126].

Song *et al.* integrated the electroconductive additive of PEDOT to promote NSC differentiation due to its high electroconductivity and chemical stability [121]. The bioink was composed of PEDOT, chondroitin sulfate methacrylate (CSMA) and tannic acid (TA) – PEDOT:

CSMS, TA (PECT) – with GelMA and PEGDA to bioprint representative physiochemical spinal cord tissues. It was suggested that for *in vivo* transplantation, other formulations with enhanced biocompatibility and elimination are recommended.

PEG-based polymers were also used in bioink formulations. Gomila Pelegri *et al.* used a PEG-based matrix to enhance the formation of neural subtypes, particularly oligodendrocyte formation from ADSCs [2]. Matthiesen *et al.* used an 8-arm azide-modified PEG to design copper-free click chemistry bioinks connecting between modified HA (HA-BCN) [112]. The addition of either RGD or IKVAV into the (PEG-Az)₈ and HA-BCN matrices was necessary to enhance cell attachment and viability.

3.2.2. Additives

Bioinks often contained support molecules (additives) that were investigated for a host of reasons, such as increasing conductivity, differentiation or rheological benefits. While not investigated in their work, Haring *et al.* referenced other research that had added nano-fibrillated cellulose or clay nanoparticles for enhancing mechanical stability but suggested that these conditions may negate the soft requirements for differentiation [132].

Sharma *et al.* integrated guggulsterone-releasing MSs to initiate neuronal differentiation to a dopaminergic state [103]. The MSs led to an increased percentage of TUJ1 and GFAP, TH and O4 based on quantitative flow cytometry after 30 days. qPCR was used to evaluate the relative gene expression, showing that the MSs led to enhanced TUBB3 (compared to soluble guggulsterone), TH (compared to unloaded MSs), and PAX6 (compared to unloaded MSs). Notably, the incorporation of MSs enhanced access to soluble factors necessary for growth and differentiation. Benwood *et al.* also incorporated small molecule releasing MSs into their AD model printed with NPCs [107]. In this work, puro-releasing MSs were used to direct NPCs to cells resembling basal forebrain cholinergic neurons. Printing with the MSs showed a slight increase in cell viability after 1 day of printing (63 % in the control, 73 % with MSs), but this was not statistically different, nor were differences found over 45 days in the healthy cells. In the AD models, the MSs showed decreased viability compared to the control after 30 days, but this was drastically reversed after 45 days, where the viability was ~ 80 % at day 45 post-printing with the MSs. Importantly, the MSs increased the relative rate of electrophysical maturity, but the resting membrane potentials were relatively high compared to *in vivo* conditions, indicating that the cultures holistically were electrophysically immature.

J. Li *et al.* integrated tetrapodal-shaped zinc oxide (t-ZnO) micro-particles into the bioink to develop biosensing capabilities for the detection of dopamine in the 3D bioprinted constructs [117]. They were able to show that the t-ZnO micro-particles have high selectivity and specificity for dopamine released *in vitro* and suggest the potential for these to monitor neurotransmitter release in 3D bioprinted models in the future [117].

3.3. Cell types

3.3.1. Single culture

Most of the literature in the past decade of our investigated cohort has explored 3D bioprinting of monocultures ($n = 35$). It should be noted that some cell types, such as hiPSCs, NSCs or NPCs can be differentiated into multiple cell types within the same construct, but these are still considered as monocultures. The cells that were printed varied, but typically reflected the model type or application. Most often, hNSCs were printed, but tumour cells (U87, SH-SY5Y), and hiPSCs were also routinely used. Human astrocytes, neural cells (rodent) and both human- and rodent-NPCs were also commonly employed for single-culture bioprinting. MSCs, which were first printed in Restan Perez *et al.*, can also be used for neural tissue modeling [104]. Namely, they note that there are several benefits of MSCs over hiPSCs, including

procurement, robustness during printing, and their higher proliferation, expression and electrophysical activity make them viable candidates for 3D bioprinting (including references therein) [104]. Similar benefits were also noted for ADSCs, due to their abundance and relevance to neural tissues [2].

The printing of single cell cultures is beneficial in optimization studies to assess the influence of various 3D bioprinting parameters. However, these unimodal tissues have limited relevance to the complexity of the human brain and co-culturing should be the goal of regenerative medicine in the future to design complex functional neural networks.

3.3.2. Co-culture

The functional complexity of the brain inherently depends on multifaceted networks from all cell types that contribute to brain function, aging, and disease pathophysiology. Most co-cultures explored in the systematic review combined glial cells, such as astrocytes, with neural cell types or glioma cells. Interestingly, astrocytes were the primary glial cell type co-cultured with varying neural cells (hNSCs, hNPCs – GABAergic and glutaminergic). Astrocytes and HUVECs were often integrated into co-cultured tumour models of GBM and neuroblastomas. Astrocytes play key functional and regulatory roles within the CNS relating to synaptogenesis and neurotransmitter recycling and are highly regulated by the ECM [112]. Astrocytes are known to influence immune response, maintenance of the BBB, neurogenesis and astrogliosis [130]. Therefore, astrocyte inclusion in 3D bioprinted neural models is necessary to understand fundamental functions, including neurological disorders. Including other glial cell types of integral to brain function, such as oligodendrocytes, endothelial cells and microglia, would also be conducive in neural tissue design, especially since current research has not investigated these interactions in 3D systems and mimicking inflammatory response is crucial for understanding the influence of drug therapies.

Y.-C. E. Li *et al.* investigated bioprinting neurospheroids into an astrocyte-containing support bath to generate a co-culture [108]. Support cells such as astrocytes play a crucial role in regulating functions within the brain stemmed from tight cellular interactions. In particular, astrocytes play a role in the initiation of neurogenesis, a critical function in tissue injury. The authors note that these mechanisms should be studied *in vitro* to understand fundamental cellular behaviour. In their study, rodent-based NSC-derived neurons and cortical astrocytes were patterned to mimic the anisotropic structure of the subventricular zone of the brain. Notably, astrocytes may enhance neuronal differentiation due to the higher TUJ1+ expression at the printed niche, and also alluded to the role of astrocytes in glutamate-glutamine cycle [108]. Further, a study by Zhou *et al.* where they co-printed NSCs and astrocytes using a droplet-based method highlighted the fundamental biological signalling and recruitment between astrocytes and maturing neurons [97]. In both co- and tri-culture GBM models, Neufeld *et al.* showed that in the presence of astrocytes, there was increased cell growth and invasion, and the triad of GBM, astrocyte and human microglial cells led to changes in tumour-dependant pore sizes [126]. Therefore, the incorporation of multiple cell types, such as astrocytes and microglia, can provide key insight into biochemical interactions between cells.

Kajtez *et al.* conducted a proof-of-concept printing of astrocyte-fate cells (derived from forebrain hNSCs) surrounding neural-fate cells (derived from ventral mesencephalic hNSCs) [65]. They showed distinct phenotypes on the inner and outer regions (β -III tubulin+ and GFAP+, respectively) after 4 weeks, but suggest the use of these patterning to investigate cellular interactions in the future [65]. One of the most intricate neural tissue models included in the systematic review was the work of Yan *et al.*, who printed multiple combinations of neural progenitors (glutamate, GABA, striatal) and astrocyte progenitors within a fibrin- and HA-based bioink [14]. The research included comprehensive mechanical and cellular characterization of systems that modeled

interactions between cells of the same tissues, between tissues and in disease models (Alexander disease). However, only a single layer of horizontally patterned constructs was printed due to the low-modulus bioink, where the height of their models was approximately 50 μm . Future work should aim to replicate the intricate modeling and characterization conducted herein using more archetypally relevant geometries of the human brain.

Co-culturing was also intuitive for tumour models. In a GBM model, X. Wang *et al.* demonstrated that when HUVECs and U118 cells were co-cultured, there was enhanced tubular morphology and expression of tumour-related markers (CD31, VEGFR2) [122]. In Tang *et al.*, HUVECs (CD31+) were shown to migrate toward GBM cells (SOX2+), which had spatially close connections and vascular morphology in the HUVECs [125]. They were able to demonstrate cellular crosstalk and key GBM features of angiogenesis, tumour invasion and drug resistance. As mentioned, co-culturing relevant cell types that represent the regional differences within the brain should be the focus of future work to elucidate key chemico-physical interactions in 3D bioprinted neural models.

3.4. 3D bioprinted constructs

3.4.1. Geometries

Various construct architectures were generated which reflected the application of the bioprinted neural tissues. For example, dome-shaped constructs were fabricated to produce similar architecture to the human brain [103–105,107], but grid shapes, either printed in single or multiple layers, were most often produced ($n = 16$). One paper had unspecified geometries, where no specified construction was provided in the methods or visually in the figures [114]. Vascularization architectures were generated by Neufeld *et al.* and Kajtez *et al.* using sacrificial materials of Pluronic F127 and gelatin, respectively [65,126]. Vascularization in bioprinting constructs can ensure oxygen supply within complex structures, and connection to peristaltic pumps resembling *in vivo* circulation. Both models showed the ability for perfusion through the vascular channels, supporting their relevance in neural models, especially those relating to the highly vascularized BBB [65,126]. More research should be done to understand the potential of these vascular networks in cellular interaction, proliferation and differentiation.

Han *et al.* compared the printing of multiple layers (1, 3, and 5 layers) and found that more layers supported higher cell viability over 3 days [120]. Interestingly, Kajtez *et al.* used oxygen-sensing particles to track oxygen levels within their 3D SHAPE composites [65]. For this, the oxygen-sensing microbeads were embedded either in the printing support or within the bioink, and their association was co-analyzed with calcein-AM stained cells using a fluorescence and phosphoresce microscope. They analyzed oxygen progression over 50 days and identified that the geometry influences oxygenation. Importantly, it was found that when printed with cells, a higher infill density led to lower O₂ percentage compared to lower (or wider/spaced) infills. This has important implications in the design of constructs, where the maintenance of oxygen levels is crucial to modeling *in vivo* conditions. It was suggested that this technique could be used to measure oxygenation at desired times and suggest using this for timing of switching to differentiation media, since cells will consume oxygen during proliferation, and their plateau correlates with a plateau in O₂ %. However, this type of analysis would require the integration into the hydrogel system.

3.4.2. Culturing timeline

The 3D bioprinted constructs also displayed varying times of construct culture (Figs. 4 and 5). Both Yan *et al.* and Kajtez *et al.* assessed their construct functionality (ICC) up to 60 days post-printing [14,65]. Several studies investigated culturing at 30 days or more for ICC, viability, RNA expression (RT-qPCR), electrophysiology- and metabolic-related characterizations. The length of construct culture should reflect the need of the investigated systems. For example, neural tissue

investigation modeling disease pathology should have sufficient time for the emergence of disease-related phenotypes. In general, longer culturing timelines allowed for the enhancement of distinct cellular networks. This was shown in Kajtez *et al.* where after one month, neural-fate hNSCs printed in the center of an outer ring of astrocyte-fate hNSCs (with a 'ECM' separating region) remained unconnected; however, when hNSCs were printed in a grid geometry, after 2 months highly interconnected networks were observed [65]. Yan *et al.* also showed that as culturing time increased, more synaptic puncta were observed after 60 days compared to 20 and 43 days post printing, and this was significantly enhanced when glutamate and GABA neurons were co-cultured [14]. Further, electrochemical signals relating to glutamate recycling, and calcium imaging also increased with culture time, indicating the importance of assessing construct functionality over an appropriate timeframe.

3.5. 3D model characterization

The characterization of the 3D constructs remains the most crucial component of assessing the functionality and appropriateness of 3D neural tissue models. Yet, these characterization methods are variable and inconsistent between the work done on constructing neural models to date. The importance of characterization and lack of thorough investigation was highlighted in Fantini *et al.*, who emphasized the poor characterization of bioinks for cell viability [101]. Lindsay *et al.* defined ideal bioinks as those with mechanical support before and after printing, maintaining cell viability, being able to be remodelled by cells, and enabling effective withdrawal of cells from the constructs [133]. The latter point is more conducive to their application of expansion lattices but has application in characterization methods of 3D bioprinted neural tissues. For example, for phenotyping, access to the cells within the middle of the construct is necessary; if effective 3D visualization without deforming the construct cannot be achieved, which is a major current limitation, cells must be extracted to fully understand the wholistic phenotypes of the tissues.

3.5.1. Material properties – Without cells

The success of 3D bioprinting in creating functional brain tissue depends on the intricate interplay between scaffold properties and cellular behaviour. Typically, the material properties of the crosslinked hydrogels are characterized by their mechanical properties (rheology, compression), physical properties (SEM, FTIR), and printability prior to cell integration. These characteristics are not just structural concerns but pivotal factors influencing the fate of embedded cells. These properties determine the microenvironment that cells encounter, which in turn affects cell survival, proliferation, differentiation, and integration into the engineered tissue. Understanding these relationships is crucial for designing scaffolds that can accurately mimic native brain tissue, providing appropriate biochemical and biophysical cues to guide cell behaviour and tissue formation.

3.5.1.1. Mechanical properties. Brain tissue studies show significant variability due to differing protocols, making it crucial to select methods aligned with specific modeling goals [136]. Brain properties vary by region and pathological condition [125,126]. For example, tumour regions in mice and humans show higher storage and complex modulus. Also, inter-species differences are significant, while age mainly affects comparisons between children and adults [136]. Considering the aforementioned criteria, these factors are essential for realistic brain tissue modeling. However, studies lack standardized parameters for testing properties against brain tissues, hindering result benchmarking and tissue replication. Thus, standardized testing parameters are essential for reliable and reproducible research in this area.

Amplitude sweeps are among the frequently used methods to study the viscoelastic behaviour of 3D bioprinted structures by giving storage

(G') and loss (G'') modulus [95,112,133]. While G'' represents the material's liquid-like behaviour, the storage modulus reflects its ability to store energy during deformation, indicating its elastic behaviour. A higher G' corresponds to greater stiffness, meaning the material resists deformation more effectively. The stiffness of 3D bioprinted constructs affects structural integrity and cellular responses. It has been suggested that neural stem cells tend to differentiate into neurons in a softer matrix with E < 1.5 kPa (where E represents the Elastic modulus), whereas glial differentiation happens in a stiffer matrix [129]. However, no difference in NPC stemness was observed with varying matrix stiffness of covalently crosslinked protein hydrogels [133].

Stiffness can also be calculated as the slope of the linear region of the stress-strain curve and is significantly influenced by the composition and concentration of the polymers [9,108,110,116,125,126,129,132]. Stiffness also affects cell viability and morphology. For example, a softer hydrogel (0.6 kPa vs 7.9 kPa) promoted higher astrocyte viability and lower cell circularity over 14 days [110]. In disease modeling, hydrogels should mimic the heterogeneity of the brain. For example, a tri-regional model of GBM was achieved by varying matrix stiffnesses of 2 kPa for the soft, healthy region, 7.3 kPa for the tumour site, and endothelial regions 0.45 kPa [125]. These findings emphasize the importance of carefully adjusting hydrogel stiffness to balance mechanical stability with biological functionality, particularly when modeling the complex and soft environment of brain tissue (E = 0.6–1.1 kPa) [108].

Apart from post-printing, the rheological properties of pre-printed bioink are also deciding for successful 3D bioprinting of brain tissue. For extrusion bioprinting, viscosity and shear-thinning behaviour are of high importance, which infers how well a bioink can be extruded and maintain its shape post-printing [113,121,133]. Viscosity also plays a critical role in preventing cell sedimentation within the bioink during the printing process, as higher viscosity can help keep cells evenly suspended, ensuring uniform cell distribution in the final printed structure [133]. Having the viscosity curve, the shear thinning property can be quantified using the following power-law equation:

$$\eta = K \bullet \gamma^{(n-1)}$$

where η is the viscosity, K denotes the consistency index, and γ is the shear rate [113]. The flow index "n" represents shear thickening ($n > 1$), shear-thinning ($n < 1$), or Newtonian ($n = 1$) fluids. Additionally, an oscillatory time sweep with high and low strains can help observe the ability of bioink to regain the initial storage modulus after being exposed to high-shear strains during the printing process, which can impact its structural fidelity [113,121,132,133].

Low viscosity bioinks pose a challenge for maintaining shape fidelity during printing. The FRESH technique addresses this by using a removable support bath, creating precise structures. The rheological properties of the bath are also critical as it needs to provide solid-like support under low shear and transition to a fluid-like state under higher shear stress. Notably, studies by Kajtez *et al.* and Y. Li *et al.* have conducted in-depth analyses of rheological properties for their bioink and support baths, demonstrating the importance of fine-tuning these parameters for 3D bioprinting [65,108].

3.5.1.2. Physical properties. The wettability of a polymer surface, measured by water contact angle and influenced by functional groups, is essential for cell-material interactions as it affects protein adsorption [137]. Also, mammalian cells prefer surfaces with a slightly positive charge due to the negatively charged membrane. Positively charged surfaces, such as amine-modified surfaces, can facilitate better cell attachment through electrostatic interactions, enhancing neuron adhesion and growth [137,138]. Surface morphology, often examined using SEM, is also key to cell attachment and interaction [96,113,123]. De Melo *et al.* reported that increased porosity percentage favoured cell interconnection and nutrient exchange [110]. Small pore sizes can obstruct the transport of nutrients and oxygen into cells, resulting in

necrotic areas [113]. Additionally, pore size is critical for the proliferation of neural cells; larger pore sizes are conducive to vascularization and neuronal differentiation [7,95,139]. It has been suggested that structures imitating the cerebral cortex should have an internal pore size of 30 to 150 µm and a modulus close to 1000 Pa [9]. Notably, studies have shown significant variation in pore sizes within constructs [9,96,98]. For instance, Lozano *et al.* observed a gradient in pore size, with larger pores of 10 to 250 µm in the interior and smaller ones (1.5 to 5 µm) near the edges [96].

The concentration, composition of the bioinks, and cell interactions influence the size and distribution of pores [9,95,110,126,135]. For instance, higher concentrations of SilMA led to denser structures with smaller pores [95]. Conversely, increasing collagen concentration in bioink has been associated with a gradual increase in internal pore size, a pattern also observed when increasing carboxymethyl cellulose concentration led to larger surface pores [9,98]. Interestingly, Neufeld *et al.* observed that acellular fibrin bioinks had smaller pores compared to cell-laden bioinks, where the addition of tumour cells significantly increased pore sizes, indicating that cellular activity can alter the microstructure of the constructs [126].

The microstructure can also affect the mechanical properties and swelling ratio [116,125]. The water content of the brain has been reported to vary from 68 to 99 in different regions [140]. Thus, hydrogels possess beneficial properties for 3D neural model cultivation due to their high water content [129]. The swelling ratio of the hydrogels can be quantified using the following formula [113]:

$$\text{Swelling rate (\%)} = \frac{W_1 - W_0}{W_0} \times 100\%$$

where W_0 and W_1 are dry and swollen weights, respectively.

Generally, smaller pores correlate with stiffer extracellular matrices [125]. For instance, Pei *et al.* showed higher crosslinking density leads to a denser structure with smaller pores and a higher compressive modulus [9]. Similarly, a higher crosslinking percentage results in a lower porosity, limiting the swelling ratio [95]. A more interconnected pore structure can increase the diffusion potential of the scaffold, which can be tested by diffusing fluorescently labelled molecules within the structure [96,98,125].

The degradation of hydrogels is influenced by their structural properties. Softer and more porous structures tend to degrade faster due to lower polymer concentration [110]. Degradation often consists of an initial rapid phase due to non-crosslinked polymer diffusion, followed by a slower, steady increase over time [110,116]. In disease modeling, the degradation rate of hydrogels should align with the progression of disease. For example, in some Alzheimer's disease models, extracellular Aβ aggregates begin to form after 6 weeks of differentiation, with significant p-tau accumulation observed after 10 weeks [141]. Thus, hydrogel degradation must be carefully timed to match these disease progression milestones.

3.5.1.3. Printability. Printability refers to a bioink ability to be effectively deposited into a 3D structure while maintaining mechanical stability [95]. Kapr *et al.* defined printability as the repeatability of printing with designed measurements without quantifying it, relying on photographic evidence [129]. However, Y. Li *et al.* quantified the printability by measuring the diameter and circularity of embedded-printed fibers, varying printing and extrusion speeds [108]. Similarly, Pei *et al.* examined single-layer grid structures, noting that needle diameter, moving speed, and extrusion rate significantly influenced printability [9]. Needle diameter had the most substantial effect on the line width, whereas moving speed impacted multi-layer printing and ink deposition continuity. Another way of quantifying printability is to measure the ratio of the lattice area to the area of the CAD file, with values close to 1 indicating ideal printability [95]. The standard way of measuring the printability is using the circularity of lattice pores (C):

$$C = \frac{4\pi A}{L^2}$$

where A and L are the area and perimeter of the lattice pores, respectively [142]. Here, the printability (Pr) is defined as:

$$Pr = \frac{\pi}{4C} = \frac{L^2}{16A}$$

with values close to 1 indicating ideal printability, while values < 1 or > 1 indicate inadequate or excessive gelation. However, none of the studies included in this paper performed the test in this manner. This highlights the need for greater standardization and adherence to established methodologies to facilitate easier comparisons across studies.

3.5.2. Material properties – With cells

Cellular characterization is arguably the most important assessment for understanding cell function, viability, and relevance of 3D bioprinted tissues. In particular, the cells must be assessed for their function to ensure that their behaviour within the tissue models represents the intrinsic cellular mechanisms of fundamental biological processes related to cell signalling, interaction, and differentiation. The relevance of the bioprinted tissues must be established to ensure similar mechanical and biochemical relevance to native tissues, which will translate to enhanced clinical success of investigated therapies. Further, ensuring the viability of cells within the tissues allows for an intuitive assessment of the data; cells must be able to survive long enough to exhibit disease pathology and prolonged testing. In addition, *in vivo* biocompatibility and treatment success must be ensured, where appropriate. The lack of characterization of 3D bioprinted materials and constructs has been noted within articles included in our search, especially for functional analysis [129]. We also noted that these characterization techniques varied among similar model types and cell types in addition to their inspected timelines of functionality assessments.

3.5.2.1. Cell viability & proliferation. Typically, determining the cell viability and proliferation can be done using similar reagents given that both rely on the detection of living cells. Cell viability is a simplistic and efficient measurement of the influence that various conditions such as biomaterials, printing parameters, and construct aging, have on the contained cells. For example, when optimizing their bioink, Joung *et al.* first assessed the viability of three different cell types (fibroblasts, hiPSC-derived spinal NPCs, and mouse iPSC-derived OPCs) over 4 days [118]. They saw low viability and opted to print with 50 % Matrigel using cooling systems to maintain printability. They also used viability assessments to see how long the cells could be exposed to air before death, where exposure for 30 min had detrimental effects at low printing volumes.

Most papers used variations of live/dead imaging to investigate cell viability over various time points (Figs. 4 and 5). Live/dead was often conducted using calcein AM to stain live cells and either propidium iodide, ethidium homodimer-III or ethidium homodimer-1 to stain dead cells. The concentrations of each varied across the literature, where it appeared that higher concentrations were typically used for 3D bioprinted materials compared to 2D cultures. Other methods for viability included flow cytometry, often using a Guava ViaCount Reagent or AlamarBlue (AB; Resazurin-based) or CellTiter-Glo (ATP-based detection). Most methods depend on a colorimetric change with living cells and detection and quantification using spectrophotometric approaches. Sulforhodamine B (SRB)-based assay kit, a protein-based detection that can be used for viability [109]. Alamar Blue is typically used for both cell viability and proliferation assessments [2]. Quantification of the cell viability also varied; some papers simply stated that viability 'increased' or 'decreased' without quantification. Cell viability was often normalized using various methods such as normalization to 2D controls (calculated using software in de Melo *et al.* [130]) or correction with pre-

print viability using the following equation [101]:

$$\text{Cell viability} = \frac{\text{cell viability} (\%)}{\text{pre - print cell viability} (\%)} \times 100\%$$

In Abelseth *et al.* [102], viability was calculated as a percentage of the live area determined through ImageJ with the following equation:

$$\% \text{Live Area} = \frac{\text{Live area}}{\text{Live area} + \text{Dead area}} \times 100\%$$

Haring *et al.* measured viability using an AB assay [132]. They calculated viability from % AB reduction using the following equation:

$$\% \text{AB}_{\text{reduced}} = \frac{(\varepsilon_{\text{OX}}\lambda_2)(A\lambda_1) - (\varepsilon_{\text{OX}}\lambda_1)(A\lambda_2)}{(\varepsilon_{\text{RED}}\lambda_1)(A'\lambda_2) - (\varepsilon_{\text{RED}}\lambda_2)(A'\lambda_1)} \times 100$$

where $\varepsilon\lambda_1$ and $\varepsilon\lambda_2$ are molar extinction coefficients of AB at 570 and 600 nm, respectively; ε_{OX} and ε_{RED} represent the oxidized or reduced forms, respectively; $A\lambda_1$ and $A\lambda_2$ are the measured absorbance at 570 and 600 nm, respectively; A' is the absorbance in a negative control. De Melo *et al.* normalized their cell viability to the 2D control and calculated viability using software [130]. If flow cytometry was used, the constructs required degradation. For example, for viability assessments in Sharma *et al.* dissociated constructs using enzymatic (Neural Tissue Dissociation Kit – Postnatal Neurons) and mechanical (gentleMACS™ Dissociator) on days 1 and 7 to obtain single cell suspension for analysis [103]. Viability was determined by adding the dissociated and filtered cells to a plate and using a flow cytometer. MTT assays can also be used for inference of viability, it is discussed in more detail next. While generally, the mechanisms for evaluating viability varied, those that use quantified methods should be explored to compare neural tissue models directly. Flow cytometry offers high-resolution assessments of viability (and other assays) but relies on the dissociation of the tissue constructs to accurately quantify cell viability.

3.5.2.2. Cell proliferation. The ability of cells to proliferate and migrate can display key functions related to tissue development and remodeling [11]. Typically, explicit analysis of cell proliferation was quantified using various methods, such as MTT assay, total DNA content, Cell Counting Kit-8 (CCK8), AlamarBlue assay, PrestoBlue or Resazurin. An MTT assay uses MTT [3-(4,5-dimethylthiazol-2-yl)-2,5-diphenyltetrazolium bromide] to generate a precipitate of formazan relative to active cells. DMSO can be used to dissolve precipitated formazan, and the dissolved analyte is then measured at 555/650 nm on a microplate reader to analyze cell number and proliferation of cells [135]. Other studies assessed proliferation using Alamar Blue assay kits, oftentimes normalizing the values to day 1 using a microplate reader [122]. Lindsay *et al.* determined proliferation through normalized total DNA content of extracted cells from the constructs using Quant-iT PicoGreen dsDNA assay kit [133]. PrestoBlue cell viability indicator was typically employed for proliferation analysis of hNSCs and hiPSCs [98–100]. Cruz *et al.* used a Resazurin assay to identify cell proliferation, which is a redox-based detection assay similar to MTT assays [116]. More indirect analysis of proliferation can evaluate the number of cells or circularity. Cell number can be used to interpret or corroborate other analyses using either fluorescent staining of nuclei (DAPI or Hoechst) or using labelled cells. Circularity is also assessed as a way of interpreting attachment.

Zhou *et al.* used ICC to investigate proliferation through the length of TUJ1+ processes [97]. Constructs were fixed and sectioned for immunohistological analysis (30 µm slices) and analyzed for the length of the TUJ1+ processes, and quantified for cell migration, process density, and bundle width. Grey values were also used to quantify these values. Similarly, Abdelrahman *et al.*, assessed neuron morphology based on neurite number, total length of neurites, length of dominant neurites, and number of branches for both non-DA neurons (TUJ1+ and TH-) and DA neurons (TH+, TUJ1-) [11]. Interestingly, in a co-culture, they looked at ATP release, staining (TUJ1, TH, TBR1) and used Tracker

Green dye to assess the formation of cellular connections between two cells (mouse embryonic cortical and DA neurons) [11].

3.5.2.3. Protein expression. As mentioned, establishing the function of 3D bioprinted models is a principal prerequisite for intuitively interpreting the *in vitro* cellular interactions and translating these functions to *in vivo* conditions. Typical evaluations of cellular function include the analysis of protein expression within the 3D bioprinted models using ICC, flow cytometry, and confocal microscopy, depending on the labelling technique. Quantitation of protein markers can also be done using RT-qPCR.

Understanding the fundamental function of the cells is critical to ensuring the relevance of the 3D bioprinted tissue models. ICC is both qualitative (e.g., identification of the presence or absence of a marker) and quantitative (through the quantification of fluorescence intensity, area, etc.). It should be noted that ICC can also be referred to as immunohistochemistry if tissue constructs are sectioned and analyzed, immunophenotyping or immunofluorescent labelling, among others. Identification of markers using ICC at various stages of cellular development and maturation can be used to interpret the functionality and relevance of the tissue models. Typical markers used for the analysis of hiPSCs, NPCs, astrocytes, oligodendrocytes, and neurons are outlined in Fig. 7.

Identification of cell markers can be used for the assessment of purity of cells. For example, Gu *et al.* confirmed both the pluripotency of cells within constructs in the absence of differentiating molecules in the media and subsequently confirmed neuronal differentiation after the inclusion of small molecules (StemPro, N2, BDNF) [99]. In another work by Gu *et al.*, pluripotency was confirmed after 10 days of culture within their 3D bioprinted constructs using flow cytometry and immunophenotyping with confocal microscopy for the pluripotent markers OCT4, SOX2, TRA-1-60, and SSEA4 [99]. They also used a combination of ICC and RT-qPCR to identify mature neuron and glial markers within their differentiating cells; neural subtypes of GABA (gamma-aminobutyric acid), NKX2-1, PET1 (serotonergic marker), and OLIGO2 (oligodendrocyte lineage transcription factor 2), Nestin, βIII tubulin, and GFAP were identified with a simultaneous downregulation of pluripotency markers (OCT4, NANOG, and SOX2). These investigations are essential to ensure that the models demonstrate representative behaviour for the designated cell and/or tissue environments. Relevant to tissue engineering, if cells are still in a pluripotent state, heterogeneous constructs can be formed which may impede function.

Given the sensitivity of RT-qPCR, markers identified using ICC or similar can be confirmed quantitatively with high confidence or can identify markers that cannot be easily visualized. For example, this applies to bioinks that use fibrinogen, which exhibits autofluorescence and obscures low expression levels, where RT-qPCR sensitivity can circumvent this. However, the caveat of using RT-qPCR is that this technique relies on the extraction and quantification of ribonucleic acid (RNA) or messenger RNA (mRNA), which may not directly reflect the protein expression *in vitro*. Therefore, corroborating the findings between ICC and RT-qPCR is suggested, which has been typically done in the literature.

3.5.2.4. Calcium imaging. In addition to protein expression, establishing fundamental functions of cell types, especially in neurons, is essential. Calcium imaging is used to explore baseline spontaneous or induced calcium release, which uses a marker-based assay to excite cells and subsequently quantify the calcium flux [128]. This method typically detects calcium ions (Ca^{2+}) within the networks, indicating spontaneous neural signalling and function [65]. Most often, Fluo-4 AM was used for baseline calcium imaging. Gu *et al.* used Fluo-4 to demonstrate spontaneous calcium spikes in their 3D bioprinted differentiated hNSCs and also used bicuculline to induce activity [98]. It was unclear on what day this was done, although it is assumed to be at least 10 days after

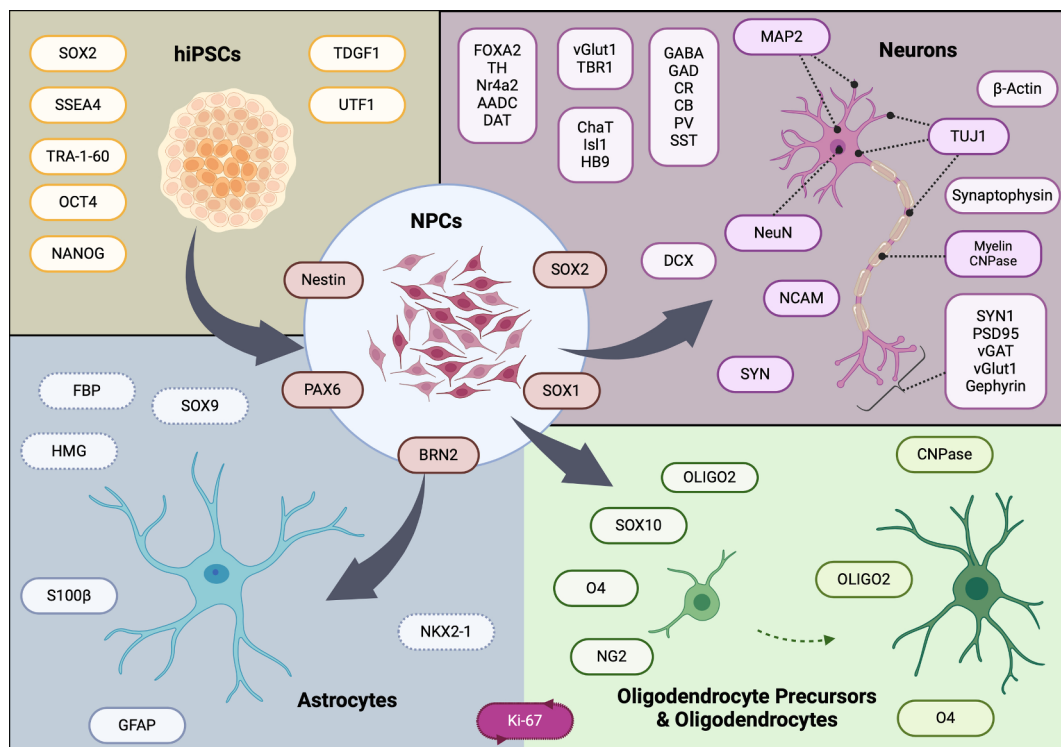


Fig. 7. Typical cellular markers investigated for various cell types including human induced pluripotent stem cells (hiPSCs), neural progenitor cells (NPCs), astrocytes, oligodendrocytes (and precursors) and neurons. Markers with dashed border indicate reported astrocyte markers outside of systematic review; grouped markers are based on specific neuron sub-type. The marker Ki-67 was reported as a proliferation marker at multiple stages of cell growth. Created with BioRender.com.

differentiation (24 days post-printing). In another study, Gu *et al.* again used Fluo-4 to conduct live calcium imaging on the calcium influx and cell migration after 40 days of bioprinting their iPSC-containing constructs [99]. Further, they expended bicuculline to confirm the function of intracellular calcium of their suspected neuron type, GABAergic neurons.

Induced activity can be measured using KCl, bicuculline, or neurotransmitters such as acetylcholine or glutamate. Bicuculline is an antagonist of GABA(A) receptor which is added to induce release of the intracellular calcium [100]. KCl can be used to selectively depolarize neurons leading to the release of relevant neurotransmitters such as glutamate in the case of cortical neurons [14]. This method works particularly well when astrocytes are co-cultured since the KCl does not influence these cell types, allowing for investigation of neural subtypes [14]. While not done in their study, Kapri *et al.* discuss that analysis of sodium signals can probe for glutamate transporters, which are more expressed by astrocytes [129]. In addition to assessing NPC basal neural activity, Joung *et al.* combined KCl and glutamate to assess doped response [118]. Early detection of functionality can be done in as little as four days, where Zhou *et al.* detected spontaneous Ca^{2+} oscillations 4 days post printing, and this response strengthened with increased days in culture [97]. At 65 days post-printing, exposure to the constructs with KCl triggered rapid Ca^{2+} transients, suggesting functional tissues [97].

It showed that action potentials could induce voltage-gated sodium and potassium channels and that the resting membrane potentials were similar to endogenous dopamine neurons but showed various stages of development and differentiation. Yan *et al.* used high and low potassium Tyrode's solution to conduct calcium and glutamate imaging and assessed fluorescence change was defined using the following equation:

$$\Delta \frac{F}{F(t)} = \frac{(F_0 - F(t))}{F_0}$$

where F_0 is the average fluorescence intensity of the imaging area for

samples in the low KCl solution, and $F(t)$ is the fluorescence intensity at a given time [14]. The fluorescence change was normalized to the control group. In addition, cells were infected with a glutamate-sensing fluorescent reporter (iGluSnFR), and calcium and glutamate imaging within varying regions of interest were conducted. The signals increased from 2 to 4 weeks, indicating that astrocytes can uptake glutamate release from neurons. This live glutamate imaging allowed for the assessment of glutamate recycling, a key function of astrocytes.

These characterizations highlight the important trend in neural tissue engineering to design both mechanically relevant and functional tissues, and the incorporation of methods to evaluate the chemically relevant functions of *in vivo* tissues.

3.5.2.5. Metabolic activity & electrophysiology. Metabolic activity can also provide key insight on functionality using assays that probe membrane potential, where electrophysiological analysis can be measured using voltage-sensitive dye, MEAs, and other direct or indirect assays. CellTiter-Glo® [11] and CellTiter Blue [133] have been used to assess metabolic activity. These assay measure ATP to indicate metabolic activity and can be done in as little as three days [11]. In Y.-C. E. Li *et al.*, metabolic activity was assessed using Presto Blue Reagent for both neural lineages and astrocytes [108]. In addition, they intuitively investigated the metabolic interactions between neurons and astrocytes in their co-culture by investigating the glutamate-glutamine pathway. They showed that neurons by themselves had higher levels of glutamate released compared to the neuron-astrocyte co-culture or the astrocyte culture. Similar work was done by Perez *et al.* where dopamine release was detected using ELISA after 12 days [105].

While not in their bioprinted constructs, Abdelrahman *et al.* assessed the metabolic activity of co-cultured mouse embryonic cortical and ventral midbrain DA neurons by assessing the amount of ATP release, in addition to staining for TUJ1, TH, and TBR1 to assess connections between TH+ and TBR1+ neurons [11]. When treated with 6-OHDA, the

% ATP release and the number of TH+ cells decreased, indicative of neuronal function for DA neurons in PD. In addition, MEAs were used to capture the extracellular activity of their networks. By printing directly on MEAs, it was demonstrated that NPC spheres embedded and differentiated contain electrical activity after 21 days in culture. Analysis using MEAs can be used to assess the efficiency of 3D bioprinted models to recapitulate *in vivo* environments [11], and provide functional readouts beyond calcium imaging [129].

Electrophysiology was assessed in Perez *et al.* using voltage-sensitive dye. They used the following equation to determine the membrane potential [105]:

$$\Delta E = \frac{RT}{zF} \ln \left(\frac{1}{\frac{\Delta F}{F_0} + 1} \right)$$

where R = gas constant (8.314 J/Kmol), T = temperature (Kelvin), F = Faraday's constant (As/mol), z = apparent charge of external dye, $\Delta F = F - F_0$, where F = the construct and cells reading, and F_0 is the background fluorescence of the construct only.

Restan Perez *et al.* used the FLIPR Membrane Potential Assay Kit Blue (voltage-sensitive dye), followed by KCl addition to assess dopaminergic neuron electrical properties since the 3D constructs could not be patch-clamped [104]. Importantly, in this work it was shown that compared to 2D culture, the 3D environment enabled the cells to become more electrophysiologically mature; these systems were shown to be relatively adolescent from native tissues but confirmed doped response to KCl [104]. Similarly, Scarian *et al.* noted that patch clamps and MEAs could not be used due to the hydrating bioink forming a film around the cells which impedes connection [111]. Instead, they measured electrophysiological characteristics using c-fos, an indirect marker of neuronal activity during action potential firing over 14 days [111]. The cells were also treated with KCl since NSC34 cells (motor neuron-like cells) do not have spontaneous electrical activity; however, their bioink (Cellink bioink) had background fluorescence with c-fos labelling, but induction with KCl did show statistically increased firing capacity.

Some studies could use whole-cell patch clamps, such as those printed into SHAPE support baths [65] or thin layered constructs [14]. Kajtez *et al.* was able to use whole-cell patch clamps to record single-cell electrophysiology using a microelectrode to target cells labelled with synapsin-GFP and neuronal morphology [65]. After 21 days in their triculture, Yan *et al.* measured the spontaneous action potentials of glutamate cortical cells within the bioprinted models [14]. They noted that the spontaneous action potentials increased both in the percentage of cortical neurons with these features and the frequency over time, and these activities were enhanced when GABAergic and glutamatergic neurons were co-cultured. Additionally, whole-cell patch clamping was used to monitor the cycling Na^+ (in) and K^+ (out), excitatory postsynaptic currents (EPSCs) and inhibitory postsynaptic currents (IPSCs). In addition, bicuculline inhibited the spontaneous IPSC activity, indicating functional maturation of the GABA neurons. The relatively small layer height (50 μm) of their constructs enabled the use of whole cell patch clamping for these analyses.

X. Wang *et al.* used a sandwich enzyme immunoassay kit to quantify VEGFA and bFGF secreted by the cells, and the concentration was measured based on OD values of a standard [122]. In the work of Matthiesen *et al.*, it was noted that viability can be measured using AlamarBlue, and the % reduction of AB is indicative of metabolic activity [112]. An innovative way to look at expression and function was shown in Sunil *et al.* Here, surface expression of calreticulin and high-mobility group box 1 (HMGB1) release from the GBMs was assessed [127]. In this way, they wanted to see if the BIONs could trigger ICD – an essential immune response. In the highest activated group (BIONs + light), there was a significant increase in HMGB1 release and calreticulin. They also analyzed mitochondrial membrane potential ($\Delta\psi_m$) to indicate apoptosis. This was done using a JC-1 assay and Annexin-V/

FITC to indicate apoptosis.

Methods related to electrophysiology such as whole cell patch clamping and MEAs lend superior functional analysis of fabricated neural tissues. Going forward, a way of performing these analyses should be considered, given their inherent value. A way around the limitation of hydrogels impeding electrical signals was shown by Kapr *et al.* by printing constructs directly on MEAs [129]. While this may not be feasible for sterility reasons on all constructs, printing select constructs for MEA analysis could be of benefit and can circumvent the current caveat of hydrogels. Additionally, the incorporation of biocompatible and inert polymers that allow for conductive analysis may also be practical.

3.6. Applications of 3D bioprinting

3.6.1. Disease modeling

Current cell culture and 3D bioprinting technologies allow us to successfully generate various brain-associated cell types and co-culture them in specific hydrogel formulations to obtain tissues that resemble aspects of the human brain [115]. Furthermore, differentiating pluripotent stem cells into NSCs, neurons and glia within the hydrogel scaffold provides an opportunity to study brain development and understand the processes that give rise to neurodevelopmental disorders, a window of development that otherwise is very difficult to capture in human-specific systems [116].

Disrupted neural circuits ultimately leading to neurodegeneration are a hallmark of diseases like Alzheimer's and Parkinson's disease, epilepsy, schizophrenia, autism spectrum disorder, and multiple sclerosis [10,107]. Neural circuits are often studied in 2D cell cultures, but it cannot be understated that neural circuits are in fact complex, three-dimensional structures in which diverse cell–cell interactions occur, and this 3D environment is essential for accuracy in circuit function, connectivity, and response to stimuli [14]. Moreover, the presence of ECM is crucial for neural circuit formation as it provides structural support, regulates cell adhesion and migration, and influences synapse formation and plasticity, thereby guiding the development and connectivity of neural networks [100]. Yan *et al.* utilized an innovative approach to producing functionalized neural tissues in which multilayered constructs were established by horizontal stacking of layers of glutamatergic neurons, GABAergic neurons and astrocytes [14]. These heterogeneous tissues facilitated synapse formation between these diverse cell types and improved modeling of neural circuits. Notably, they found that the formation of functional networks between cortical and striatal tissues is similar to observations *in vivo* where striatal neurons project their axons towards cortical neurons. This model was further applied to study Alexander disease, a neurodegenerative disease where the accumulation of GFAP within astrocytes disrupts their normal function, leading to impaired neuronal support, altered neurotransmitter regulation, and a breakdown in neural circuitry. The disease model containing mutant astrocytes (which carried an R88C mutation) had significantly fewer synapses than controls as the mutated astrocytes were less supportive for synaptogenesis. This approach therefore has the potential to provide detailed models of various neurological disorders that involve neural network dysfunction.

Neural death in PD, characterized by progressive degeneration of DA neurons, is thought to involve oxidative stress and neuroinflammation, making it important to establish a model that can capture neuroimmune interactions. Rueda-Gensini *et al.* [10] therefore modeled PD incorporating monocytes, macrophages and astrocytes with human mid-brain DA neurons in an electroconductive scaffold. In this model, key pathologies of PD were replicated including α -sync aggregation, mitochondrial dysfunction and oxidative stress. These types of models that feature scaffolds with improved relevance to human brain tissue, and incorporate multiple cell types, are invaluable for studying complex disorders. While the apparent cause of disease in PD is the loss of DA neurons, it is the integration of all contributing factors that leads to

neuronal loss and therefore co-culturing cells together to study these diseases is of paramount importance. Diseases that affect motor neurons, such as ALS, have been modeled by differentiating pluripotent stem cells to motor neurons *in vitro* [111]. In addition to NSCs, Perez *et al.* [105] employed mesenchymal stem cells to create neural tissues, offering another accessible strategy for generating patient-specific tissues.

Among disorders of the brain, GBM stands out as particularly lethal and incurable, with a median survival of just 15 months, and represents one of the most malignant forms of brain cancer [143]. GBM exists within a complex and hostile milieu where altered ECM, hypoxia, cellular heterogeneity and drug efflux mechanisms hamper the effectiveness of drug treatments. Thus, GBM-targeted drugs typically fail in clinical trials [144]. 3D bioprinting technology has been employed to help overcome this challenge due to its efficient spatial control, ability to use biomaterials that mimic human brain ECM, and capability to culture multiple cell types in an organized manner [122]. Neufeld *et al.* proposed an incredible approach to not only model GBM neural cells in 3D but to also introduce vasculature into the engineered tumours by printing a combination of two bioinks, specifically a tumour-specific ink and a vascular-specific ink [126]. This group used a fugitive bioink to create temporary channels within the tissue construct that can be removed by pumping fibronectin using a peristaltic pump, leaving behind a hollow vascular network surrounded by 3D-bioprinted neural tissue. The hollow channels are later flooded with endothelial cells, pericytes, astrocytes and microglia in an effort to model the BBB. Impressively, growth of GBM cells in this model was found to be comparable to *in vivo* tumour growth. A similar GBM model was created by Wang *et al.* where they printed hydrogels loaded with glioblastoma (U118) with an inner core of HUVEC cells in the form of fibers using a coaxial printer [122]. This model effectively replicates the vascularization ability of GBM, making it an ideal platform for discovering drugs to control angiogenesis within GBM tumours, which is one of the main biological aspects of interest to control tumour growth [145].

Since tumour tissue naturally varies in stiffness, Tang *et al.* created a GBM model with varying stiffness and found that the drug temozolamide exhibited differential responses [125]. The drug was less effective in stiffer tissue regions, corresponding to the tumour mass, and more effective in softer areas which are associated with active cell differentiation. Such models are valuable in studying the response of drugs within defined tumour microenvironments and help in developing more targeted therapies that account for the physical heterogeneity of tumours, potentially leading to more effective treatments. Smits *et al.* showed that GBM cannot be accurately modeled in 2D, rather 3D models of GBM present as spheroids within hydrogel [124]. They also showed that these spheroids, which indicate tumour growth can be controlled by N-cadherin antagonist (Compound 15), N-cadherin over expression is associated with gliomas. Using 3D bioprinting the native tumour microenvironment can be replicated making it an excellent platform for assessing the clinical potential of new anticancer agents.

3.6.2. Drug discovery

Since 3D bioprinting provides more predictive and accurate models of brain tissue over 2D models, 3D approaches should also provide optimal strategies for preclinical testing of drug efficacy and toxicity [126]. Additionally, 3D bioprinted models can be customized to include patient-specific cells, enabling personalized medicine approaches where drug responses can be tested on tissue engineered from a patient's own cells [107,111]. 3D bioprinting can also be coupled with high throughput screening to test large libraries of compounds for restoration of cell and tissue phenotypes as potential drug candidates [146]. This way it can also accelerate the drug development process. Aligning with ethical considerations, 3D bioprinted models also reduce the reliance on animal testing.

Of all 46 studies included in the review, most focus on the development and validation of the bioprinted constructs, with few exploring the efficacy of therapeutic agents within these complex systems. C. Lee

et al. aimed to test whether a 3D-printed scaffold would respond uniquely to a GBM-reprogramming cocktail (FICBD; Forskolin, ISX9, CHIR99021, BET 151, and DAPT), previously shown to convert GBM cells into neurons in 2D [123]. While the cells treated within the 3D scaffold showed reduced proliferation, they did not exhibit the expected neurite elongation. Additionally, key markers like TUJ1, DCX, and Nestin did not show significant changes compared to untreated scaffolds which signifies a resistance of cells towards drugs that is only observed in 3D environments.

As mentioned previously, small molecule compounds and other potential drugs can have different effects in 2D as compared to 3D environments. In a model of GBM, P-selectin inhibitor SELPi, that controls growth of GBM had no effect in 2D cultures of human GB cells (PD-GB4) [126]. However, SELPi significantly inhibited PD-GB4 cell proliferation in 3D cultures, an effect also observed *in vivo* in GB-bearing mice, likely due to differing P-selectin expression in 3D compared to 2D cultures. Similar results were seen in additional GB cell types, indicating that the 3D model better reflects the tumour's response to SELPi treatment. This is one example that demonstrates the significance of using 3D models for drug testing [126]. Similarly, TMZ, a chemotherapy drug for glioblastoma, showed similar IC₅₀ values across different patient-derived cells in 2D cultures, but varied significantly in 3D models [126].

These findings suggest that 3D scaffolds provide a more relevant cellular environment to *in vivo*, they may offer valuable insights for optimizing new drugs before moving on to animal trials.

3.6.3. Tissue regeneration

The studies on peripheral nerve regeneration were excluded from the review as the main focus of the review is neural brain tissue, however, their relevance to clinical research is worth mentioning.

Outside of modeling development and disease pathogenesis, another important application of 3D bioprinting is the mounting effort to generate functional neural tissue. Among those, nerve conduits hold significant importance as peripheral nerve injuries are difficult to treat with medical and physiotherapy procedures [147]. It is complex as not only is the growth of functional neuronal connections important, but proper myelination is also essential for the rapid transmission of nerve impulses [135]. Damage to myelin sheaths leads to slower signal transmission and reduced nerve function. Restoration of myelin, which is produced by Schwann cells, is a prime requirement of nerve regeneration [148].

By enabling the precise fabrication of biomimetic scaffolds that support the growth and differentiation of neural cells, 3D bioprinting offers a promising avenue for nerve tissue regeneration, facilitating the establishment of a neural relay to repair the damaged site. It holds the potential to overcome the challenges of traditional nerve repair methods by facilitating the formation of functional neural networks and promoting myelination have employed various strategies for regeneration of nerve implants [122,148,149]. More innovative strategies have been employed for spinal cord regeneration, a process that requires the precise establishment of axon connections within its highly organized structure, making it challenging to recapitulate *in vitro* [118]. As the field advances, 3D bioprinting could also revolutionize the treatment of nerve injuries, providing personalized therapeutic options for patients.

4. Conclusion and future Outlooks

In this review, we systematically examined the most recent literature in the last ten years to compare neural models that have been generated using 3D bioprinting. In particular, we emphasized the analysis of neural tissue models of the brain and aimed to investigate the potential drug screening applications. In the systematic review, we found that neural tissues were designed using various bioinks, cell types, and for a host of applications relating to modeling the brain or spinal cord exclusively or were generated for more broad applications in modeling the CNS, or tumour conditions such as glioblastomas.

4.1. Improving reproducibility and transparency

Based on this review, we underscore that the transparency of methodologies used in research should be conducted. While it appears that strides have been made over the years to report comprehensive and straightforward methods, we encourage transparency and explanation in methodology – especially related to characterization. For example, the literature should aim to provide comprehensive explanations of frequency (e.g., on what days) and conditions (e.g., polymer variations, media, cells, etc.) of characterization techniques. This truancy can still be found in present-day research and should be rectified in future works. While we appreciate the proprietary nature of intellectual property in biomaterial design, encouraging methodology transparency will only advance the newly designed neural models and allow for adequate comparisons between 3D bioengineered neural tissues.

4.2. Standardizing material characterization

The heterogeneities in material characterization, both relating to mechanical and cellular domains, are quite evident (Tables 2–5, Table S3), but this appears to be trending towards more sophisticated characterization techniques that aim to understand the relevance of the neural tissue models. There was a clear lack of studies in our search that investigated effective drug screening applications in conjunction with a comprehensive evaluation of neural tissue models' physical and biochemical performance. This is a critical area of neural tissue engineering that needs to be addressed to strive toward accurate tissue models that can effectively recapitulate the spatiotemporal and chemical-physical networks found in neural tissues. Understanding the mechanical properties through printability testing, rheological/compression testing, degradation, and porosity assessments is suggested. Further, cellular characterization of viability and proliferation, protein expression, inflammatory state, and evaluating the electrophysiology is necessary. Recent literature has suggested the use of characterization techniques for drug screening applications be conducted related to dysfunctions in a variety of physiological functions such as: proteostasis, metabolic pathways, oxidative stress, immune activation, and synaptic loss [150]. In addition, models should aim to incorporate multiple relevant cell types into their tissues to truly capture the complexity and fundamental function of the human brain.

4.3. Translational relevance to drug discovery

3D bioprinted tissue models can be used to improve pre-clinical disease modeling compared to traditional 2D and animal models, which can play a pivotal role in drug screening applications [48,151]. 3D bioprinting can generate architecturally relevant models that can be effectively used for drug screening [150]. Incorporating reproducible human cell-based models can identify poor candidate drugs early in the drug development pipeline using high-throughput screening (HTS), before expensive and time-consuming clinical testing can take place [146]. Further, in addition to treatment efficacy, these models can elucidate important features such as cytotoxicity, and the influence on cell proliferation, morphology, and metabolic pathways, among others.

An important feature of 3D bioprinting is that it can be easily integrated with precision medicine, a technique that integrates personalized approaches to disease treatment. Patient-specific models account for underlying genetic effects and have the potential to be rapidly fabricated, allowing for efficient HTS of multiple drugs for their individual efficacy [152]. In practice, it can be time-consuming to generate individual cell lines, but can greatly enhance patient response to drugs in multiple disease-based scenarios and can alleviate some of the disadvantages of currently used xenografts. Patient-derived xenografts within animal models are time-consuming, have limited drug testing capacities, and often occur in immunodeficient mice, limiting the replication of the disease microenvironment [152].

These challenges have the unique opportunity to strengthen collaborations at multiple levels of research and practice – where academia, industry and regulatory bodies can play critical roles in bridging the gap from research to clinical success. Industry and academic research groups can have reciprocal relationships by sharing insights on drug testing needs and offering mutual feedback on drug performance. Additionally, governing bodies can support these relationships through funding [153,154]. This highlights the importance of collaboration and fosters successful environments for viable drug identification. For example, academic settings typically lack the expertise in regulatory factors for drug testing [154] and have limited resources for large scale HTS for multiple diseases, patients, etc. Collaboration with regulatory and industry partners (who often have more resources) can bridge this gap and strengthen the translation of scientific research to clinical settings [153,154].

4.4. Challenges and future perspectives

While the future of regenerative medicine and disease therapy can be advanced with 3D bioprinting technologies, these avenues do not come without challenges. An important concept in drug screening is the ability to cross the BBB, which is a current limit in 3D tissue models. The BBB is a crucially relevant microstructure in brain models, especially when modelling neurodegenerative disorders and evaluating drug efficacy [155,156]. Simplification in these BBB models can be effective to assess cell migration and molecule permeability, where *in vitro* models commonly use TransWell inserts in combination with monolayers of BMECs or Madin-Darby Canine Kidney epithelial cells (MDCKs) [156]. The challenges associated with accurate modelling have been effectively outlined in a review by Linville and Searson [156]. One of the challenges highlighted is that approaches for achieving multiscale and hierarchical models should be explored [156]. As mentioned previously, chaotic bioprinting may provide a sophisticated solution to accomplish this hierarchical patterning for improving BBB-containing 3D models [75]. Moreover, advances in DLP and extrusion-based bioprinting have allowed for the creation of BBB models by incorporating endothelial cells, pericytes, astrocytes, and dynamic flow systems to replicate BBB structure and function [157–159]. However, the resolution of these systems is still insufficient to print small capillary structures, with lumen diameters in models being larger than actual capillaries. Although two-photon printing offers higher resolution, its slow printing speed makes it unsuitable for large-scale applications [160]. Nonetheless, the integration of bioactive hydrogels, perfusion systems, and advanced bioinformatics for characterization is pushing the field forward, enabling more accurate and relevant BBB models for drug screening and disease modelling [159].

Emerging research in the last few years has demonstrated the potential for advanced characterization techniques using bioinformatics to reveal underlying changes in cellular function, proliferation capabilities, among others. Further, integrating machine learning and artificial intelligence (AI) platforms within 3D bioprinting workflows has the potential to strongly enhance the optimization, relevance and functionality of these models [161]. Not only will these advancing techniques be useful for understanding disease pathology in a new light, but will offer novel tools to characterize preclinical models for their relevance.

4.5. Concluding Remarks

Overall, recent work has shown how bioprinted neural tissues can be produced with complex structures and replicate relevant neural phenotypes – making it a powerful tool for neuroscience and drug discovery. An intriguing find was that in the most recent literature evaluated, the design of brain tissue models that recapitulate *in vivo* functions is still emphasized as a critical need in biomedical research. We currently face the challenge of mimicking the functional complexity and structural layered hierarchy of the human brain, despite progressing technologies.

When reviewed systematically, we note that the trend of bio-manufacturing 3D bioprinted neural models is progressing towards the design of more representative environments, that include the crucial components of the ECM [14,65], in addition to the investigation of mechanical relevance and its influence on function [108,115,125].

These trends should be adopted as the standard for assessing the relevance of 3D bioprinted neural models going forward. Constructs should mimic the mechanical properties found naturally in the brain to encourage appropriate cellular function. Importantly, research in biomaterial design for 3D bioprinted tissue models should also focus on assessing the translational relevance to *in vivo* conditions, where possible, including basic cell function and behaviour. Addressing these clear gaps in 3D tissue engineering will be beneficial to advance the design, analysis, and versatility of these models to answer complex questions relating to disease pathology and treatment in the future.

Acknowledgments

This work was supported by multiple funding agencies: the Micheal Smith Health Research B.C./Canadians for Leading Edge Alzheimer Research (CLEAR) to A.O. (RT-2023-3070), the Canadian Biomaterials Society Visiting Scholar Award (B.B.), NSERC Discovery Grants to S.M. W. (RGPIN-2017-04044) and L.M.J. (JULIAN, L-RGPIN-03965), the Canadian Research Chairs program to L.M.J. (950-233179), the Canadian Institutes of Health Research Project Grant to S.M.W. (Project Grant: 460840), the Michael Smith Health Research B.C. to S.M.W. (I2C-2019-2160) and L.M.J. (SCH-2021-1907), the Pacific Parkinson's Research Institute to S.M.W. (I2C-2019-2160), Fulbright Canada - MITACS Globalink program (K.O.), and a Cancer Research Society operating grant to L.M.J. (JULIAN, L-CRS 25551).

Appendix A. Supplementary material

Supplementary data to this article can be found online at <https://doi.org/10.1016/j.addrev.2025.115524>.

Data availability

Data will be made available on request.

References

- [1] L. de la Vega, C. Lee, R. Sharma, M. Amereh, S.M. Willerth, 3D bioprinting models of neural tissues: the current state of the field and future directions, *Brain Res. Bull.* 2019 (150) (2019) 240–249, <https://doi.org/10.1016/j.brainresbull.2019.06.007>.
- [2] N. Gomila Pelegri, A.M. Stanczak, A.L. Bottomley, B.K. Milthorpe, C.A. Gorrie, M. P. Padula, J. Santos, Adipose-derived stem cells spontaneously express neural markers when grown in a PEG-based 3D matrix, *Int. J. Mol. Sci.* 24 (15) (2023), <https://doi.org/10.3390/IJMS241512139>.
- [3] J. Wang, X. Kong, Q. Li, C. Li, H. Yu, G. Ning, Z. Xiang, Y. Liu, S. Feng, The spatial arrangement of cells in a 3D-Printed biomimetic spinal cord promotes directional differentiation and repairs the motor function after spinal cord injury, *Biofabrication* 13 (4) (2021), <https://doi.org/10.1088/1758-5090/AC0C5F>.
- [4] D.S. Bassett, M.S. Gazzaniga, Understanding complexity in the human brain, *Trends Cognitive Sci* 15 (2011) 200–209, <https://doi.org/10.1016/j.tics.2011.03.006>.
- [5] S. Bagchi, T. Chhibber, B. Lahooti, A. Verma, V. Borse, R.D. Jayant, In-Vitro Blood-Brain Barrier Models for Drug Screening and Permeation Studies: An Overview, *Drug Des Devel Ther.* 13 (2019) 3591–3605, <https://doi.org/10.2147/DDDT.S218708>.
- [6] H.T. Hogberg, J. Bressler, K.M. Christian, G. Harris, G. Makri, C. O'Driscoll, D. Pamies, L. Smirnova, Z. Wen, T. Hartung, Toward a 3D model of human brain development for studying gene/environment interactions, *Stem Cell Res Ther.* 4 Suppl 1(Suppl 1) (2013) S4, <https://doi.org/10.1186/scrt365>.
- [7] P. Zhuang, A.X. Sun, J. An, C.K. Chua, S.Y. Chew, 3D neural tissue models: from spheroids to bioprinting, *Biomaterials* 154 (2018) 113–133, <https://doi.org/10.1016/j.biomaterials.2017.10.002>.
- [8] D. Anton, H. Burkel, E. Josset, G. Noel, Three-Dimensional Cell Culture: A Breakthrough *In Vivo*, *Int. J. Mol. Sci.* (2015) 5517–5527, <https://doi.org/10.3390/ijms16035517>.
- [9] N. Pei, Z. Hao, S. Wang, B. Pan, A. Fang, J. Kang, D. Li, J. He, L. Wang, 3D printing of layered gradient pore structure of brain-like tissue, *Int. J. Bioprint.* 7 (3) (2021) 71–85, <https://doi.org/10.18063/IJB.V7I3.359>.
- [10] L. Rueda-Gensini, J.A. Serna, D. Rubio, J.C. Orozco, N.I. Bolaños, J.C. Cruz, C. Muñoz-Camargo, Three-dimensional neuroimmune co-culture system for modeling Parkinson's disease microenvironments *in vitro*, *Biofabrication* 15 (4) (2023), <https://doi.org/10.1088/1758-5090/ace21b>.
- [11] S. Abdelrahman, W.F. Alsanie, Z.N. Khan, H.I. Albalawi, R.I. Felimban, M. Moretti, N. Steiner, A.G. Chaudhary, C.A.E. Hauser, A Parkinson's disease model composed of 3D bioprinted dopaminergic neurons within a biomimetic peptide scaffold, *Biofabrication* 14 (4) (2022), <https://doi.org/10.1088/1758-5090/AC7EEC>.
- [12] K. Grenier, J. Kao, P. Diamandis, Three-dimensional modeling of human neurodegeneration: brain organoids coming of age, *Mol. Psychiatry* 25 (2) (2020) 254–274, <https://doi.org/10.1038/s41380-019-0500-7>.
- [13] W.K. Raja, A.E. Mungenast, Y.T. Lin, T. Ko, F. Abdurrob, J. Seo, L.H. Tsai, Self-Organizing 3D human neural tissue derived from induced pluripotent stem cells recapitulate Alzheimer's disease phenotypes, *PLoS One* 11 (9) (2016), <https://doi.org/10.1371/journal.pone.0161969>.
- [14] Y. Yan, X. Li, Y. Gao, S. Mathivanan, L. Kong, Y. Tao, Y. Dong, X. Li, A. Bhattacharyya, X. Zhao, S.C. Zhang, 3D Bioprinting of human neural tissues with functional connectivity, *Cell Stem Cell* 31 (2) (2024) 260–274, <https://doi.org/10.1016/j.stem.2023.12.009>.
- [15] J.A. Garcia-Leon, L. Caceres-Palomero, E. Sanchez-Mejias, M. Mejias-Ortega, C. Nuñez-Díaz, J.J. Fernandez-Valenzuela, R. Sanchez-Varo, J.C. Davila, J. Vitorica, A. Gutierrez, Human pluripotent stem cell-derived neural cells as a relevant platform for drug screening in Alzheimer's disease, *Int. J. Mol. Sci.* 21 (18) (2020) 6867, <https://doi.org/10.3390/ijms21186867>.
- [16] J.C. Park, S.Y. Jang, D. Lee, J. Lee, U. Kang, H. Chang, H.J. Kim, S.H. Han, J. Seo, M. Choi, D.Y. Lee, M.S. Byun, D. Yi, K.H. Cho, I. Mook-Jung, A logical network-based drug-screening platform for Alzheimer's disease representing pathological features of human brain organoids, *Nat. Commun.* 12 (1) (2021) 280, <https://doi.org/10.1038/s41467-020-20440-5>.
- [17] S.S. Kwak, K.J. Washicosky, E. Brand, D. von Maydell, J. Aronson, S. Kim, D. E. Capen, M. Cetinbas, R. Sadreyev, S. Ning, E. Bylykbashi, W. Xia, S.L. Wagner, S. H. Choi, R.E. Tanzi, D.Y. Kim, Amyloid-B42/40 ratio drives tau pathology in 3D human neural cell culture models of Alzheimer's disease, *Nat. Commun.* 11 (1) (2020) 1377, <https://doi.org/10.1038/s41467-020-15120-3>.
- [18] K. Karzyński, K. Kosowska, F. Ambrożkiewicz, A. Berman, J. Cichoń, M. Klak, M. Serwańska-Swistek, M. Wszola, Use of 3D bioprinting in biomedical engineering for clinical application, *Medical Studies/studia Medyczne* 34 (1) (2018) 93–97, <https://doi.org/10.5114/ms.2018.74827>.
- [19] A. Arslan-Yıldız, R. El Assal, P. Chen, S. Guven, F. Inci, U. Demirci, Towards artificial tissue models: past, present, and future of 3D bioprinting, *Biofabrication* 8 (1) (2016) 014103, <https://doi.org/10.1088/1758-5090/8/1/014103>.
- [20] Y.S. Zhang, M. Duchamp, R. Oklu, L.W. Ellisen, R. Langer, A. Khademhosseini, Bioprinting the cancer microenvironment, *ACS Biomater. Sci. Eng.* 2 (10) (2016) 1710–1721, <https://doi.org/10.1021/acsbiomaterials.6b00246>.
- [21] C. Mazzaglia, Y. Sheng, L.N. Rodrigues, I.M. Lei, J.D. Shields, Y.Y.S. Huang, Deployable extrusion bioprinting of compartmentalized tumoroids with cancer associated fibroblasts for immune cell interactions, *Biofabrication* 15 (2) (2023) 25005, <https://doi.org/10.1088/1758-5090/acb1db>.
- [22] I.T. Ozbolat, M. Hospidou, Current advances and future perspectives in extrusion-based bioprinting, *Biomaterials* 76 (2016) 321–343, <https://doi.org/10.1016/j.biomaterials.2015.10.076>.
- [23] P. Zhuang, W.L. Ng, J. An, C.K. Chua, L.P. Tan, Layer-by-layer ultraviolet assisted extrusion-based (UAE) bioprinting of hydrogel constructs with high aspect ratio for soft tissue engineering applications, *PLoS One* 14 (6) (2019) e0216776, <https://doi.org/10.1371/journal.pone.0216776>.
- [24] K. Ling, G. Huang, J. Liu, X. Zhang, Y. Ma, T. Lu, F. Xu, Bioprinting-based high-throughput fabrication of three-dimensional MCF-7 human breast cancer cellular spheroids, *Engineering* 1 (2) (2015) 269–274, <https://doi.org/10.15302/J-ENG-2015062>.
- [25] A. Shafiee, A. Atala, Printing technologies for medical applications, *Trends Mol. Med.* 22 (3) (2016) 254–265, <https://doi.org/10.1016/j.molmed.2016.01.003>.
- [26] J.H. Park, J. Jang, J.-S. Lee, D.-W. Cho, Three-dimensional printing of tissue/organ analogues containing living cells, *Ann. Biomed. Eng.* 45 (2017) 180–194, <https://doi.org/10.1007/s10439-016-1611-9>.
- [27] D. Caballero, S. Kaushik, V.M. Correlo, J.M. Oliveira, R.L. Reis, S.C. Kundu, Organ-on-chip models of cancer metastasis for future personalized medicine: from chip to the patient, *Biomaterials* 149 (2017) 98–115, <https://doi.org/10.1016/j.biomaterials.2017.10.005>.
- [28] Y. Kang, P. Datta, S. Shanmugapriya, I.T. Ozbolat, 3D bioprinting of tumor models for cancer research, *ACS Appl. Bio Mater.* 3 (9) (2020) 5552–5573, <https://doi.org/10.1021/acsabm.0c00791>.
- [29] W. Wan, Z. Li, X. Wang, F. Tian, J. Yang, Surface-fabrication of fluorescent hydroxyapatite for cancer cell imaging and bio-printing applications, *Biosensors (Basel)* 12 (6) (2022) 419, <https://doi.org/10.3390/bios12060419>.
- [30] A. Memic, A. Navaei, B. Mirani, J.A.V. Cordova, M. Aldahri, A. Dolatshahi-Pirouz, M. Akbari, M. Nikkhah, Bioprinting technologies for disease modeling, *Biotechnol. Lett* 39 (9) (2017) 1279–1290, <https://doi.org/10.1007/s10529-017-2360-z>.
- [31] J.M. Lee, W.Y. Yeong, Design and printing strategies in 3d bioprinting of cell-hydrogels: a review, *Adv. Healthc. Mater.* 5 (22) (2016) 2856–2865, <https://doi.org/10.1002/adhm.201600435>.

- [32] R. Suntornnond, W.L. Ng, X. Huang, C.H.E. Yeong, W.Y. Yeong, Improving printability of hydrogel-based bio-inks for thermal inkjet bioprinting applications via saponification and heat treatment processes, *J. Mater. Chem. B* 10 (31) (2022) 5989–6000, <https://doi.org/10.1039/D2TB00442A>.
- [33] X. Li, B. Liu, B. Pei, J. Chen, D. Zhou, J. Peng, X. Zhang, W. Jia, T. Xu, Inkjet bioprinting of biomaterials, *Chem. Rev.* 120 (19) (2020) 10793–10833, <https://doi.org/10.1021/acs.chemrev.0c00008>.
- [34] P. Kumar, S. Ebbens, X. Zhao, Inkjet printing of mammalian cells—theory and applications, *Bioprinting* 23 (2021) e00157, <https://doi.org/10.1016/j.bioprint.2021.e00157>.
- [35] N. Bhardwaj, S. Dey, B. Bhar, B.B. Mandal, Bioprinted in vitro tissue models: an emerging platform for developing therapeutic interventions and disease modelling, *Prog. Biomed. Eng.* 6 (1) (2023), <https://doi.org/10.1088/2516-1091/ad10b4>.
- [36] J. Bohandy, B.F. Kim, F.J. Adrian, Metal deposition from a supported metal film using an excimer laser, *J. Appl. Phys.* 60 (4) (1986) 1538–1539, <https://doi.org/10.1063/1.337287>.
- [37] J. Li, M. Chen, X. Fan, H. Zhou, Recent advances in bioprinting techniques: approaches, applications and future prospects, *J. Transl. Med.* 14 (2016) 271, <https://doi.org/10.1186/s12967-016-1208-0>.
- [38] F. Guillermot, A. Souquet, S. Catros, B. Guillotin, Laser-assisted cell printing: principle, physical parameters versus cell fate and perspectives in tissue engineering, *Nanomedicine (Lond.)* 5 (3) (2010) 507–515, <https://doi.org/10.2217/nmm.10.14>.
- [39] F. Guillermot, A. Souquet, S. Catros, B. Guillotin, J. Lopez, M. Faucon, B. Pippenger, R. Bareille, M. Rémy, S. Bellance, High-throughput laser printing of cells and biomaterials for tissue engineering, *Acta Biomater.* 6 (7) (2010) 2494–2500, <https://doi.org/10.1016/j.actbio.2009.09.029>.
- [40] B.R. Ringeisen, S.E. Lizewski, L.A. Fitzgerald, J.C. Biffinger, C.L. Knight, W. J. Crookes-Goodson, P.K. Wu, Single cell isolation of bacteria from microbial fuel cells and potomac river sediment, *Electroanalysis* 22 (7–8) (2010) 875–882, <https://doi.org/10.1002/elan.200880012>.
- [41] B. Guillotin, A. Souquet, S. Catros, M. Duocastella, B. Pippenger, S. Bellance, R. Bareille, M. Rémy, L. Bordenave, J. Amédée, Laser assisted bioprinting of engineered tissue with high cell density and microscale organization, *Biomaterials* 31 (28) (2010) 7250–7256, <https://doi.org/10.1016/j.biomaterials.2010.05.055>.
- [42] O. Kérourédan, D. Hakobyan, M. Rémy, S. Ziane, N. Dusserre, J.C. Fricain, S. Delmond, N.B. Thébaud, R. Devillard, In situ prevascularization designed by laser-assisted bioprinting: effect on bone regeneration, *Biofabrication* 11 (4) (2019) 045002, <https://doi.org/10.1088/1758-5090/ab2620>.
- [43] P. Delaporte, A.-P. Allioncle, Laser-induced forward transfer: a high resolution additive manufacturing technology, *Opt. Laser Technol.* 78 (2016) 33–41, <https://doi.org/10.1016/j.optlastec.2015.09.022>.
- [44] A. Bakhsinejad, R.M. D’Souza, A brief comparison between available bio-printing methods, *IEEE Great Lakes Biomed. Conf. (GLBC) 2015* (2015) 1–3, <https://doi.org/10.1109/GLBC.2015.7158294>.
- [45] B. Hopp, T. Smasz, N. Kresz, N. Barna, Z. Bor, L. Kolozsvári, D.B. Chrisey, A. Szabó, A. Nőgrádi, Survival and proliferative ability of various living cell types after laser-induced forward transfer, *Tissue Eng.* 11 (11–12) (2005) 1817–1823, <https://doi.org/10.1089/ten.2005.11.1817>.
- [46] M. Gruene, A. Deiwick, L. Koch, S. Schlie, C. Unger, N. Hofmann, I. Bernemann, B. Glasmachler, B. Chichkov, Laser printing of stem cells for biofabrication of scaffold-free autologous grafts, *Tissue Eng. Part C Methods* 17 (1) (2011) 79–87, <https://doi.org/10.1089/ten.TEC.2010.0359>.
- [47] L. Koch, S. Kuhn, H. Sorg, M. Gruene, S. Schlie, R. Gaebel, B. Polchow, K. Reimers, S. Stoelting, N. Ma, P.M. Vogt, G. Steinhoff, B. Chichkov, Laser printing of skin cells and human stem cells, *Tissue Eng. Part C Methods* 16 (5) (2010) 847–854, <https://doi.org/10.1089/ten.TEC.2009.0397>.
- [48] B. Qiu, N. Bessler, K. Figler, M.B. Buchholz, A.C. Rios, J. Malda, R. Levato, M. Caiazzo, Bioprinting neural systems to model central nervous system diseases, *Adv. Functional Mater.* 30 (44) (2020) 1910250, <https://doi.org/10.1002/adfm.201910250>.
- [49] J.Z. Manapat, Q. Chen, P. Ye, R.C. Advincula, 3D printing of polymer nanocomposites via stereolithography, *Macromol. Mater. Eng.* 302 (9) (2017) 1600553, <https://doi.org/10.1002/mame.201600553>.
- [50] Z. Wang, R. Abdulla, B. Parker, R. Samanipour, S. Ghosh, K. Kim, A simple and high-resolution stereolithography-based 3D Bioprinting system using visible light crosslinkable bioinks, *Biofabrication* 7 (4) (2015) 045009, <https://doi.org/10.1088/1758-5090/7/4/045009>.
- [51] S.P. Grogan, P.H. Chung, P. Soman, P. Chen, M.K. Lotz, S. Chen, D.D. D’Lima, Digital micromirror device projection printing system for meniscus tissue engineering, *Acta Biomater.* 9 (7) (2013) 7218–7226, <https://doi.org/10.1016/j.actbio.2013.03.020>.
- [52] R. Gauvin, Y.-C. Chen, J.W. Lee, P. Soman, P. Zorlutuna, J.W. Nichol, H. Bae, S. Chen, A. Khademhosseini, Microfabrication of complex porous tissue engineering scaffolds using 3D projection stereolithography, *Biomaterials* 33 (15) (2012) 3824–3834, <https://doi.org/10.1016/j.biomaterials.2012.01.048>.
- [53] T.Q. Huang, X. Qu, J. Liu, S. Chen, 3D printing of biomimetic microstructures for cancer cell migration, *Biomed. Microdevices* 16 (2014) 127–132, <https://doi.org/10.1007/s10544-013-9812-6>.
- [54] H. Lin, D. Zhang, P.G. Alexander, G. Yang, J. Tan, A.-W.-M. Cheng, R.S. Tuan, Application of visible light-based projection stereolithography for live cell-scaffold fabrication with designed architecture, *Biomaterials* 34 (2) (2013) 331–339, <https://doi.org/10.1016/j.biomaterials.2012.09.048>.
- [55] L.S.S. Magalhães, F.E.P. Santos, C.D.M.V. Elias, S. Afewerki, G.F. Sousa, A. S. Furtado, F.R. Marciano, A.O. Lobo, Printing 3D hydrogel structures employing low-cost stereolithography technology, *J. Funct. Biomater.* 11 (1) (2020) 12, <https://doi.org/10.3390/jfb11010012>.
- [56] S.-J. Lee, M. Nowicki, B. Harris, L.G. Zhang, Fabrication of a highly aligned neural scaffold via a table top stereolithography 3D printing and electrospinning, *Tissue Eng. Part A* 23 (11–12) (2017) 491–502, <https://doi.org/10.1089/ten.TEA.2016.0353>.
- [57] E. Tamjid, A. Simchi, Fabrication of a highly ordered hierarchically designed porous nanocomposite via indirect 3D printing: mechanical properties and in vitro cell responses, *Mater. Des.* 88 (2015) 924–931, <https://doi.org/10.1016/j.matedes.2015.08.133>.
- [58] J.-Q. Wang, B.-J. Jiang, W.-J. Guo, Y.-M. Zhao, Indirect 3D printing technology for the fabrication of customised β-TCP/chitosan scaffold with the shape of rabbit radial head—an in vitro study, *J. Orthop. Surg. Res.* 14 (2019) 102, <https://doi.org/10.1186/s13018-019-1136-7>.
- [59] J.S. Miller, K.R. Stevens, M.T. Yang, B.M. Baker, D.-H.-T. Nguyen, D.M. Cohen, E. Toro, A.A. Chen, P.A. Galie, X. Yu, Rapid casting of patterned vascular networks for perfusable engineered three-dimensional tissues, *Nat. Mater.* 11 (9) (2012) 768–774, <https://doi.org/10.1038/nmat3357>.
- [60] E.Y.S. Tan, R. Suntornnond, W.Y. Yeong, High-resolution novel indirect bioprinting of low-viscosity cell-laden hydrogels via model-support bioink interaction, *3D Print. Addit. Manuf.* 8 (1) (2021) 69–78, <https://doi.org/10.1089/3dp.2020.0153>.
- [61] S. Wüst, M.E. Godla, R. Müller, S. Hofmann, Tunable hydrogel composite with two-step processing in combination with innovative hardware upgrade for cell-based three-dimensional bioprinting, *Acta Biomater.* 10 (2) (2014) 630–640, <https://doi.org/10.1016/j.actbio.2013.10.016>.
- [62] T.J. Hinton, Q. Jallerat, R.N. Palchesko, J.H. Park, M.S. Grodzicki, H.-J. Shue, M. H. Ramadan, A.R. Hudson, A.W. Feinberg, Three-dimensional printing of complex biological structures by freeform reversible embedding of suspended hydrogels, *Sci. Adv.* 1 (9) (2015) e1500758, <https://doi.org/10.1126/sciadv.1500758>.
- [63] A. Lee, A.R. Hudson, D.J. Shiawski, J.W. Tashman, T.J. Hinton, S. Yerneni, J. M. Biley, P.G. Campbell, A.W. Feinberg, 3D bioprinting of collagen to rebuild components of the human heart, *Science* 365 (6452) (2019) 482–487, <https://doi.org/10.1126/science.aav9051>.
- [64] P. Siqueira, É. Siqueira, A.E. De Lima, G. Siqueira, A.D. Pinzón-Garcia, A.P. Lopes, M.E.C. Segura, A. Isaac, V.R. Pereira, V.R. Botaro, Three-dimensional stable alginate-nanocellulose gels for biomedical applications: towards tunable mechanical properties and cell growing, *Nanomaterials (Basel)* 9 (1) (2019) 78, <https://doi.org/10.3390/nano9010078>.
- [65] J. Kajtez, M.F. Wesseler, M. Birtèle, F.R. Khorasgani, D. Rylander Ottosson, A. Heiskanen, T. Kamperman, J. Leijten, A. Martínez-Serrano, N.B. Larsen, T. E. Angelini, M. Parmar, J.U. Lind, J. Emnéus, Embedded 3D printing in self-healing annealable composites for precise patterning of functionally mature human neural constructs, *Adv. Sci. (Weinh.)*, 9 (25) (2022) e2201392, <https://doi.org/10.1002/ADVS.202201392>.
- [66] E. Mirdamadi, J.W. Tashman, D.J. Shiawski, R.N. Palchesko, A.W. Feinberg, FRESH 3D bioprinting a full-size model of the human heart, *ACS Biomater. Sci. Eng.* 6 (11) (2020) 6453–6459, <https://doi.org/10.1021/acsbiomaterials.0c01133>.
- [67] M. Rahimnejad, A. Adouguetchodo, N.R. Demarquette, S. Lerouge, FRESH bioprinting of biodegradable chitosan thermosensitive hydrogels, *Bioprinting* 27 (2022) e00209, <https://doi.org/10.1016/j.bioprint.2022.e00209>.
- [68] D.J. Shiawski, A.R. Hudson, J.W. Tashman, A.W. Feinberg, Emergence of FRESH 3D printing as a platform for advanced tissue biofabrication, *APL Bioeng.* 5 (1) (2021) 010904, <https://doi.org/10.1063/5.0032777>.
- [69] I.A. Marques, C. Fernandes, N.T. Tavares, A.S. Pires, A.M. Abrantes, M.F. Botelho, Magnetic-based human tissue 3D cell culture: a systematic review, *Int. J. Mol. Sci.* 23 (20) (2022) 12681, <https://doi.org/10.3390/ijms232012681>.
- [70] H. Tseng, L.R. Balaqong, B. Grigoryan, R.M. Raphael, T.C. Killian, G.R. Souza, K. J. Grande-Allen, A three-dimensional co-culture model of the aortic valve using magnetic levitation, *Acta Biomater.* 10 (1) (2014) 173–182, <https://doi.org/10.1016/j.actbio.2013.09.003>.
- [71] H. Tseng, A.C. Daquinag, G.R. Souza, M.G. Kolonin, Three-dimensional magnetic levitation culture system simulating white adipose tissue, *Methods Mol Biol* 1773 (2018) 147–154, https://doi.org/10.1007/978-1-4939-7799-4_12.
- [72] A. Van de Walle, J.E. Perez, C. Wilhelm, Magnetic Bioprinting of Stem Cell-Based Tissues, *Bioprinting* 30 (2023) e00265, <https://doi.org/10.1016/j.bioprint.2023.e00265>.
- [73] A. Van de Walle, A.P. Sangnier, A. Abou-Hassan, A. Curcio, M. Hémadi, N. Menguy, Y. Lalatonne, N. Luciani, C. Wilhelm, Biosynthesis of Magnetic nanoparticles from nanodegradation products revealed in human stem cells, *Proc. Natl. Acad. Sci. U S A* 116 (10) (2019) 4044–4053, <https://doi.org/10.1073/pnas.1816792116>.
- [74] G. Trujillo-de Santiago, M.M. Alvarez, M. Samandari, G. Prakash, G. Chandrabhatla, P.I. Rellstab-Sánchez, B. Byambaa, P.P.S.S. Abadi, S. Mandla, R.K. Avery, A. Vallejo-Arroyo, Chaotic printing: using chaos to fabricate densely packed micro- and nanostructures at high resolution and speed, *Mater. Horiz.* 5 (5) (2018) 813–822, <https://doi.org/10.1039/c8mh00344k>.
- [75] M.M. Alvarez, A. Cantoral-Sánchez, G. Trujillo-de Santiago, Chaotic (Bio)printing in the context of drug delivery systems, *Adv. Drug Deliv. Rev.* 216 (2025) 115475, <https://doi.org/10.1016/J.ADDR.2024.115475>.
- [76] W. Balestri, R. Sharma, V.A. da Silva, B.C. Bobotis, A.J. Curle, V. Kothakota, F. Kalantarnia, M.V. Hangad, M. Hoofar, J.L. Jones, M.É. Tremblay, Modeling the neuroimmune system in Alzheimer’s and Parkinson’s diseases,

- J. Neuroinflammation 21 (1) (2024) 32, <https://doi.org/10.1186/s12974-024-03024-8>.
- [77] I. Chiaradia, M.A. Lancaster, Brain organoids for the study of human neurobiology at the interface of in vitro and in vivo, *Nat. Neurosci.* 23 (12) (2020) 1496–1508, <https://doi.org/10.1038/s41593-020-00730-3>.
- [78] M. Hofer, M.P. Lutolf, Engineering organoids, *Nat. Rev. Mater.* 6 (5) (2021) 402–420, <https://doi.org/10.1038/s41578-021-00279-y>.
- [79] C.M. Leung, P. De Haan, K. Ronaldson-Bouchard, G.A. Kim, J. Ko, H.S. Rho, Z. Chen, P. Habibovic, N.L. Jeon, S. Takayama, M.L. Shuler, A guide to the organ-on-a-chip, *Nat. Rev. Methods Primers* 2 (1) (2022) 33, <https://doi.org/10.1038/s43586-022-00118-6>.
- [80] Y. Shin, S.H. Choi, E. Kim, E. Bylykbashi, J.A. Kim, S. Chung, D.Y. Kim, R.D. Kamm, R.E. Tanzi, Blood-brain barrier dysfunction in a 3D in vitro model of Alzheimer's disease, *Adv. Sci. (Weinh.)* 6 (20) (2019) 1900962, <https://doi.org/10.1002/advs.201900962>.
- [81] H. Cho, T. Hashimoto, W. Yoon, Y. Hori, L.B. Wood, L. Zhao, K.M. Haigis, B.T. Hyman, D. Irimia, Microfluidic chemotaxis platform for differentiating the roles of soluble and bound amyloid- β on microglial accumulation, *Sci. Rep.* 3 (2013) 1823, <https://doi.org/10.1038/srep01823>.
- [82] Y.J. Choi, S. Chae, J.H. Kim, K.F. Barald, J.Y. Park, S.H. Lee, Neurotoxic amyloid beta oligomer assemblies recreated in microfluidic platform with interstitial level of slow flow, *Sci. Rep.* 3 (2013) 1921, <https://doi.org/10.1038/srep01921>.
- [83] S. Seo, C.H. Choi, K.S. Yi, S.U. Kim, K. Lee, N. Choi, H.J. Lee, S.H. Cha, H.N. Kim, An engineered neurovascular unit for modeling neuroinflammation, *Biofabrication* 13 (3) (2021), <https://doi.org/10.1088/1758-5090/abf741>.
- [84] H. Uwamori, T. Higuchi, K. Arai, R. Sudo, Integration of neurogenesis and angiogenesis models for constructing a neurovascular tissue, *Sci. Rep.* 7 (1) (2017) 17349, <https://doi.org/10.1038/s41598-017-17411-0>.
- [85] H.G. Yi, Y.H. Jeong, Y. Kim, Y.J. Choi, H.E. Moon, S.H. Park, K.S. Kang, M. Bae, J. Jang, H. Youn, S.H. Paek, D.W. Cho, A bioprinted human-glioblastoma-on-a-chip for the identification of patient-specific responses to chemoradiotherapy, *Nat. Biomed. Eng.* 3 (2019) 509–519, <https://doi.org/10.1038/s41551-019-0363-x>.
- [86] G. Akcay, R. Luttge, Microenvironments matter: advances in brain-on-chip, *Biosensors (Basel)* 13 (5) (2023) 551, <https://doi.org/10.3390/BIOS13050551>.
- [87] L. Amirifar, A. Shamloo, R. Nasiri, N.R. de Barros, Z.Z. Wang, B.D. Unlurturk, A. Libanori, O. Ievglevskyi, S.E. Diltemiz, S. Sances, I. Balasingham, S.K. Seidlits, N. Ashammakhi, Brain-on-a-chip: recent advances in design and techniques for microfluidic models of the brain in health and disease, *Biomaterials* 285 (2022) 121531, <https://doi.org/10.1016/J.BIOMATERIALS.2022.121531>.
- [88] A. Harper, Mouse models of neurological disorders—a comparison of heritable and acquired traits, *Biochim. Biophys. Acta.* 1802 (10) (2010) 785–795, <https://doi.org/10.1016/j.bbapplied.2010.05.009>.
- [89] D. Siolas, G.J. Hannon, Patient-derived tumor xenografts: transforming clinical samples into mouse models, *Cancer Res.* 73 (17) (2013) 5315–5319, <https://doi.org/10.1158/0008-5472.CAN-13-1069>.
- [90] B.J. Casey, C.E. Glatt, F.S. Lee, Treating the developing versus developed brain: translating preclinical mouse and human studies, *Neuron* 86 (6) (2015) 1358–1368, <https://doi.org/10.1016/j.neuron.2015.05.020>.
- [91] A.F. Haddad, J.S. Young, D. Amara, M.S. Berger, D.R. Raleigh, M.K. Aghi, N.A. Butowski, Mouse models of glioblastoma for the evaluation of novel therapeutic strategies, *Neurooncol Adv* 3 (1) (2021) vdab100, <https://doi.org/10.1093/noajn/vdab100>.
- [92] Y. Liu, F. Zhou, H. Ali, J.D. Lathia, P. Chen, Immunotherapy for glioblastoma: current state, challenges, and future perspectives, *Cell. Mol. Immunol.* 21 (12) (2024) 1354–1375, <https://doi.org/10.1038/s41423-024-01226-x>.
- [93] M. Jucker, The benefits and limitations of animal models for translational research in neurodegenerative diseases, *Nat. Med.* 16 (11) (2010) 1210–1214, <https://doi.org/10.1038/nm.2224>.
- [94] M.J. Page, J.E. McKenzie, P.M. Bossuyt, I. Boutron, T.C. Hoffmann, C.D. Mulrow, L. Shamseer, J.M. Tetzlaff, E.A. Akl, S.E. Brennan, R. Chou, J. Glanville, J. Grimshaw, A. Hróbjartsson, M.M. Lau, T. Li, E.W. Loder, E. Mayo-Wilson, S. McDonald, L.A. McGuinness, L.A. Stewart, J. Thomas, A.C. Tricco, V.A. Welch, P. Whiting, D. Moher, The PRISMA 2020 Statement: An Updated Guideline for Reporting Systematic Reviews, *BMJ* 372 (2021) n71, <https://doi.org/10.1136/bmj.n71>.
- [95] H.-W. Lee, K.-T. Chen, Y.-C.-E. Li, Y.-C. Yeh, C.-Y. Chiang, I.-C. Lee, Dual crosslinking silk fibroin/pectin-based bioink development and the application on neural stem/progenitor cells spheroid laden 3D bioprinting, *Int. J. Biol. Macromol.* 269 (2024) 131720, <https://doi.org/10.1016/j.ijbiomac.2024.131720>.
- [96] R. Lozano, L. Stevens, B.C. Thompson, K.J. Gilmore, R. Gorkin, E.M. Stewart, M. in het Panhuis, M. Romero-Ortega, G.G. Wallace, 3D Printing of Layered Brain-like Structures Using Peptide Modified Gellan Gum Substrates, *Biomaterials* 67 (2015) 264–273, <https://doi.org/10.1016/j.biomaterials.2015.07.022>.
- [97] L. Zhou, A.C. Wolfes, Y. Li, D.C.W. Chan, H. Ko, F.G. Szele, H. Bayley, Lipid-bilayer-supported 3D printing of human cerebral cortex cells reveals developmental interactions, *Adv. Mater.* 32 (31) (2020) e2002183, <https://doi.org/10.1002/adma.202002183>.
- [98] Q. Gu, E. Tomaskovic-Crook, R. Lozano, Y. Chen, R.M. Kapsa, Q. Zhou, G. G. Wallace, J.M. Crook, Functional 3D neural mini-tissues from printed gel-based bioinks and human neural stem cells, *Adv. Healthc. Mater.* 5 (12) (2016) 1429–1438, <https://doi.org/10.1002/adhm.201600095>.
- [99] Q. Gu, E. Tomaskovic-Crook, G.G. Wallace, J.M. Crook, 3D bioprinting human induced pluripotent stem cell constructs for in situ cell proliferation and successive multilineage differentiation, *Adv. Healthc. Mater.* 6 (17) (2017), <https://doi.org/10.1002/ADHM.201700175>.
- [100] Q. Gu, E. Tomaskovic-Crook, G.G. Wallace, J.M. Crook, Engineering human neural tissue by 3D bioprinting, *Methods Mol. Biol.* 1758 (2018) 129–138, https://doi.org/10.1007/978-1-4939-7741-3_10.
- [101] V. Fantini, M. Bordoni, F. Scocozza, M. Conti, E. Scarian, S. Carelli, A.M. Di Giulio, S. Marconi, O. Pansarasa, F. Auricchio, C. Cereda, Bioink composition and printing parameters for 3D modeling neural tissue, *Cells* 8 (8) (2019) 830, <https://doi.org/10.3390/cells8080830>.
- [102] E. Abelseth, L. Abelseth, L. De La Vega, S.T. Beyer, S.J. Wadsworth, S.M. Willerth, 3D printing of neural tissues derived from human induced pluripotent stem cells using a fibrin-based bioink, *ACS Biomater. Sci. Eng.* 5 (1) (2019) 234–243, <https://doi.org/10.1021/acsbiomaterials.8b01235>.
- [103] R. Sharma, I.P.M. Smits, L. De La Vega, C. Lee, S.M. Willerth, 3D bioprinting pluripotent stem cell derived neural tissues using a novel fibrin bioink containing drug releasing microspheres, *Front. Bioeng. Biotechnol.* 8 (2020) 57, <https://doi.org/10.3389/fbioe.2020.00057>.
- [104] M. Restan Perez, R. Sharma, N.Z. Masri, S.M. Willerth, 3D bioprinting mesenchymal stem-cell derived neural tissues using a fibrin-based bioink, *Biomolecules* 11 (8) (2021) 1250, <https://doi.org/10.3390/biom11081250>.
- [105] M.R. Perez, N.Z. Masri, J. Walters-Shumka, S. Kahale, S.M. Willerth, Protocol for 3D bioprinting mesenchymal stem cell-derived neural tissues using a fibrin-based bioink, *Bio Protoc* 13 (9) (2023) e4663, <https://doi.org/10.21769/BIOPROTOC.4663>.
- [106] J. Chrenek, R. Kirsch, K. Scheck, S.M. Willerth, Protocol for printing 3D neural tissues using the BIO X equipped with a pneumatic printhead, *STAR Protoc* 3 (2) (2022) 101348, <https://doi.org/10.1016/j.xpro.2022.101348>.
- [107] C. Benwood, J. Walters-Shumka, K. Scheck, S.M. Willerth, 3D bioprinting patient-derived induced pluripotent stem cell models of Alzheimer's disease using a smart bioink, *Bioelectron Med* 9 (1) (2023) 10, <https://doi.org/10.1186/s42234-02-30012-7>.
- [108] Y.-C.-E. Li, Y.A. Jodat, R. Samanipour, G. Zorzi, K. Zhu, M. Hirano, K. Chang, A. Arnaout, S. Hassan, N. Matharu, A. Khademhosseini, M. Hoorfar, S.R. Shin, Toward a neurospheroid niche model: optimizing embedded 3D bioprinting for fabrication of neurospheroid brain-like co-culture constructs, *Biofabrication* 13 (1) (2020), <https://doi.org/10.1088/1758-5090/ABC1BE>.
- [109] M.C. Chiang, C.J.B. Nicol, C.H. Lin, S.J. Chen, C. Yen, R.N. Huang, Nanogold induces anti-inflammation against oxidative stress induced in human neural stem cells exposed to amyloid-beta peptide, *Neurochem. Int.* 145 (2021) 104992, <https://doi.org/10.1016/J.NEUNINT.2021.104992>.
- [110] B.A.G. da Melo, M.V. Mundim, R.M.R. Lemes, E.M. Cruz, T.N. Ribeiro, C. F. Santiago, J.H.L. da Fonseca, J.C. Benincasa, R.S. Stilhano, N. Mantovani, L. C. Santana, R. Durães-Carvalho, R.S. Diaz, L.M.R. Janini, J.T. Maricato, M. A. Porcionatto, 3D bioprinted neural-like tissue as a platform to study neurotropism of mouse-adapted SARS-CoV-2, *Adv Biol. (Weing)* 6 (8) (2022) e220002, <https://doi.org/10.1002/abdi.202200002>.
- [111] E. Scarian, M. Bordoni, V. Fantini, E. Jacchetti, M.T. Raimondi, L. Diamanti, S. Carelli, C. Cereda, O. Pansarasa, Patients' Stem cells differentiation in a 3D environment as a promising experimental tool for the study of amyotrophic lateral sclerosis, *Int. J. Mol. Sci.* 23 (10) (2022) 5344, <https://doi.org/10.3390/IJMS23105344>.
- [112] I. Matthiesen, M. Jury, F. Rasti Boroojeni, S.L. Ludwig, M. Holzreuter, S. Buchmann, A. Åman Träger, R. Selegård, T.E. Winkler, D. Aili, A. Herland, Astrocyte 3D culture and bioprinting using peptide functionalized hyaluronan hydrogels, *Sci. Technol. Adv. Mater.* 24 (1) (2023) 2165871, <https://doi.org/10.1080/14686996.2023.2165871>.
- [113] Z. Wang, C. Huang, H. Liu, Z. Shi, X. Han, S. Li, J. Huang, Z. Wang, Y. Yan, Z. Chen, Two-step method fabricating a 3D nerve cell model with brain-like mechanical properties and tunable porosity vascular structures via coaxial printing, *Colloids Surf. B Biointerfaces* 224 (2023) 113202, <https://doi.org/10.1016/J.COLSURFB.2023.113202>.
- [114] B. Yavuz, A.P.Z. Yıldız, E.S. Abamor, H. Darıcı, A.M. Allahverdiyev, Neuroprotective effects of wharton jelly stem cell-derived exosomes developed as nano-drug delivery system in 6-OHDA-induced neurotoxicity in 2D and 3D neuronal cell line, *Regen. Eng. Transl. Med.* 10 (2023) 243–252, <https://doi.org/10.1007/s40883-023-00322-0>.
- [115] L. Wang, L. Bai, S. Wang, J. Zhou, Y. Liu, C. Zhang, S. Yao, J. He, C. Liu, D. Li, Biomimetic design and integrated biofabrication of an in-vitro three-dimensional multi-scale multilayer cortical model, *Mater. Today Bio* 28 (2024) 101176, <https://doi.org/10.1016/j.mtbiol.2024.101176>.
- [116] E.M. Cruz, L.S. Machado, L.N. Zamproni, L.V. Bim, P.S. Ferreira, L.A. Pinto, L. A. Pessan, E.H. Backes, M.A. Porcionatto, A gelatin methacrylate-based hydrogel as a potential bioink for 3D bioprinting and neuronal differentiation, *Pharmaceutics* 15 (2) (2023), <https://doi.org/10.3390/PHARMACEUTICS15020627>.
- [117] J. Li, A. Reimers, K.M. Dang, M.G.K. Brunk, J. Drewes, U.M. Hirsch, C. Willem, C. E.H. Schmelzer, T. Groth, A.S. Nia, X. Feng, R. Adelung, W.D. Sacher, F. Schütt, J. K.S. Poon, 3D printed neural tissues with in situ optical dopamine sensors, *Biosens. Bioelectron.* 222 (2023) 114942, <https://doi.org/10.1016/J.BIOSENS.2022.114942>.
- [118] D. Joung, V. Truong, C.C. Neitzke, S.Z. Guo, P.J. Walsh, J.R. Monat, F. Meng, S. H. Park, J.R. Dutton, A.M. Parr, M.C. McAlpine, 3D printed stem-cell derived neural progenitors generate spinal cord scaffolds, *Adv. Funct. Mater.* 28 (39) (2018) 1801850, <https://doi.org/10.1002/adfm.201801850>.
- [119] L. de la Vega, D.A.R. Gómez, E. Abelseth, L. Abelseth, V.A. da Silva, S.M. Willerth, 3D bioprinting human induced pluripotent stem cell-derived neural tissues using

- a novel lab-on-a-printer technology, *Applied Sciences (Switzerland)* 8 (12) (2018) 2414, <https://doi.org/10.3390/app8122414>.
- [120] Y. Han, M. King, E. Tikhomirov, P. Barasa, C.D.S. Souza, J. Lindh, D. Baltrukiene, L. Ferraiuolo, M. Azzouz, M.R. Gullo, E.N. Kozlova, Towards 3D bioprinted spinal cord organoids, *Int. J. Mol. Sci.* 23 (10) (2022) 5788, <https://doi.org/10.3390/ijms23105788>.
- [121] S. Song, Y. Li, J. Huang, S. Cheng, Z. Zhang, Inhibited Astrocytic differentiation in neural stem cell-laden 3D bioprinted conductive composite hydrogel scaffolds for repair of spinal cord injury, *Biomater. Adv.* 148 (2023) 213385, <https://doi.org/10.1016/J.BIOADV.2023.213385>.
- [122] X. Wang, X. Li, Y. Zhang, X. Long, H. Zhang, T. Xu, C. Niu, Coaxially bioprinted cell-laden tubular-like structure for studying glioma angiogenesis, *Front. Bioeng. Biotechnol.* 9 (2021) 761861, <https://doi.org/10.3389/fbioe.2021.761861>.
- [123] C. Lee, E. Abelseth, L. de la Vega, S.M. Willerth, Bioprinting a novel glioblastoma tumor model using a fibrin-based bioink for drug screening, *Mater. Today Chem.* 12 (2019) 78–84, <https://doi.org/10.1016/j.mtchem.2018.12.005>.
- [124] I.P.M. Smits, O.W. Blaschuk, S.M. Willerth, Novel N-cadherin antagonist causes glioblastoma cell death in a 3D bioprinted co-culture model, *Biochem. Biophys. Res. Commun.* 529 (2) (2020) 162–168, <https://doi.org/10.1016/j.bbrc.2020.06.001>.
- [125] M. Tang, S.K. Tiwari, K. Agrawal, M. Tan, J. Dang, T. Tam, J. Tian, X. Wan, J. Schimelman, S. You, Q. Xia, T.M. Rana, S. Chen, Rapid 3D Bioprinting of glioblastoma model mimicking native biophysical heterogeneity, *Small* 17 (15) (2021) e2006050, <https://doi.org/10.1002/smll.202006050>.
- [126] L. Neufeld, E. Yeini, N. Reisman, Y. Shitlerman, D. Ben-Shushan, S. Pozzi, A. Madi, G. Tiram, A. Eldar-Boock, S. Ferber, R. Grossman, Z. Ram, R. Satchi-Fainaro, Microengineered perfusable 3D-bioprinted glioblastoma model for in vivo mimicry of tumor microenvironment, *Sci. Adv.* 7 (34) (2021) eabi9119, <https://doi.org/10.1126/sciadv.abi9119>.
- [127] V. Sunil, J.H. Teoh, B.C. Mohan, A. Mozhai, C.H. Wang, Bioengineered immunomodulatory organelle targeted nanozymes for photodynamic immunometabolic therapy, *J. Control. Release* 350 (2022) 215–227, <https://doi.org/10.1016/J.JCONREL.2022.08.025>.
- [128] E. Tomaskovic-Crook, J.M. Crook, 3D bioprinting electrically conductive bioink with human neural stem cells for human neural tissues, *Methods Mol. Biol.* 2140 (2020) 159–170, https://doi.org/10.1007/978-1-0716-0520-2_10.
- [129] J. Kapr, L. Petersilie, T. Distler, I. Lauria, F. Bendt, C.M. Sauter, A.R. Boccaccini, C.R. Rose, E. Fritzsche, Human induced pluripotent stem cell-derived neural progenitor cells produce distinct neural 3D In vitro models depending on alginate/gellan gum/laminin hydrogel blend properties, *Adv. Healthc. Mater.* 10 (16) (2021) e2100131, <https://doi.org/10.1002/ADHM.202100131>.
- [130] B.A.G. de Melo, E.M. Cruz, T.N. Ribeiro, M.V. Mundim, M.A. Porcionatto, 3D bioprinting of murine cortical astrocytes for engineering neural-like tissue, *J. Vis. Exp.* (173) (2021), <https://doi.org/10.3791/62691>.
- [131] M.A. Sullivan, S. Lane, A. Volkerling, M. Engel, E.L. Werry, M. Kassiou, Three-dimensional bioprinting of stem cell-derived central nervous system cells enables astrocyte growth, vasculogenesis, and enhances neural differentiation/function, *Biotechnol. Bioeng.* 120 (10) (2023) 3079–3091, <https://doi.org/10.1002/bit.28470>.
- [132] A.P. Haring, E.G. Thompson, Y. Tong, S. Laheri, E. Cesewski, H. Sontheimer, B.N. Johnson, Process- and bio-inspired hydrogels for 3D bioprinting of soft free-standing neural and glial tissues, *Biofabrication* 11 (2) (2019) 025009, <https://doi.org/10.1088/1758-5090/ab02c9>.
- [133] C.D. Lindsay, J.G. Roth, B.L. LeSavage, S.C. Heilshorn, Bioprinting of stem cell expansion lattices, *Acta Biomater.* 95 (2019) 225–235, <https://doi.org/10.1016/j.actbio.2019.05.014>.
- [134] Q. Li, G. Qi, X. Liu, J. Bai, J. Zhao, G. Tang, Y.S. Zhang, R. Chen-Tsai, M. Zhang, D. Wang, Y. Zhang, A. Atala, J.Q. He, X.S. Sun, Universal peptide hydrogel for scalable physiological formation and bioprinting of 3D spheroids from human induced pluripotent stem cells, *Adv. Funct. Mater.* 31 (41) (2021), <https://doi.org/10.1002/adfm.202104046>.
- [135] L. Ning, H. Sun, T. Lelong, R. Guilloteau, N. Zhu, D.J. Schreyer, X. Chen, 3D Bioprinting of scaffolds with living schwann cells for potential nerve tissue engineering applications, *Biofabrication* 10 (3) (2018) 035014, <https://doi.org/10.1088/1758-5090/aacd30>.
- [136] S. Chatelin, A. Constantinesco, R. Willinger, Fifty years of brain tissue mechanical testing: from in vitro to in vivo investigations, *Biorheology* 47 (5–6) (2010) 255–276, <https://doi.org/10.3233/BIR-2010-0576>.
- [137] L. Chen, C. Yan, Z. Zheng, Functional polymer surfaces for controlling cell behaviors, *Mater. Today* 21 (1) (2018) 38–59, <https://doi.org/10.1016/j.matod.2017.07.002>.
- [138] K. Webb, V. Hlady, P.A. Fresco, Relative importance of surface wettability and charged functional groups on NIH 3T3 fibroblast attachment, spreading, and cytoskeletal organization, *J. Biomed. Mater. Res.* 41 (3) (1998) 422–430, [https://doi.org/10.1002/\(SICI\)1097-4636\(19980905\)41:3<422::AID-JBML12>3.0.CO;2-K](https://doi.org/10.1002/(SICI)1097-4636(19980905)41:3<422::AID-JBML12>3.0.CO;2-K).
- [139] G. Potjewyd, S. Moxon, T. Wang, M. Domingos, N.M. Hooper, Tissue engineering 3D neurovascular units: a biomaterials and bioprinting perspective, *Trends Biotechnol.* 36 (4) (2018) 457–472, <https://doi.org/10.1016/j.tibtech.2018.01.003>.
- [140] N.J. Shah, Z. Abbas, D. Ridder, M. Zimmermann, A.M. Oros-Peusquens, A novel MRI-based quantitative water content atlas of the human brain, *Neuroimage* 252 (2022) 119014, <https://doi.org/10.1016/j.neuroimage.2022.119014>.
- [141] Y.H. Kim, S.H. Choi, C. D'Avanzo, M. Hebischi, C. Sliwinski, E. Bylykbashi, K. J. Washicosky, J.B. Klee, O. Brüstle, R.E. Tanzi, D.Y. Kim, A 3D human neural cell culture system for modeling Alzheimer's disease, *Nat. Protoc.* 10 (7) (2015) 985–1006, <https://doi.org/10.1038/nprot.2015.065>.
- [142] L. Ouyang, R. Yao, Y. Zhao, W. Sun, Effect of bioink properties on printability and cell viability for 3D bioprinting of embryonic stem cells, *Biofabrication* 8 (3) (2016) 035020, <https://doi.org/10.1088/1758-5090/8/3/035020>.
- [143] T. Kanderi, S. Munakomi, V. Gupta, *Glioblastoma Multiforme*. 2024 May 6. In: StatPearls [Internet]. Treasure Island (FL): StatPearls Publishing. PMID: 32644380.
- [144] Y. Wang, S. Li, Y. Peng, W. Ma, Y. Wang, W. Li, Progress in phase III clinical trials of molecular-targeted therapy and immunotherapy for glioblastoma, *Cancer Innov.* 2 (2) (2023) 114–130, <https://doi.org/10.1002/cai2.59>.
- [145] Z.L. Liu, H.H. Chen, L.L. Zheng, L.P. Sun, L. Shi, *Angiogenic Signaling Pathways and Anti-Angiogenic Therapy for Cancer*. Signal Transduct Target Ther. 8 (1) (2023) 198, <https://doi.org/10.1038/s41392-023-01460-1>.
- [146] G. Gao, M. Ahn, W.W. Cho, B.S. Kim, D.W. Cho, 3D Printing of Pharmaceutical Application, Drug Screening and Drug Delivery. *Pharmaceutics*. 13 (9) (2021) 1373, <https://doi.org/10.3390/pharmaceutics13091373>.
- [147] S. Naghieh, M.D. Sarker, E. Abelseth, X. Chen, Indirect 3D bioprinting and characterization of alginate scaffolds for potential nerve tissue engineering applications, *J. Mech. Behav. Biomed. Mater.* 93 (2019) 183–193, <https://doi.org/10.1016/j.jmbbm.2019.02.014>.
- [148] Z. Wu, Q. Li, S. Xie, X. Shan, Z. Cai, In vitro and in vivo biocompatibility evaluation of a 3D bioprinted gelatin-sodium alginate/rat schwann-cell scaffold, *Mater. Sci. Eng. C Mater. Biol. Appl.* 109 (2020) 110530, <https://doi.org/10.1016/j.msec.2019.110530>.
- [149] J. Chen, D. Huang, L. Wang, J. Hou, H. Zhang, Y. Li, S. Zhong, Y. Wang, Y. Wu, W. Huang, 3D bioprinted multiscale composite scaffolds based on gelatin methacryloyl (GelMA)/chitosan microspheres as a modular bioink for enhancing 3D neurite outgrowth and elongation, *J. Colloid Interface Sci.* 574 (2020) 162–173, <https://doi.org/10.1016/j.jcis.2020.04.040>.
- [150] C. Whitehouse, N. Corbett, J. Brownlee, 3D models of neurodegeneration: implementation in drug discovery, *Trends Pharmacol Sci.* 44 (4) (2023) 208–221, <https://doi.org/10.1016/j.tips.2023.01.005>.
- [151] S.M. Willerth, Bioprinting neural tissues using stem cells as a tool for screening drug targets for Alzheimer's disease, *J. 3D Print. Med.* 2 (4) (2018) 163–165, <https://doi.org/10.2217/3dp-2018-0016>.
- [152] A.A. Friedman, A. Letai, D.E. Fisher, K.T. Flaherty, Precision medicine for cancer with next-generation functional diagnostics, *Nat. Rev. Cancer* 15 (12) (2015) 747–756, <https://doi.org/10.1038/nrc4015>.
- [153] J. Frearson, P. Wyatt, Drug Discovery in Academia: The Third Way? *Expert Opin Drug Discov.* 5 (10) (2010) 909–919, <https://doi.org/10.1517/17460441.2010.506508>.
- [154] M. Everts, M. Drew, Successfully Navigating the Valley of Death: The Importance of Accelerators to Support Academic Drug Discovery and Development, *Expert Opin Drug Discov.* 19 (2) (2024) 253–258, <https://doi.org/10.1080/17460441.2023.2284824>.
- [155] A.M. Palmer, The Role of the Blood Brain Barrier in Neurodegenerative Disorders and Their Treatment, *J Alzheimers Dis* 24 (4) (2011) 643–656, <https://doi.org/10.3233/JAD-2011-110368>.
- [156] R.M. Linville, P.C. Searn, Next-Generation In Vitro Blood–Brain Barrier Models: Benchmarking and Improving Model Accuracy, *Fluids Barriers CNS* 18 (1) (2021) 56, <https://doi.org/10.1186/s12987-021-00291-y>.
- [157] K.N.U. Galpayage Dona, S.H. Ramirez, A.M. Andrews, A next-generation 3D tissue-engineered model of the human brain microvasculature to study the blood-brain barrier, *Bioengineering (Basel)* 10 (7) (2023) 817, <https://doi.org/10.3390/bioengineering10070817>.
- [158] H. Han, S. Lee, G. Gao, H.G. Yi, S.H. Paek, J. Jang, Cerebrovascular-Specific Extracellular Matrix Bioink Promotes Blood-Brain Barrier Properties, *Biomater Res* 28 (2024) 0115, <https://doi.org/10.34133/bmr.0115>.
- [159] L.S. Paone, M.M. Benmassoud, A. Curran, S.L. Vega, P.A. Galie, A 3D-printed blood-brain barrier model with tunable topology and cell-matrix interactions, *Biofabrication* 16 (1) (2023), <https://doi.org/10.1088/1758-5090/ad0260>.
- [160] M. Tang, J.N. Rich, S. Chen, Biomaterials and 3D Bioprinting Strategies to Model Glioblastoma and the Blood–Brain Barrier, *Adv Mater* 33 (5) (2021) e2004776, <https://doi.org/10.1002/adma.202004776>.
- [161] V.A. da Silva, R. Sharma, E. Shtenberg, V. Patel, L. Bhardwaj, T. Garay, B. Yu, S. M. Willerth, Machine learning approaches to 3D models for drug screening, *Biomed. Mater. Devices.* 2 (2024) 695–720, <https://doi.org/10.1007/s44174-023-00142-4>.